

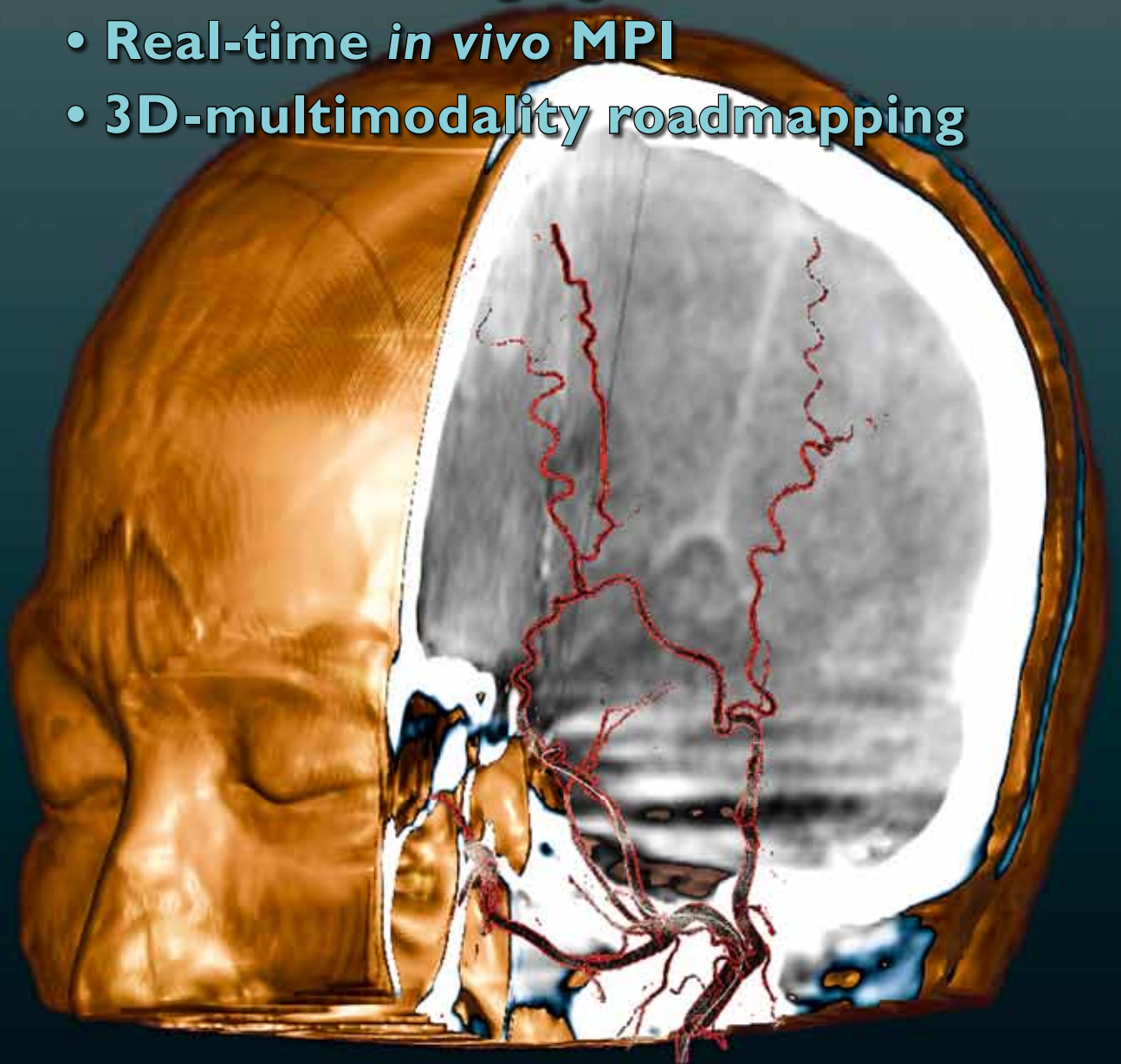
# MEDICAMUNDI

A review of modern healthcare solutions

Volume 53/2 2009

## Neurology:

- Quantitative CT imaging in stroke
- Advanced MRI applications
- Dynamic MRI of contortionists
- Molecular imaging in dementia
- Real-time *in vivo* MPI
- 3D-multimodality roadmapping



- ▶ **Editor-in-Chief:** E. O'Lionaird
- ▶ **Deputy Editor:** Dr J.A.J.M. Deckers
- ▶ **Editorial Board:**

Dr R. Aarnink  
 J. Beckett  
 Dr S.N. Boon  
 Drs H.J.B. Hadders  
 Dr S.A. Higgins  
 S.J.I. Lee  
 Dr P. Maniawski  
 Dr U. Neitzel  
 Dr D.J. Olego  
 R.B. Peterson  
 S.K. Pohlman  
 Dr M.B. Scheidegger  
 Dr E. Silfen  
 Dr P.H. Smit  
 Dr D.P. White  
 Dr G. Zeitler

- ▶ **Publisher:** Dr P.H. Smit
- ▶ **Project Manager:** Drs H.J.B. Hadders
- ▶ **Production Editors:** S.J.I. Lee and Consultek 2 B.V.
- ▶ **Digital Publishing Specialist:** W. Zimmermann
- ▶ **Correspondence (USA):**

**MEDICAMUNDI**  
 Philips Healthcare  
 Sales & Service Organization – North America  
 22100 Bothell Everett Highway  
 Bothell, Washington 98021-8431, USA

- ▶ **Correspondence (International):**

**MEDICAMUNDI**  
 Philips Healthcare Nederland B.V.  
 Building QX-2.135.1, P.O. Box 10 000,  
 5680 DA Best, the Netherlands

- ▶ **Internet address:**

[www.philips.com/medicamundi](http://www.philips.com/medicamundi)

- ▶ **Email address:** [healthcare@philips.com](mailto:healthcare@philips.com)

- ▶ **Print:** Daneels Graphic Group, Belgium

- ▶ **Published by:**

Philips Healthcare Nederland B.V.  
 All rights reserved. No part of this publication may be reproduced, stored in a retrieval system, or transmitted in any form or by any means, electronic, mechanical, photocopying, recording or otherwise, without the prior written permission of the Editor-in-Chief of **MEDICAMUNDI**.

- ▶ **Notice:**

Medicamundi is a professional journal for users of Philips medical equipment. It provides the healthcare community with results of scientific studies performed by colleagues. Some articles in this journal may describe research conducted outside the USA on equipment not yet available for commercial distribution in the USA.

- ▶ **ISSN:** 0025-7664

- ▶ **Code number:** 4522 962 55681 \* 2009

- ▶ © Koninklijke Philips Electronics N.V. 2009

- ▶ Printed in Belgium

For information on publishing articles in **MEDICAMUNDI**, please see the inside back cover.

**Next issue: Fall 2009**



## Dear Friends,

It gives me great pleasure to introduce this issue of Medicamundi, presenting the latest contributions of medical imaging to neurology.

Little more than thirty years ago, imaging of the living brain was virtually impossible, and tumors and other abnormalities could only be visualized by cumbersome and

often painful indirect procedures such as pneumoencephalography.

The advent of computed tomography and magnetic resonance imaging in the late 1970's provided new insights into the brain that would previously have been beyond the neurologist's wildest dreams.

Further developments of these modalities not only show the structure of the brain and its vessels, but also its function and development. In this issue we present some of the most recent advances in clinical applications and research.

Quantitative CT imaging of blood-brain barrier permeability offers new hope to stroke victims by enabling more widespread application of recombinant tissue plasminogen activator (rt-TPA), which has been shown to be effective in treating acute ischemic stroke.

Diffusion tensor imaging based MR tractography, presented as an experimental technique in Medicamundi some years ago, allows individual visualization of white matter tracts, including information on axonal integrity and myelination. It is now widely used in routine clinical practice, including preoperative planning for brain tumors and vascular malformations, and even more significantly, for monitoring the development of the brain in neonates and young children. This is of particular importance in monitoring infants at risk because of preterm birth.

A somewhat unusual article is a study of anterior limb fractures in contortionists, demonstrating the ability of the Panorama open MR system to examine the spine in extreme positions, unrestricted by the conventional cylinder.

We also pay attention to ongoing research projects, including the use of 7T MRI in the investigation of neurodegenerative diseases, and molecular imaging with FDG PET and target-specific ligands for *in vivo* assessment of the pathophysiological processes in dementia.

Magnetic particle imaging is a promising new technique providing very high spatial and temporal resolution. In this issue we present the first *in vivo* real-time scans of a beating heart in an animal model.

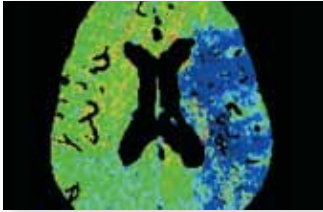
In addition to these various methods for image acquisition, we present some advanced techniques for processing and displaying the acquired image data.

I trust that you will enjoy reading this issue of Medicamundi, and hope that it will give you an interesting insight into the latest developments in neurological imaging.

Gene Saragnese  
 Executive Vice President and CEO Imaging Systems, Philips Healthcare

# Contents

## Computed tomography

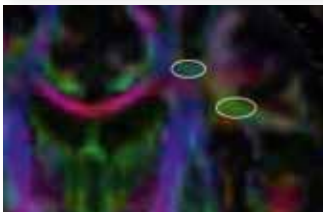


### 03 Blood-brain barrier permeability: quantification with computed tomography and application in acute ischemic stroke

*M. Wintermark, J. Hom, J. W. Dankbaar J. Bredno and M.E. Olszewski*

The costs associated with a stroke make improvements in treatment of paramount importance. Quantitative CT imaging may enable treatment based on physiology rather than time.

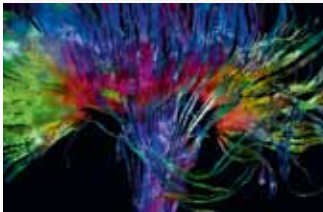
## Magnetic resonance imaging



### 09 Clinical MR tractography: past, present, and future

*K. Yamada, K. Akazawa, S. Yuen and T. Nishimura*

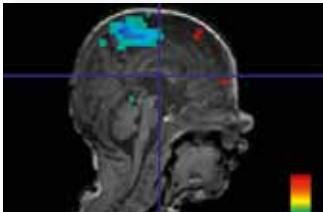
Diffusion tensor imaging (DTI)-based tractography was first introduced to the medical community a decade ago. Since then, the technique has been widely used in routine clinical practice in many different fields and its application is reviewed in this article.



### 16 Clinical applications of diffusion tensor imaging in children

*N.K. Rollins and J.M. Chia*

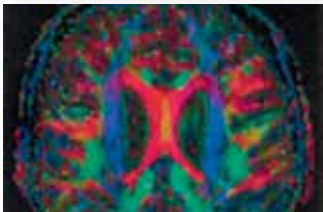
DTI, a relatively new addition to Magnetic Resonance (MR) imaging, exploits the preferential movement of water protons within the brain along the axis of the axons. DTI has numerous applications in the pediatric brain from birth onwards, in normal and disease states.



### 25 Functional MRI of the sensorimotor system in newborns

*H. Boecker, L. Scheef and A. Heep*

Neonatal functional MRI (fMRI) allows non-invasive *in vivo* mapping of dedicated brain circuits at the early stages of development. The article describes optimizing fMRI studies on infants at high risk of developing motor sequelae because of preterm birth.



### 29 7T MRI in neurology: initial results and future applications

*A.G. Webb, M.J. Versluis, M.A van Buchem, H.E. Kan, W.M. Teeuwisse and M.J.P. van Osch*

The C.J. Gorter Center for High Field MRI uses one of only two Philips Achieva 7T whole-body MRI research systems in the Netherlands to develop new methods and protocols.



### 37 Dynamic whole-spine MRI of contortionists

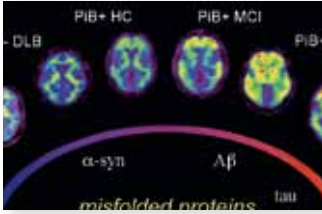
*W.W. Orrison Jr. and T.G. Perkins*

A study of anterior limbus fractures in a group of contortionists demonstrates the ability of the Panorama HFO 1T open MR system to examine the spine in extreme positions, without the restrictions imposed by the conventional cylinder.

Continued overleaf ►

# Contents

## Nuclear medicine

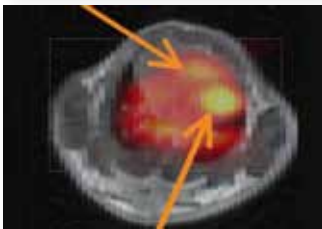


### 41 Molecular imaging in dementia: journey to the end of the night

*V.L. Villemagne and G.J. O'Keefe*

New therapeutic strategies for dementia increase interest in developing agents to allow assessment of the pathophysiological mechanisms. A review of recent developments in molecular imaging illustrates molecular imaging utility in clinical management of dementia.

## Magnetic particle imaging

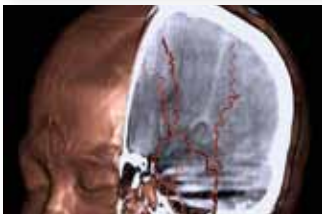


### 48 Three-dimensional real-time *in vivo* magnetic particle imaging

*J. Borgert, B. Gleich, J. Rahmer, H. Dahnke and J. Weizenecker*

Magnetic particle imaging (MPI) is a new imaging method capable of imaging the local concentration of commercially available contrast agent with high spatial and temporal resolution. This article presents the first *in vivo* 3D real-time MPI scans revealing details of a beating mouse heart using clinically approved concentrations of a commercially available MRI contrast agent.

## Image processing



### 58 3D-multimodality roadmapping in interventional neuroradiology

*T. Andersson, M. Söderman, D. Ruijters, D. Babic, R. Homan and P. Mielekamp*

This article describes a method of fusing, in real time, 2D fluoroscopic images with 3D MRI and CT images. The resulting combined image helps to reduce the overall workload and allows for a better anatomical understanding with more precise navigation.

## 63 Summaries

- 63 English
- 65 Français
- 67 Deutsch
- 69 Español

## 71 Technology News

- 71 Innovative neuroradiology interpretation made possible by Advanced Vessel Analysis on the Brilliance Workspace
- 71 The Wireless Portable Detector for DigitalDiagnost
- 72 FlexVision XL display helps clinicians to perform complex interventional procedures

# Blood-brain barrier permeability: quantification with computed tomography and application in acute ischemic stroke

- M. Wintermark** Department of Radiology and Biomedical Imaging, Neuroradiology Section, University of California, San Francisco, CA, USA.
- J. Hom**
- J. W. Dankbaar** Department of Radiology and Biomedical Imaging, Neuroradiology Section, University of California, San Francisco, CA, USA.  
Department of Radiology, University Medical Center, Utrecht, the Netherlands.
- J. Bredno** Department of Radiology and Biomedical Imaging, Neuroradiology Section, University of California, San Francisco, CA, USA.  
Philips Research North America, Briarcliff Manor, NY, USA.
- M. E. Olszewski** Computed Tomography Clinical Science, Philips Healthcare Cleveland, OH, USA.

Stroke is the third leading cause of death and the first leading cause of long-term disability in the United States, where annual direct and indirect costs of stroke care totaled US\$ 69 billion in 2006 [1]. Stroke may be ischemic or hemorrhagic in nature.

An ischemic stroke is defined as an infarction of central nervous system tissue [2] that may be either thrombotic or embolic in etiology, while a hemorrhagic stroke results from the rupture of a blood vessel in the brain. Ischemic stroke is the more common of the two subtypes, accounting for 87% of strokes in 2006 [1], and is most often caused by carotid atherosclerosis or cardioembolism.

Before the National Institute of Neurological Disorders and Stroke Recombinant Tissue Plasminogen Activator (NINDS rt-PA) stroke study, therapeutic options for stroke were nearly nonexistent; however, the NINDS study demonstrated the efficacy of treatment with intravenous rt-PA started within three hours of the onset of symptoms [3]. Meta-analysis of this and other major trials of IV rt-PA have confirmed the improved outcomes demonstrated by patients treated with rt-PA within the three-hour window. This also suggests that the treatment window may be widened to the potential benefit of patients [4].

The Safe Implementation of Treatments in Stroke (SITS) study, based on a prospective audit of the International Stroke Thrombolysis Registry (ISTR), concluded that rt-PA remains safe when given up to four and a half hours after the

onset of acute ischemic stroke [5]. Research on later treatment with rt-PA continues, with indications that thrombolysis may still be safe and effective up to six hours or more after symptoms begin. This includes the context of “wake up” strokes where the initial onset of focal neurological deficit may be unknown [6].

However, despite the promise shown by these studies, the number of stroke patients receiving therapy to date has been limited to between 1% and 18% of those eligible [3, 7-9]. While there are many reasons for exclusion [9, 10], medical and legal concerns regarding symptomatic hemorrhagic transformation (HT) are primary causes of this underutilization [10].

While it is well accepted that “time is brain” during a stroke [11], it is also known that cerebral tissue viability depends not only on time, but also cerebral hemodynamics, tissue status, and the applied intervention [12]. Given this intricate balance, it has been suggested that advanced imaging techniques should play a role in moving from this “time is brain” paradigm to a “physiology is brain” paradigm [13].

In particular, practical imaging techniques sensitive and specific enough to identify patients who could simultaneously benefit most from thrombolytic therapy and be at the lowest risk for HT, could increase the administration of rt-PA within the currently approved time window. This could also facilitate an increase in the number of patients considered for thrombolysis through an extension of that time window.

► **Stroke is the third leading cause of death and the first cause of disability in the USA.**

► **Advanced imaging supports the paradigm shift from “time is brain” to “physiology is brain”.**

This paper describes the risk of HT in acute ischemic stroke, the response of the blood-brain barrier to ischemic insult and its link to HT, and the role of computed tomography perfusion and permeability imaging in identifying patients who may benefit the most from thrombolytic therapy while being at the lowest risk for HT. A case study is also presented to demonstrate CT permeability imaging and its role in diagnosis and treatment planning for acute stroke.

### **Hemorrhagic transformation in acute ischemic stroke**

The most feared complication in acute ischemic stroke is HT. The most severe form of HT has devastating clinical consequences and is associated with an over ten-fold increase in mortality [14]. While HT may occur spontaneously in patients with no recanalization therapy [15-17], and less severe forms are seen in many stroke patients, thrombolysis significantly increases the risk of symptomatic HT. Symptomatic HT within 36 hours from the onset of stroke symptoms is seen up to ten times more often in treated (6.4% HT) versus untreated (0.6% HT) patients, and 61% of the patients with symptomatic HT die within three months [3, 4, 18, 19].

Any extension of the thrombolytic treatment window also implies an increased risk of HT. Data shows that the occurrence of HT in patients treated within three hours of symptom onset was 4.8%, while for those treated between three and six hours after onset the occurrence rose to 6.4% [3, 4, 18, 19]. This has motivated the search for predictors of HT [20-22].

Blood-brain barrier (BBB) breakdown resulting from ischemia before reperfusion therapy is hypothesized to contribute to HT in acute ischemic stroke patients [23]. This breakdown shows a prognostic relevance and may indicate the possibility of detecting and weighing risks of thrombolytic therapy before treatment [15-17, 24, 25].

### **The response of the blood-brain barrier to ischemic insult**

The blood-brain barrier (BBB) is a cellular structure in the central nervous system (CNS) that regulates the transfer of materials from the bloodstream to the neural tissue. In essence, the BBB restricts the passage of many chemicals and microscopic organisms that may be harmful to the CNS while maintaining passage of oxygen and other items necessary for metabolism.

This regulation is achieved through tight junctions among the cells of the CNS vascular endothelium. The resulting vascular lining has a low permeability for small polar molecules, ions, or even water, and few transcytotic vesicles exist [15] that enable paracellular routes for diffusion between the intravascular lumen and interstitial space. [26]. However, the BBB is permeable to many lipid-soluble substances [27].

Consequently, with an intact BBB, both the convection and diffusion of blood plasma and dissolved molecules are restricted [21], and permeability across the BBB for large hydrophilic molecules [23] is nearly nonexistent. Notably, permeability of contrast agents, such as the iodinated agents used in CT, is not commonly observed in the presence of an intact BBB. In most cases, contrast agent stays within the intravascular lumen during its passage through the CNS.

On the other hand, following an acute ischemic stroke the integrity of the BBB may be compromised by the ischemic insult to the vascular endothelium. While the exact mechanisms of this breakdown are not yet fully understood [21, 26, 27], multiple signaling molecules and mediators have been identified with respect to how rt-PA treatment may lead from BBB breakdown to HT [15].

Notably, the mechanisms of BBB breakdown lead to leakage of blood plasma across the now-open junctions between the endothelial cells of the BBB. Since cerebral endothelial cells are considered more resistant than neurons to ischemia, BBB breakdown is hypothesized to be an indicator for more significant ischemia and an increased likelihood of HT [17]. Of particular interest is that the resulting increase in BBB permeability may lead to observable contrast agent extravasation during CT imaging; hence, providing a quantitative imaging predictor of HT.

### **CT brain perfusion and blood-brain barrier permeability imaging**

Computed tomography (CT) is the gold standard for the diagnosis of hemorrhagic stroke and is a mandated imaging test to rule out alternate etiologies for patients with stroke symptoms [28]. In addition, the rapid evolution of multidetector CT in the past decade has enabled perfusion CT imaging to quickly and quantitatively evaluate dynamic brain perfusion – including cerebral blood flow, cerebral blood volume, and mean transit time (Figure 1) [29, 30].

► **Hemorrhagic transformation (HT) is the most feared complication in acute ischemic stroke.**

► **CT is the gold standard for the diagnosis of hemorrhagic stroke.**

This functional information has the potential to identify infarcted tissue, while also identifying the ischemic penumbra that may be saved, and the technique has been shown to be accurate in comparison with acute and delayed diffusion-weighted and perfusion-weighted magnetic resonance imaging [31-33]. CT is particularly attractive since it is readily available in most emergency departments, thus enabling rapid diagnosis and treatment [11].

As noted earlier, BBB breakdown is not an “all or nothing” phenomenon [34, 35], but is a gradual process that needs quantification to assess its severity. The goal of such quantification is to predict HT that may cause clinical deterioration in patients with reperfusion injury and to use this quantitative information to weigh the risks and benefits of potential treatment options. Perfusion CT imaging allows quantification of the rate of BBB permeability.

The Patlak model can be used to quantify BBB permeability from perfusion CT data [36, 37]. As applied to perfusion CT, the Patlak model assumes unidirectional flow of contrast from the vascular lumen to the cerebral parenchyma during a steady-state phase, and allows the calculation of BBB permeability by graphical analysis of the Patlak plot.

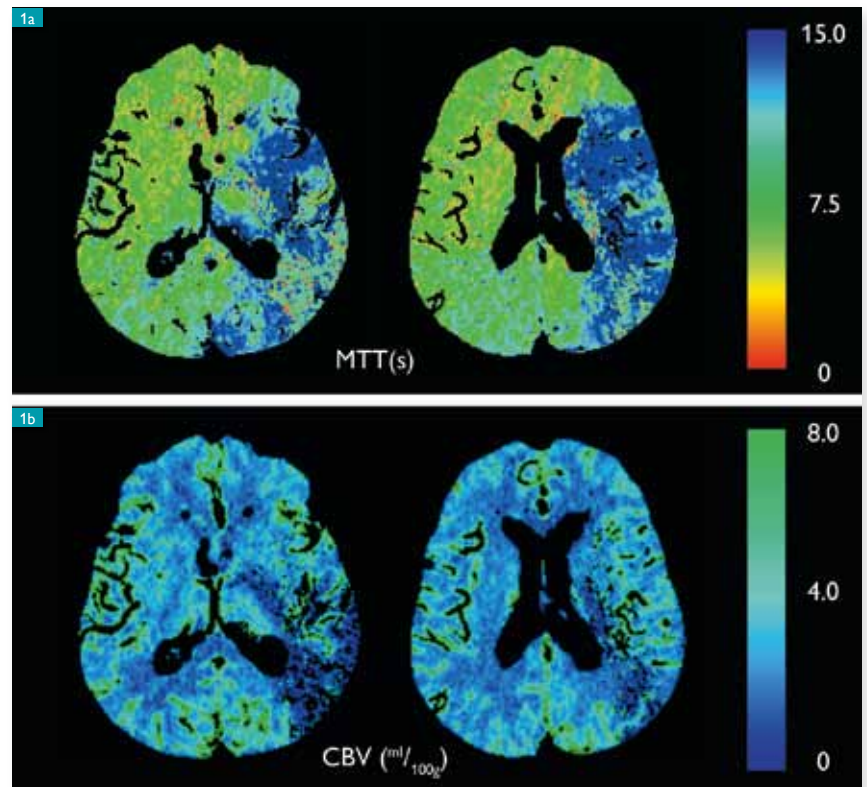
This analysis follows image acquisition using a slightly modified perfusion CT protocol that includes a delayed phase of four minutes [38], since previous studies have shown that analysis of first-pass data leads to significant overestimations of BBB permeability [39]. In addition, it has been shown that a two-bolus technique can be used to extend the anatomical coverage of BBB permeability assessment without loss of accuracy [40].

Despite this acquisition extension, radiation exposure to the patient is minimized by using a lowered cycle time during the delayed phase, leading to an increase in effective dose of only ten percent beyond that of a standard perfusion CT acquisition.

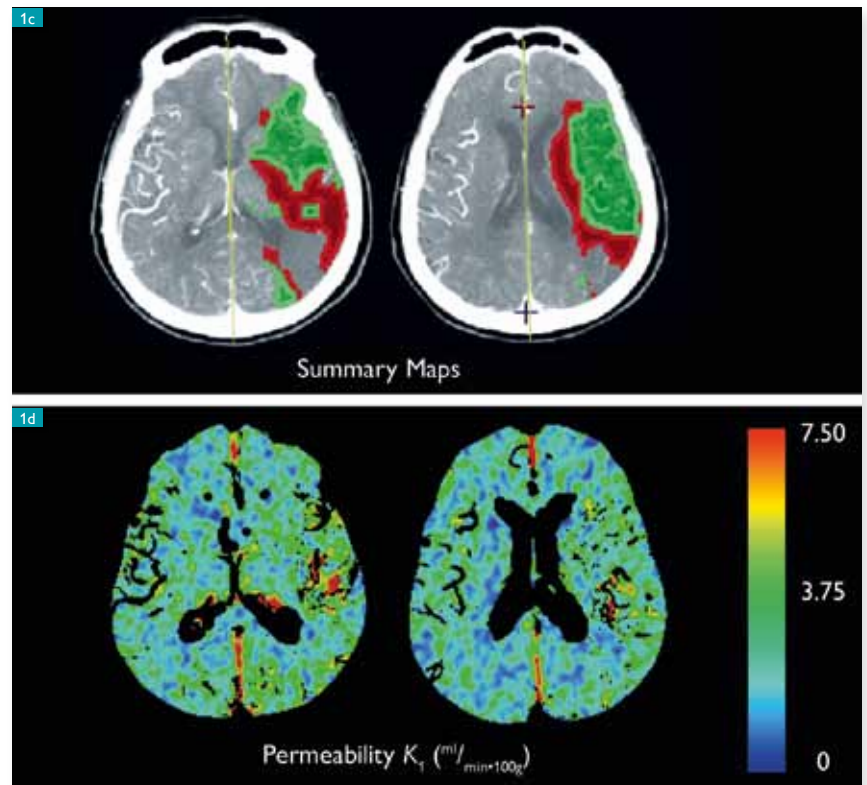
### Clinical decision support in acute stroke

Dynamic brain perfusion CT with maps of the infarct core and penumbra (Summary Maps, Brain Perfusion, Philips Healthcare, Cleveland, OH) provides a potential tool to move beyond the existing treatment time criteria to provide individualized imaging assessments of acute stroke patients [33]. As an automated procedure, this assessment will not only decrease the time

Figure 1. CT perfusion imaging.



▲ Figure 1a. Ischemic tissue is identified by an increased mean transit time.  
▲ Figure 1b. Infarcted tissue is identified by reduced cerebral blood volume.

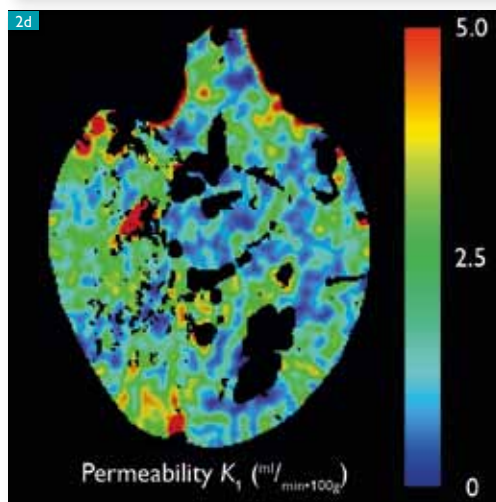
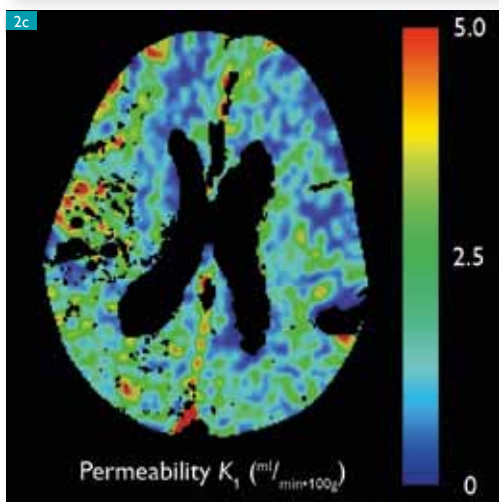


▲ Figure 1c. Summary maps indicate areas of increased mean transit time (MTT)/preserved cerebral blood volume (CBV), and of increased MTT/decreased CBV, that correspond to infarct core (red) and ischemic penumbra (green), respectively.  
▲ Figure 1d. In addition to these state-of-the-art parameter maps, the measurement of BBB permeability may identify areas at risk of hemorrhagic transformation.

Figure 2. 85-year-old female presenting with left hemiparesis. Admission imaging revealed no evidence of intracranial hemorrhage and IV rt-PA was administered.



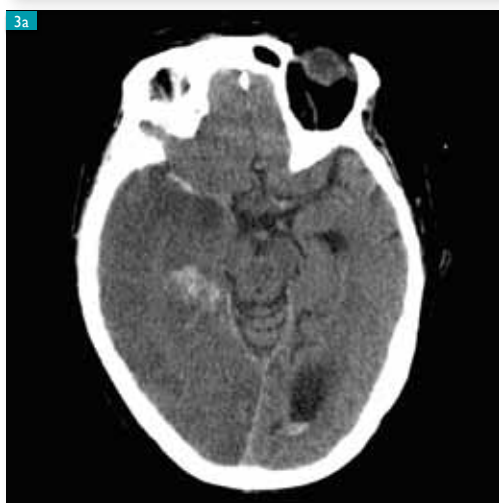
▶  
Figure 2a, b. Non-contrast CT.



▶  
Figure 2c, d. Perfusion CT.

Figure 3. Same patient as Figure 2.

▶  
Figure 3a, b. 26 hours after admission the patient developed multiple intraparenchymal hematomas. Retrospective analysis with prototype permeability software demonstrated that the patient presented with increased BBB permeability (Figure 2b,d) at the same locations as the eventual hematoma.



to treatment, but also enables a reduction in the potential variability among measured parameters [41].

Building upon this paradigm, quantitative BBB permeability imaging may be used as a surrogate biomarker to identify patients that may benefit from therapy and those for whom therapy may only increase the risk of HT. The developed tools have already enabled a first study of age- and anatomy-related BBB permeability

values that may permit detection of abnormal BBBP values when assessing acute ischemic stroke patients for the risk of HT [42].

### Case study

An 85-year-old female presented with left hemiparesis. She underwent stroke CT imaging work-up (noncontrast CT, perfusion CT, CT angiography) within three hours after symptom onset. Noncontrast CT (Figure 2a, b) revealed

no evidence of intracranial hemorrhage, and perfusion imaging indicated an acute M1 occlusion. The patient was treated with IV rt-PA at that time; however, 26 hours later she presented with symptoms suggesting HT. Follow-up noncontrast CT at that time demonstrated multiple new regions of intraparenchymal hemorrhage (Figure 3a, b).

Retrospective analysis with the prototype permeability analysis software indicates that the patient presented with elevated permeability (Figure 2c, d) on the baseline perfusion CT study in areas near the foci of significant hemorrhage in the patient's eventual parenchymal hematoma. Of note, the areas of increased permeability occur in both the infarct and penumbra – not just in the infarct, where the vasculature has presumably undergone the most severe ischemia-induced damage. This highlights that permeability imaging provides information beyond what is provided by the standard perfusion CT parameters that can be used to define infarct and penumbra.

## Discussion

Quantitative BBB permeability imaging in the acute stroke setting may provide individualized clinical decision support that can predict complications of thrombolytic therapy. This decision support may allow the extension of the rt-PA time window and may increase rt-PA administration rates by reducing the risk associated with treatment. Through these simultaneous actions, the population of stroke patients eligible for thrombolysis may increase substantially.

## Informed consent

Imaging data referred to in this article were obtained as part of standard clinical stroke care at the University of California, San Francisco (UCSF), and were retrospectively reviewed with the approval of the UCSF institutional review board ■

► **Quantitative BBB permeability imaging may help predict complications of thrombolytic therapy.**

## References

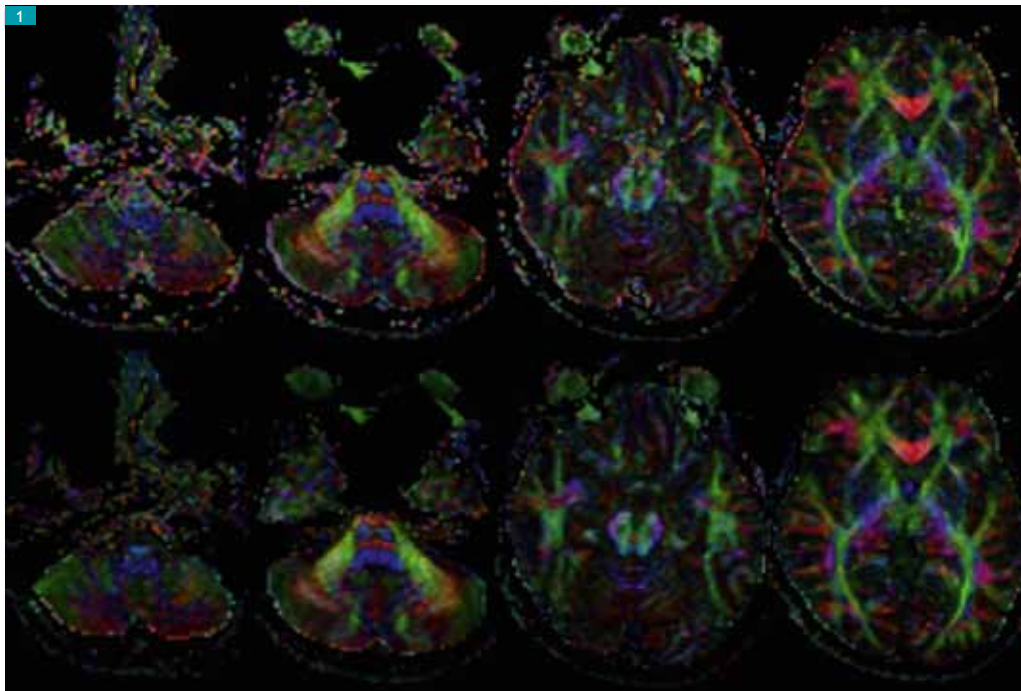
- [1] Lloyd-Jones D, Adams R, Carnethon M, De Simone G, Bruce Ferguson T, Flegal K, et al. *Heart Disease and Stroke Statistics – 2009 Update: A Report from the American Heart Association Statistics Committee and Stroke Statistics Subcommittee*. Circulation. 2009; 119: 480–486.
- [2] Easton JD, Saver JL, Albers GW, Alberts MJ, Chaturvedi S, Feldman E, et al. *Definition and Evaluation of Transient Ischemic Attack: A Scientific Statement for Healthcare Professionals from the American Heart Association/American Stroke Association Stroke Council; Council on Cardiovascular Surgery and Anesthesia; Council on Cardiovascular Radiology and Intervention; Council on Cardiovascular Nursing; and the Interdisciplinary Council on Peripheral Vascular Disease*. Stroke. 2009; 40: 2276–2293.
- [3] The National Institute of Neurological Disorders and Stroke rt-PA Stroke Study Group. *Tissue Plasminogen Activator for Acute Ischemic Stroke*. N Engl J Med. 1995; 333: 1581–1587.
- [4] Hacke W, Donnan G, Fieschi C, Kaste M, von Kummer R, Broderick JP, et al. *Association of Outcome with Early Stroke Treatment: Pooled Analysis of ATLANTIS, ECASS, and NINDS rt-PA Stroke Trials*. Lancet. 2004; 363: 768–774.
- [5] Wahlgren N, Ahmed N, Dávalos A, Hacke W, Millán M, Muir K, et al. *Thrombolysis with Alteplase 3–4.5 h after Acute Ischaemic Stroke (SITS-ISTR): An Observational Study*. Lancet. 2008; 372: 1303–1309.
- [6] Barreto AD, Martin-Schild S, Halleivi H, Morales MM, Abraham AT, Gonzales NR, et al. *Thrombolytic Therapy for Patients who Wake-up with Stroke*. Stroke. 2009; 40: 827–832.
- [7] Koennecke HC, Nohr R, Leistner S, Marx P. *Intravenous tPA for Ischemic Stroke Team Performance over Time, Safety, and Efficacy in a Single-Center, 2-year Experience*. Stroke. 2001; 32: 1074–1078.
- [8] Katzan IL, Hammer MD, Furlan AJ, Hixson ED, Nadzam DM. *Quality Improvement and Tissue-Type Plasminogen Activator for Acute Ischemic Stroke: a Cleveland Update*. Stroke. 2003; 34: 799–800.
- [9] Cocho D, Belvís R, Martí-Fàbregas J, Molina-Porcel L, Diaz-Manero J, Aleu A, et al. *Reasons for Exclusion from Thrombolytic Therapy following Acute Ischemic Stroke*. Neurology. 2005; 64: 719–720.
- [10] Bambauer KZ, Johnston SC, Bambauer DE, Zivin JA. *Reasons Why Few Patients with Acute Stroke Receive Tissue Plasminogen Activator*. Arch Neurol. 2006; 63: 661–664.
- [11] Saver JL. *Time is Brain—Quantified*. Stroke. 2006; 37: 263–266.
- [12] Warach S. *Tissue Viability Thresholds in Acute Stroke: the 4-factor Model*. Stroke. 2001; 32: 2460–2461.
- [13] González RG. *Imaging-Guided Acute Ischemic Stroke Therapy: From “Time is Brain” to “Physiology is Brain”*. AJNR Am J Neuroradiol. 2006; 27: 728–735.
- [14] Berger C, Fiorelli M, Steiner T, Schäbitz W-R, Bozzao L, Bluhmki E, et al. *Hemorrhagic Transformation of Ischemic Brain Tissue: Asymptomatic or Symptomatic?* Stroke. 2001; 32: 1330–1335.
- [15] Wang X, Lo EH. *Triggers and Mediators of Hemorrhagic Transformation in Cerebral Ischemia*. Mol Neurobiol. 2003; 28: 229–244.
- [16] Bisdas S, Hartel M, Cheong LH, Koht S. *Detection of Early Vessel Leakiness in Acute Ischemic Stroke using Computed Tomography Perfusion may indicate Hemorrhagic Transformation*. Acta radiologica. 2007; 48: 341–344.

- [17] Bang OY, Buck BH, Saver JL, Alger JR, Yoon SR, Starkman S, et al. *Prediction of Hemorrhagic Transformation after Recanalization Therapy using T2\*-Permeability Magnetic Resonance Imaging*. Ann Neurol. 2007; 62: 170–176.
- [18] Hacke W, Kaste M, Bluhmki E, Brozman M, Dávalos A, Guidetti D, et al. *Thrombolysis with Alteplase 3 to 4.5 hours after Acute Ischemic Stroke*. N Engl J Med. 2008; 359: 1317–1329.
- [19] The NINDS t-PA Stroke Study Group. *Intracerebral Hemorrhage after Intravenous t-PA Therapy for Ischemic Stroke*. Stroke. 1997; 28: 2109–2118.
- [20] Selim M, Fink JN, Kumar S, Caplan LR, Horkan C, Chen Y, et al. *Predictors of Hemorrhagic Transformation after Intravenous Recombinant Tissue Plasminogen Activator: Prognostic Value of the Initial Apparent Diffusion Coefficient and Diffusion-Weighted Lesion Volume*. Stroke. 2002; 33: 2047–2052.
- [21] Ding B, Ling HW, Chen KM, Jiang H, Zhu YB. *Comparison of Cerebral Blood Volume and Permeability in Preoperative Grading of Intracranial Glioma using CT Perfusion Imaging*. Neuroradiology. 2006; 48: 773–781.
- [22] Jiang Q, Ewing JR, Ding GL, Zhang L, Zhang ZG, Li L, et al. *Quantitative Evaluation of BBB Permeability after Embolic Stroke in Rat using MRI*. Journal of Cerebral Blood Flow and Metabolism. 2005; 25: 583–592.
- [23] Lin K, Kazmi KS, Law M, Babb J, Peccerelli N, Pramanik. *Measuring Elevated Microvascular Permeability and Predicting Hemorrhagic Transformation in Acute Ischemic Stroke using First-pass Dynamic Perfusion CT imaging*. Am J Neuroradiology. 2007; 28: 1292–1298.
- [24] Lampl Y, Shmuilovich O, Lockman J, Sadeh M, Lorberboym M. *Prognostic Significance of Blood Brain Barrier Permeability in Acute Hemorrhagic Stroke*. Cerebrovascular Diseases. 2005; 20: 433–437.
- [25] Neumann-Haefelin C, Brinker G, Uhlenkücken U, Pillekamp F, Hossman K-A, Hoehn M. *Prediction of Hemorrhagic Transformation after Thrombolytic Therapy of Clot Embolism: an MRI investigation in Rat Brain*. Stroke. 2002; 33: 1392–1398.
- [26] Fraser PA, Dallas AD. *Permeability of Disrupted Cerebral Microvessels in the Frog*. J Physiol. 1993; 461: 619–632.
- [27] Ewing JR, Knight RA, Nagaraja TN, Yee J, Nagesh V, Whitton P, et al. *Patlak Plots of Gd-DTPA MRI Data yield Blood-Brain Transfer Constants Concordant with those of <sup>14</sup>C-Sucrose in Areas of Blood-Brain Opening*. Magnetic resonance in medicine 2003; 50:283–292
- [28] Adams HP, del Zoppo G, Alberts MJ, Bhatt DL, Brass, Furlan A, et al. *Guidelines for the Early Management of Adults with Ischemic Stroke: a Guideline from the American Heart Association/American Stroke Association Stroke Council, Clinical Cardiology Council, Cardiovascular Radiology and Intervention Council, and the Atherosclerotic Peripheral Vascular Disease and Quality of Care Outcomes in Research Interdisciplinary Working Groups*. Circulation. 2007; 115: e478–e534.
- [29] Wintermark M, Thiran JP, Maeder P, Schnyder P, Meuli R. *Simultaneous Measurement of Regional Cerebral Blood Flow by Perfusion CT and Stable Xenon CT: A Validation Study*. AJNR Am J Neuroradiol. 2001; 22: 905–914.
- [30] Wintermark M, Bogousslavsky J. *Imaging of Acute Ischemic Brain Injury: The Return of Computed Tomography*. Curr Opin Neurol. 2003; 16: 59–63.
- [31] Wintermark M, Reichhart M, Cuisenaire O, Maeder P, Thiran J-P, Schnyder P, et al. *Comparison of Admission Perfusion Computed Tomography and Qualitative Diffusion- and Perfusion-Weighted Magnetic Resonance Imaging in Acute Stroke Patients*. Stroke. 2002; 33: 2025–2031.
- [32] Wintermark M, Reichhart M, Thiran JP, Maeder P, Chalaron M, Schnyder P, et al. *Prognostic Accuracy of Cerebral Blood Flow Measurement by Perfusion Computed Tomography, at the time of Emergency Room Admission, in Acute Stroke Patients*. Ann Neurol. 2002; 51: 417–432.
- [33] Wintermark M, Flanders AE, Velthuis B, Meuli R, van Leeuwen M, Goldsher D, et al. *Perfusion-CT Assessment of Infarct Core and Penumbra: Receiver Operating Characteristic Curve Analysis in 130 Patients Suspected of Acute Hemispheric Stroke*. Stroke. 2006; 37: 979–985.
- [34] Tofts PS, Kermode AG. *Measurement of the Blood-Brain Barrier Permeability and Leakage Space using Dynamic MR Imaging. 1. Fundamental Concepts*. Magnetic Resonance in Medicine. 1991; 17: 357–367.
- [35] Nagaraja TN, Karki K, Ewing JR, Croxen RL, Knight RA. *Identification of Variations in Blood-Brain Barrier Opening after Cerebral Ischemia by Dual Contrast-Enhanced Magnetic Resonance Imaging and T<sub>1st</sub> Measurements*. Stroke 2008; 39: 427–432.
- [36] Patlak CS, Blasberg RG. *Graphical Evaluation of Blood-to-Brain Transfer Constants from Multiple-time Uptake Data. Generalizations*. Journal of Cerebral Blood Flow and Metabolism. 1985; 5: 584–590.
- [37] Patlak CS, Blasberg RG, Fenstermacher JD. *Graphical Evaluation of Blood-to-Brain Transfer Constants from Multiple-Time Uptake Data*. Journal of Cerebral Blood Flow and Metabolism. 1983; 3: 1–7.
- [38] Hom J, Dankbaar JW, Schneider T, Cheng SC, Bredno J, Wintermark M. *Optimal Duration of Acquisition for Dynamic Perfusion CT Assessment of Blood-Brain Barrier Permeability using the Patlak Model*. AJNR Am J Neuroradiol. 2009; Epub ahead of print.
- [39] Dankbaar JW, Hom J, Schneider T, Cheng SC, Lau BC, van der Schaaf I, et al. *Dynamic Perfusion CT Assessment of the Blood-Brain Barrier Permeability: First Pass versus Delayed Acquisition*. AJNR Am J Neuroradiol. 2008; 29: 1671–1676.
- [40] Dankbaar JW, Hom J, Schneider T, Cheng SC, Lau BC, van der Schaaf I, et al. *Dynamic Accuracy and Anatomical Coverage of Perfusion CT Assessment of the Blood-Brain Barrier Permeability: One Bolus versus Two Boluses*. Cerebrovasc Dis. 2008; 26: 600–605.
- [41] Soares BP, Dankbaar JW, Bredno J, Cheng SC, Bhogal S, Dillon WP, et al. *Automated versus Manual Post-Processing of Perfusion-CT Data in Patients with Acute Cerebral Ischemia: Influence on Interobserver Variability*. Neuroradiology 2009; 51: 445–451.
- [42] Dankbaar JW, Hom J, Schneider T, Cheng SC, Lau BC, van der Schaaf I, et al. *Age- and Anatomy-related Values of Blood-Brain Barrier Permeability Measured by Perfusion-CT in Non-stroke Patients*. J Neuroradiol. 2009; Epub ahead of print.

# Clinical MR tractography: past, present, and future

**K. Yamada** Department of Radiology, Graduate School of Medical Science,  
**K. Akazawa** Kyoto Prefectural University of Medicine, Kajii-cyo, Kawaramachi  
**S. Yuen** Hirokoji Sagaru, Kamigyo-ku, Kyoto, Japan  
**T. Nishimura**

Without registration



With registration

Figure 1. Effect of image registration. Color-coded vector maps of a DTI data set of a normal volunteer are shown ( $b = 1000$ , averaging = 1, and 32 motion probing gradient directions). The images of the upper row represent the calculated vector maps without image registration. The images of the lower row represent those with registration. Note that one can achieve higher image quality using this technique, especially at the boundaries between the CSF and the brain surface. The vector elements of the color maps are assigned to red (x element, left to right), green (y element, anteroposterior), and blue (z element, superoinferior). The intensities of the color map are scaled in proportion to the FA.

Diffusion-tensor tractography is one of the most remarkable advances in the field of neuroimaging in the past decade. This method offers *in vivo* visualization of water diffusion along neuronal fiber tracts, which previously was not possible. As a clinical tool, this technique primarily targets intracranial space-occupying lesions, that is, brain tumors and vascular malformations [1-6]. Surgical resection of brain masses involving the so-called eloquent areas remains a huge challenge.

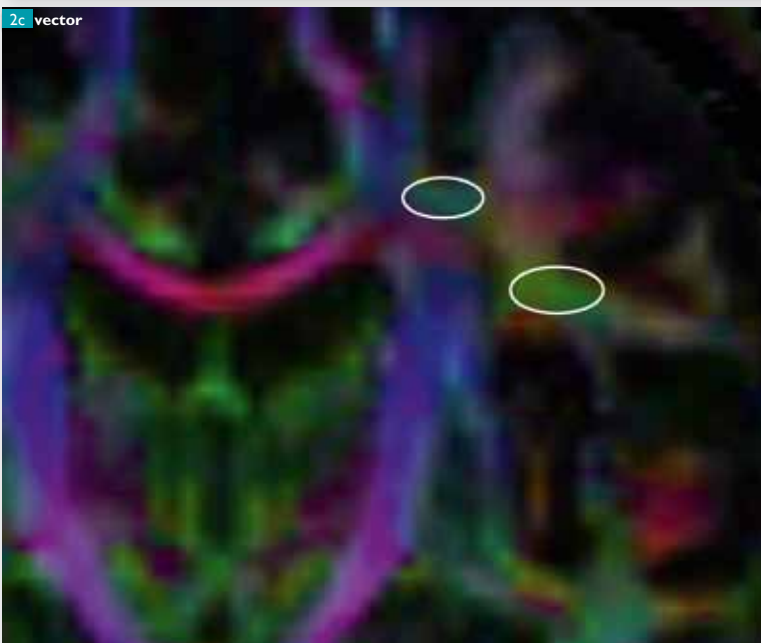
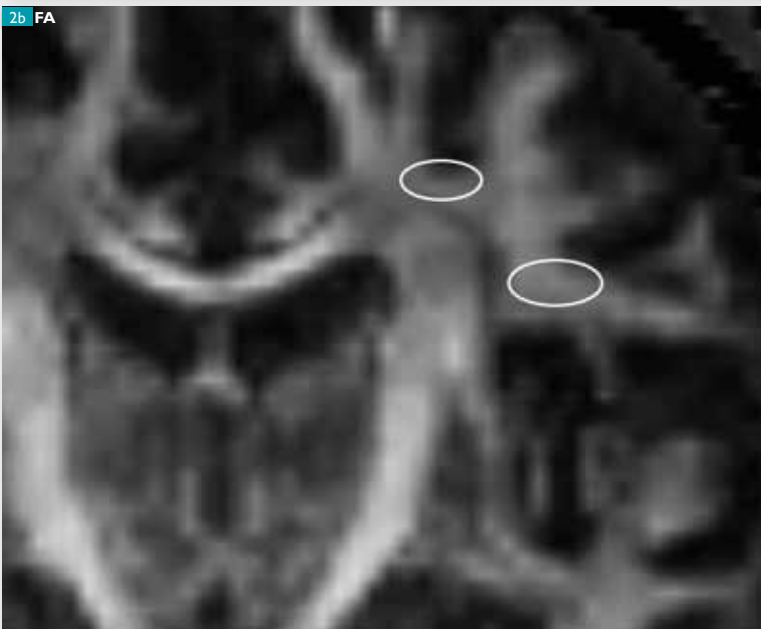
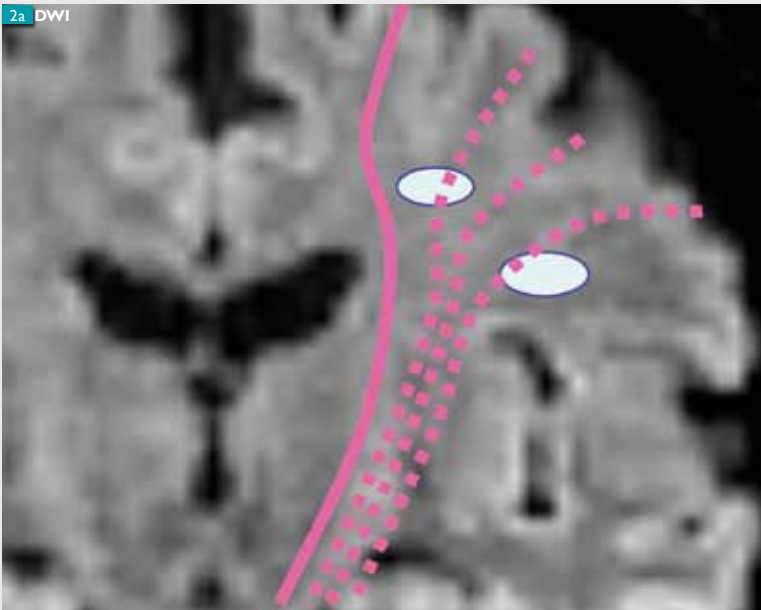
Various adjunct strategies have been employed to improve patient outcomes. These include awake surgery, intraoperative navigation systems, and intraoperative electrical stimulation. It has also been suggested that preservation of cortical, as well as subcortical, function is critical for improving outcomes; thus, the visualization of eloquent white matter tracts is an important issue. However, when using diffusion-tensor tractography clinically, some limitations need to be addressed. These will be discussed later in this article.

## The basics of tractography

Water-diffusion anisotropy (directionality) in the white matter of the brain is defined on the basis of axonal alignment [3]. Water diffusion preferentially diffuses along the axon's longitudinal axis but is relatively restricted in the perpendicular axis. This phenomenon can be represented mathematically by the so-called diffusion ellipsoid, or tensor. These tensors can be reconstructed to track three-dimensional macroscopic fiber orientation in the brain.

The translation of the longest axis of the tensor ( $v_1$ ) into neural trajectories can be achieved by various algorithms. These algorithms can be broadly classified into two types; that is, deterministic and probabilistic. Deterministic algorithms were the first ones invented and remain the most commonly used clinically. One of the first deterministic methods invented was the Fiber Assignment by Continuous Tracking (FACT) algorithm [1, 7].

► **Diffusion-tensor tractography offers *in-vivo* visualization of the neuronal fiber tracts.**



Trajectories are mapped by designating two arbitrary regions of interest (ROI) in three-dimensional space. Tracking is terminated when a pixel with low fractional anisotropy (FA) or a predetermined trajectory curvature between two contiguous vectors is reached.

### Evolution in imaging techniques

When the diffusion-tensor imaging (DTI)-based tractography technique was first introduced, its major drawback was the duration of the examination (typically more than 30 minutes) [8]. Multi-shot (segmented) echo planar imaging (EPI) was one of the imaging methods of choice in the early days. As it requires cardiac gating, this limits the number of echoes acquired and thus leads on to an extended imaging time.

The multi-shot technique was used primarily to reduce image distortion, but later studies demonstrated that single-shot EPI (ssEPI) with parallel imaging technique is an alternative to the multi-shot EPI. Using ssEPI, image acquisition can be shortened to less than five minutes while obtaining fair tractographic results [5]. Thus, the ssEPI technique is now considered the standard imaging method of choice for brain DTI.

For clinical scans, the signal to noise ratio (SNR) of the images must be balanced against scan time, since motion artifact becomes overt when the scan time is too long. Thus, it seems reasonable to combine data from several separate DTI examinations, each approximately five to ten minutes in length, to effectively increase the SNR [9]. Motion correction and image registration between these data sets would result in higher image quality (Figure 1).

Imaging resolution is another important factor that could affect the results of tractography. Especially important is the resolution in the z-axis (that is, slice thickness) to obtain voxels that are close to isotropic shape. When a regular slice thickness of 5 mm to 8 mm is used, the effect of partial volume averaging degrades the data set and leads to apparently inferior tracking results [10]. It has also been shown that this adverse effect is most pronounced at the areas with crossing fibers [10].

◀ Figure 2. Illustration of the pyramidal tract fibers descending from the primary motor cortex. The trunk and lower extremity fibers are drawn with purple lines. The fibers from the hand/face/tongue regions (dashed lines) are much more difficult to depict owing to the presence of crossing fibers, such as the superior longitudinal fasciculus and the arcuate fasciculus (circles).

## More advanced imaging techniques

Depiction of crossing fibers has always been the central problem for tractography. For instance, the motor tracts of the brain should have a fan-shaped configuration at the level of the centrum semiovale. However, the fiber-tracking technique can only depict the fibers traveling from the vertex of the brain. This is attributable to the existence of multiple crossing fibers at the level of the centrum semiovale, which leads to inaccuracy in the estimation of the direction of anisotropy in these areas (Figure 2).

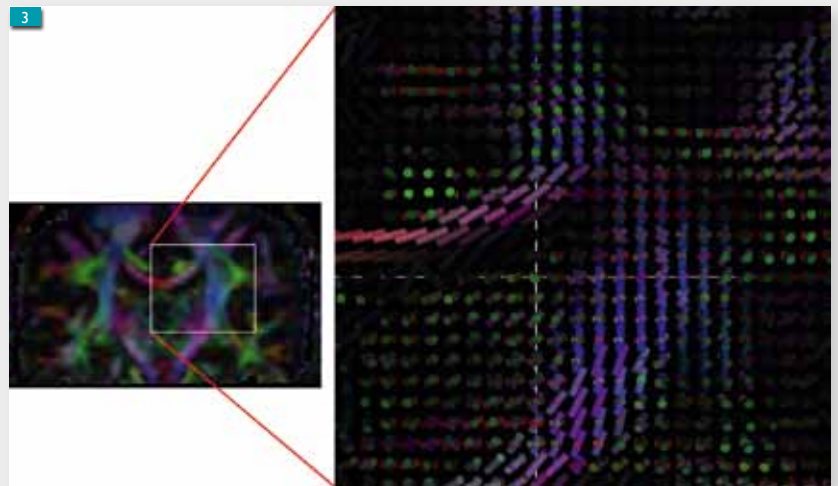
The development of new models and methods seeks to provide solutions for these problems. Recent studies have shown successful reconstruction of multiple intravoxel fibers [9, 11, 12]. These new techniques would improve the reproducibility and reliability of tractography (Figure 3, 4).

In order to carry out these more advanced techniques, one has to use higher angular resolution of the diffusion-sensitizing gradients, as well as higher b-values, which would prolong imaging time. The highest b-values that one can use on a regular clinical scanner are usually limited to approximately  $3000 \text{ s/mm}^2$ . However, a simulation study has shown that the benefit of increasing the b-value in this range would not enable robust depiction of the crossing fibers [13].

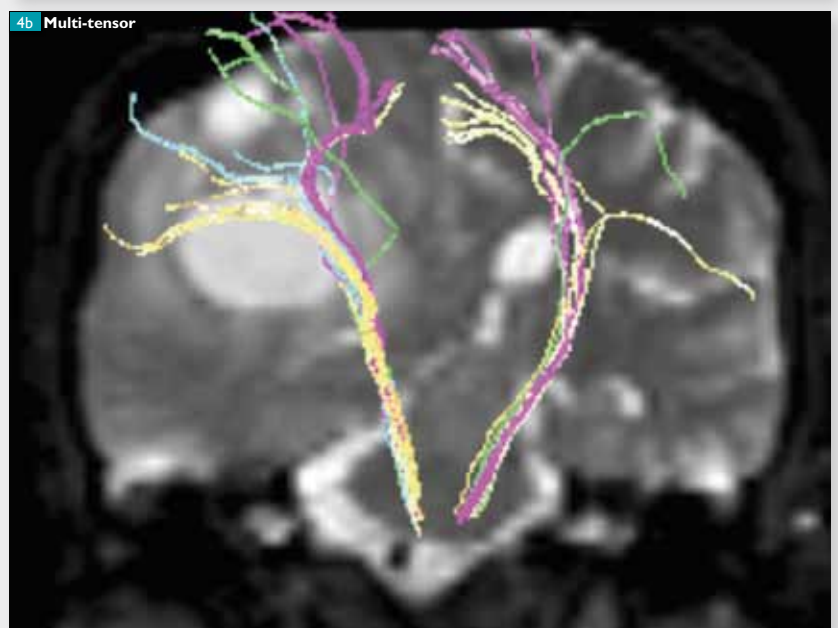
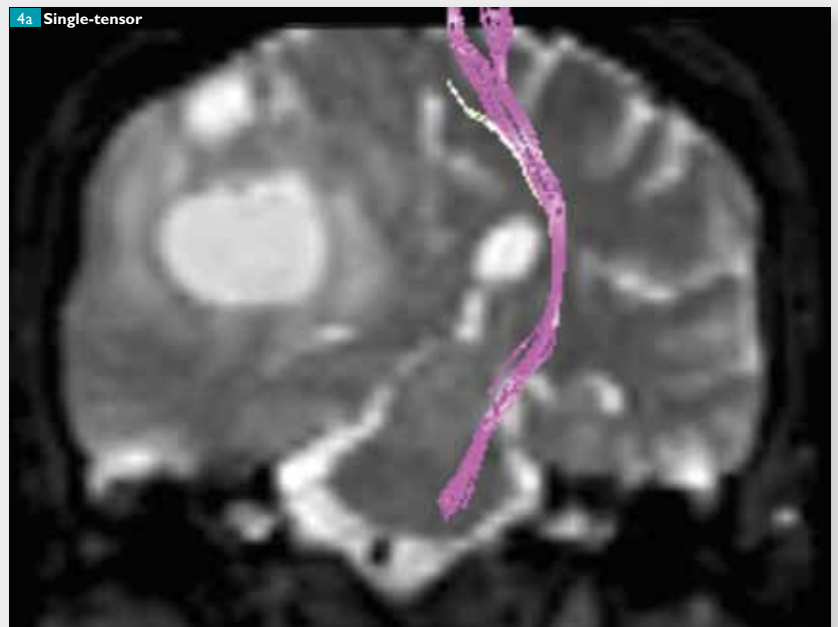
## Probabilistic approach

The probabilistic approach is the alternative to the deterministic approach, (for example, FACT). By its nature, the deterministic approach is only able to produce one reconstructed trajectory per seed point and is therefore, not able to depict branching fibers. The applied arbitrary anisotropy threshold will force the early termination of the reconstructed pathway. These issues have limited the usefulness of deterministic approaches in defining certain fiber tracts.

Probabilistic tractography algorithms aim to address these criticisms by considering multiple pathways emanating from the seed point and from each point along the reconstructed trajectories. Thus, the probabilistic method accounts for the uncertainty in the estimation of



▲ Figure 3. Areas with crossing fibers at the centrum semiovale. With multi-tensor analysis, one can now resolve the crossing fibers. A model-dependent approach (two tensor model) was used for this analysis.



► Figure 4. A 58-year-old woman with glioblastoma is shown. A large right parietal lobe tumor is noted with surrounding vasogenic edema. Note that the pyramidal fibers of the lesional side (right hemisphere) are not depicted using single-tensor tractography, whereas they are well shown using multitensor tractography.

fiber direction. It also attempts to provide some estimate of confidence in the projected neural pathway. This method is also known to be resistant to noise, which would be a clear benefit for clinical scans that have limited SNRs.

For neurosurgical planning, however, the probabilistic approach has some weaknesses [15]. First, the probabilistic approach is slower and, therefore, cannot be used interactively. Second, probabilistic methods may be harder to interpret visually. Instead of discrete geometric pathways, probabilistic methods generate a 3D volume of potential connectivities. The depicted connectivity maps tend to leak into unexpected regions of the brain. Thus, one has to use anatomical knowledge to judge which parts of the depicted fibers are relevant.

### Limitations of tractography

Perhaps the most important limitation of tractography is that it has not yet been fully validated. Attempts to validate this technique have been made in the past [16-18]. Most of these efforts are based on comparisons of the tractographic images and known neuroanatomy. A study that evaluated deterministic tractography in patients who underwent intraoperative electrophysiological tests indicated that tractography appears to underestimate fiber tracts [19].

Thus, the tool has to be used with caution, knowing that observations are on only a fraction of the reality. The probabilistic approach mentioned above would depict more fibers, thus leading to less serious underestimation. The relevant fibers, however, have to be judged in each case based on anatomical knowledge, and thus it remains to be proven whether the probabilistic approach is a better tool.

### Clinical application: brain tumors

Tractography has been used for preoperative assessment of eloquent white matter tracts. The most common target thus far has been the pyramidal tract [20-22], because of the relative importance of this fiber bundle for activity in daily life. The centrum semiovale is one of the most difficult areas from which to obtain a reliable landmark to locate the pyramidal tract during surgery, therefore, this technique would be particularly helpful.

Another important fiber pathway is the optic radiation. Damage to the optic radiation results in a visual field defect. Therefore, preoperative knowledge about the location of the optic

radiation is important. There are areas that are difficult to depict with this technique, which is the anterior part of Myer's loop [23].

Underestimation probably occurs due to the presence of a crossing fiber from the medial geniculate body to the superior temporal gyrus (that is, the primary auditory cortex) [24]. A recent study has shown that this problem can be overcome by depicting the uncinate fasciculus, which represents the anterior limits of the optic radiation [25].

### Clinical application: stroke and beyond

DTI has also been used in the field of stroke imaging. The technique has been used to assess the relationship between the eloquent fiber tracts and small brain infarcts [26, 27]. These clinicoradiological correlation studies have indicated that tractographic results have a fair correlation with clinical symptoms. Later studies have shown that it may also be used to measure a patient's outcome after stroke [28-30].

Assessment of the language circuits, one of which is known as the arcuate fasciculus, has also been attempted [31-33]. This fiber tract connects the temporal lobe (primary auditory cortex), Wernicke's area, and Broca's area (frontal lobe). This fiber bundle is considered an eloquent one when the left hemisphere is considered. Vascular insult to this circuit can result in conduction aphasia [32]. Studies have shown that the degree of damage to this circuit can predict the patient's language function in the chronic stage following the vascular event [33].

DTI can be applied to fields other than neuro-oncology and stroke. In fact, DTI has been used to characterize amyotrophic lateral sclerosis (ALS) [34, 35], pediatric ischemic brain insult [36-38], developmental CNS disease [39], multiple sclerosis [40], diffuse axonal injury (DAI) [41], and spinal cord lesions [42]. Most of these studies have attempted to predict the patients' outcome/prognosis, and the results appear promising.

### Application to neuroscience

Tractography is not only a clinical tool; it is also widely used in the field of neuroscience. Many researchers, including the present authors, expect this field to be fruitful. At the same time, it is believed that the interpretation of the results should be done with caution, as there is not yet an effective reality check on this technique [43].

► **Tractography has been used for pre-operative assessment of eloquent white matter tracts.**

► **Tractography is not only a clinical tool. It is also widely used in neuroscience.**

One should still rely on the classical neuroanatomy description at the histological level when looking at the results. It is apparent that all medical imaging has limitations, and this is true for DTI. Especially important will be the spatial resolution of this technique. With tractography, one is limited to looking at the system at a completely different scale from the histology.

## The future

As illustrated in this article, there have been remarkable evolutions in both the imaging and post-processing aspects of this technique in the past decade. It is apparent that the environment for using this technique clinically is improving each year. However, performing the advanced techniques that are robust with respect to crossing fibers is still time consuming [11, 12]. The imaging time for these advanced techniques must become even shorter for clinical use.

A more objective way of analyzing tractographic results may be needed in the future. Current analysis is limited to qualitative intra-subject

comparisons, such as the contralateral ratio of the number of fibers depicted or the anisotropy index. These factors can be easily affected by image quality, and, thus, it is often difficult to use the information for direct inter-subject comparisons.

A better way of representing the pathological processes of fibers is necessary. For instance, the anisotropy reduction can be driven by increased radial diffusivity (that is, increased diffusion perpendicular to the principal diffusion direction) or reduced axial diffusion. Both of these conditions would represent different pathological processes. It would be ideal if we would be able to handle these separately and attribute them to specific pathological processes. This would potentially expand the quality of the information obtained.

Standardization of the technique may be necessary in the future to allow for clinical studies of a larger scale. When this happens, it could be the sign that the technique has matured and truly established itself in this field ■

► **The environment for clinical application of tractography is improving each year.**

## References

- [1] Mori S, Crain BJ, Chacko VP, van Zijl PCM. *Three-dimensional Tracking of Axonal Projections in the Brain by Magnetic Resonance Imaging*. *Ann Neurol*. 1999; 45(2): 265-269.
- [2] Witwer BP, Moftakhar R, Hasan KM, Deshmukh P, Haughton V, Field A, et al. *Diffusion-Tensor Imaging of White Matter Tracts in Patients with Cerebral Neoplasm*. *J Neurosurg*. 2002; 97(3): 568-575.
- [3] Wiegell MR, Larsson HB, Wedeen VJ. *Fiber Crossing in Human Brain Depicted with Diffusion Tensor MR Imaging*. *Radiology*. 2000; 217(3): 897-903.
- [4] Nimsy C, Ganslandt O, Merhof D, Sorensen AG, Fahlbusch R. *Intraoperative Visualization of the Pyramidal Tract by Diffusion-Tensor-Imaging-Based Fiber Tracking*. *Neuroimage*. 2006; 30(4): 1219-1229.
- [5] Yamada K, Kizu O, Mori S, Ito H, Nakamura H, Yuen S, et al. *Brain Fiber Tracking with Clinically Feasible Diffusion-Tensor Imaging for Fiber Tracking*. *Radiology*. 2003; 227(1): 295-301.
- [6] Okada T, Miki Y, Kikuta K, Mikuni N, Urayama, Fushimi Y, et al. *Diffusion Tensor Fiber Tractography for Arteriovenous Malformations: Quantitative Analyses to Evaluate the Corticospinal Tract and Optic Radiation*. *AJNR Am J Neuroradiol*. 2007; 28: 1107-1113.
- [7] Xue R, van Zijl PCM, Crain BJ, Solaiyappan M, Mori S. *In vivo Three-Dimensional Reconstruction of Rat Brain Axonal Projections by Diffusion Tensor Imaging*. *Magn. Reson Med*. 1999; 42(6): 1123-1127.
- [8] Conturo TE, Lori NF, Cull TS, Akbudak E, Snyder AZ, Shimony JS, et al. *Tracking Neuronal Fiber Pathways in the Living Human Brain*. *Proc Natl Acad. Sci USA*. 1999; 96(18): 10422-10427.
- [9] Yamada K, Sakai K, Hoogenraad FGC, Holthuisen R, Akazawa K, Ito H, et al. *Multitensor Tractography Enables Better Depiction of Motor Pathways: Initial Clinical Experience Using Diffusion-Weighted MR Imaging with Standard B-value*. *AJNR Am J Neuroradiol* 2007; 28(9): 1668-1673.
- [10] Oouchi H, Yamada K, Sakai K, Kizu O, Kubota T, Ito H, et al. *Diffusion Anisotropy Measurement of Brain White Matter is affected by Voxel Size; Underestimation Occurs in Areas with Crossing Fibers*. *AJNR Am J Neuroradiol*. 2007; 28: 1102-1106.
- [11] Tuch DS, Reese TG, Wiegell MR, Makris N, Belliveau JW, Wedeen VJ. *High Angular Resolution Diffusion Imaging Reveals Intravoxel White Matter Fiber Heterogeneity*. *Magn Reson Med*. 2002; 48(4): 577-582.

- [12] Frank LR. *Characterization of Anisotropy in High Angular Resolution Diffusion-Weighted MRI*. Magn Reson Med. 2002; 47(6): 1083-1099.
- [13] Behrens TE, Berg HJ, Jbabdi S, Rushworth MF, Woolrich MW. *Probabilistic Diffusion Tractography with Multiple Fiber Orientations: What can we gain?* Neuroimage. 2007; 34(1): 144-155.
- [14] Behrens TE, Johansen-Berg H, Woolrich MW, Smith SM, Wheeler-Kingshott CAM, Boulby PA, et al. *Non-Invasive Mapping of Connections between Human Thalamus and Cortex using Diffusion Imaging*. Nat Neurosci. 2003; 6: 750-757.
- [15] Qazi AA, Radmanesh A, O'Donnell L, Kindlmann G, Peled S, Whalen S, et al. *Resolving Crossings in the Corticospinal Tract by Two-Tensor Streamline Tractography: Method and Clinical Assessment using fMRI*. Neuroimage. 2008; Jul 8. [Epub In Press.].
- [16] Lin CP, Tseng WY, Cheng HC, Chen JH. *Validation of Diffusion Tensor Magnetic Resonance Axonal Fiber Imaging with Registered Manganese-Enhanced Optic Tracts*. Neuroimage. 2001; 14(5): 1035-1047.
- [17] Ciccarelli O, Toosy AT, Parker GJM, Wheeler-Kingshott CAM, Barker GJ, Miller DH, et al. *Diffusion Tractography Based Group Mapping of Major White-Matter Pathways in the Human Brain*. Neuroimage. 2003; 19(4): 1545-1555.
- [18] Parker GJ, Stephan KE, Barker GJ, Rowe JB, MacManus DG, Wheeler-Kingshott CA, et al. *Initial Demonstration of In Vivo Tracing of Axonal Projections in the Macaque Brain and Comparison with the Human Brain using Diffusion Tensor Imaging and Fast Marching Tractography*. Neuroimage. 2002; 15(15): 797-809.
- [19] Kinoshita M, Yamada K, Hashimoto N, Kato A, Izumoto S, Baba T, et al. *Fiber Tracking does not Accurately Estimate Size of Fiber Bundle in Pathological Condition: Initial Neurosurgical Experience using Neuronavigation and Subcortical White Matter Stimulation*. Neuroimage. 2005; 25(2): 424-429.
- [20] Coenen VA, Krings T, Mayfrank L, Polin RS, Reinges MHT, Thron A, et al. *Three-Dimensional Visualization of the Pyramidal Tract in a Neuronavigation System during Brain Tumor Surgery: First Experiences and Technical Note*. Neurosurgery. 2001; 49(1): 86-93.
- [21] Hendler T, Pianka P, Sigal M, Kafri M, Ben-Bashat D, Constantini S, et al. *Delineating Gray and White Matter Involvement in Brain Lesions: Three-Dimensional Alignment of Functional Magnetic Resonance and Diffusion-Tensor Imaging*. J Neurosurg. 2003; 99(6): 1018-1027.
- [22] Holodny AI, Schwartz TH, Ollenschleger M, Liu WC, Schulder M. *Tumor involvement of the corticospinal tract: diffusion magnetic resonance tractography with intraoperative correlation*. J Neurosurg. 2001; 95(6): 1082.
- [23] Yamamoto A, Miki Y, Urayama S, Fushimi Y, Okada T, Hanakawa T, et al. *Diffusion Tensor Fiber Tractography of the Optic Radiation: Analysis with 6-, 12-, 40-, and 81-Directional Motion-Probing Gradients, A Preliminary Study*. AJNR Am J Neuroradiol. 2007; 28(1): 92-96.
- [24] Yamamoto T, Yamada K, Nishimura T, Kinoshita S. *Tractography to Depict Three Layers of Visual Field Trajectories to the Calcarine Gyri*. Am J Ophthalmol. 2005; 140(5): 781-785.
- [25] Taoka T, Sakamoto M, Nakagawa H, Hakase H, Iwasaki S, Takayama K, et al. *Diffusion Tensor Tractography of the Meyer Loop in Cases of Temporal Lobe Resection for Temporal Lobe Epilepsy: Correlation between Postsurgical Visual Field Defect and Anterior Limit of Meyer Loop on Tractography*. AJNR Am J Neuroradiol. 2008; 29(7): 1329-1334.
- [26] Kunimatsu A, Aoki S, Masutani Y, Abe O, Mori H, Ohtomo K. *Three Dimensional White Matter Tractography by Diffusion Tensor Imaging in Ischemic Stroke Involving the Corticospinal Tract*. Neuroradiology. 2003; 45(8): 532-535.
- [27] Yamada K, Mori S, Nakamura H, Ito H, Kizu O, Shiga K, et al. *Fiber-Tracking Method Reveals Sensorimotor Pathway Involvement in Stroke Patients*. Stroke. 2003; 34(9): e159-e162.
- [28] Konishi J, Yamada K, Kizu O, Ito H, Sugimura K, Yoshikawa K, et al. *MR Tractography for the Evaluation of the Functional Recovery from Lenticulostriate Infarct*. Neurology. 2005; 64(1): 108-113.
- [29] Nelles M, Gieseke J, Flacke S, Lachenmayer L, Schild HH, Urbach H. *Diffusion Tensor Pyramidal Tractography in Patients with Anterior Choroidal Artery Infarcts*. AJNR Am J Neuroradiol. 2008; 29(3): 488-493.
- [30] Kunimatsu A, Itoh D, Nakata Y, Kunimatsu N, Aoki S, Masutani Y, et al. *Utilization of Diffusion Tensor Tractography in Combination with Spatial Normalization to Assess Involvement of the Corticospinal Tract in Capsular/Pericapsular Stroke: Feasibility and clinical implications*. J Magn Reson Imaging. 2007; 26(6): 1399-1404.
- [31] Catani M, Mesulam M. *The Arcuate Fasciculus and the Disconnection Theme in Language and Aphasia: History and Current State*. Cortex. 2008; 44(8): 953-961.
- [32] Yamada K, Nagakane T, Mizuno T, Hosomi A, Nakagawa M, Nishimura T. *MR Tractography Depicting Damage to the Arcuate Fasciculus in a Patient with Conduction Aphasia*. Neurology. 2007; 68(10):789.
- [33] Breier JI, Hasan KM, Zhang W, Men D, Papanicolaou AC. *Language Dysfunction after Stroke and Damage to White Matter Tracts Evaluated using Diffusion Tensor Imaging*. AJNR Am J Neuroradiol. 2008; 29(3): 483-487.
- [34] Aoki S, Iwata NK, Masutani Y, Yoshida M, Abe O, Ugawa Y, et al. *Quantitative Evaluation of the Pyramidal Tract Segmented by Diffusion Tensor Tractography: Feasibility Study in Patients with Amyotrophic Lateral Sclerosis*. Radiat Med. 2005; 23(3): 195-199.

- [35] Abe O, Yamada H, Masutani Y, Aoki S, Kunimatsu A, Yamasue H, et al. *Amyotrophic Lateral Sclerosis: Diffusion Tensor Tractography and Voxel-Based Analysis*. NMR Biomed. 2004; 17(6): 411-416.
- [36] Yoo S-S, Park H-J, Soul JS, Mamata H, Park H, Westin C-F, et al. *In Vivo Visualization of White Matter Fiber Tracts of Preterm- and Term-infant Brains with Diffusion Tensor Magnetic Resonance Imaging*. Invest Radiol. 2005; 40(2): 110-115.
- [37] Hoon AH Jr, Lawrie WT Jr, Melhem ER, Reinhard EM, van Zijl PCM, Solaiyappan M, et al. *Diffusion Tensor Imaging of Periventricular Leukomalacia shows Affected Sensory Cortex White Matter Pathways*. Neurology. 2002; 59(5): 752-756.
- [38] Murakami A, Morimoto M, Yamada K, Kizu O, Nishimura A, Nishimura T, et al. *Fiber-Tracking Techniques can Predict the Degree of Neurologic Impairment for Periventricular Leukomalacia*. Pediatrics. 2008; 122(3): 500-506.
- [39] Lee S-K, Kim DI, Kim J, Kim JD, Kim HD, Kim DS, et al. *Diffusion-Tensor MR Imaging and Fiber Tractography: a New Method of Describing Aberrant Fiber Connections in Developmental CNS Anomalies*. Radiographics. 2005; 25(1): 53-68.
- [40] Pagani E, Filippi M, Rocca MA, Horsfield MA. *A Method for Obtaining Tract-Specific Diffusion Tensor MRI Measurements in the Presence of Disease: Application to Patients with Clinically Isolated Syndromes Suggestive of Multiple Sclerosis*. Neuroimage. 2005; 26(1): 258-265.
- [41] Le TH, Mukherjee P, Henry RG, Berman JI, Ware M, Manley GT. *Diffusion Tensor Imaging with Three-Dimensional Fiber Tractography of Traumatic Axonal Shearing Injury: an Imaging Correlate for the Posterior Callosal "Disconnection" Syndrome: Case Report*. Neurosurgery. 2005; 56(1): 189.
- [42] Tsuchiya K, Fujikawa A, Suzuki Y. *Diffusion Tractography of the Cervical Spinal Cord by using Parallel Imaging*. AJNR Am J Neuroradiol. 2005; 26(2): 398-400.
- [43] Yamada K. *Diffusion Tensor Tractography should be used with Caution*. Proc Natl Acad Sci USA. 2009; 106(7): E14.

# Clinical applications of diffusion tensor imaging in children

**N. K. Rollins**  
**J. M. Chia**

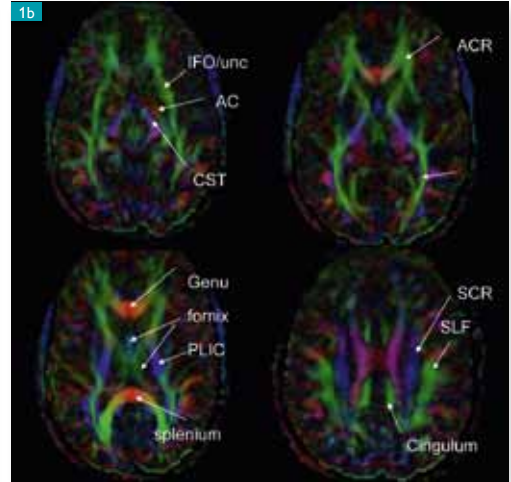
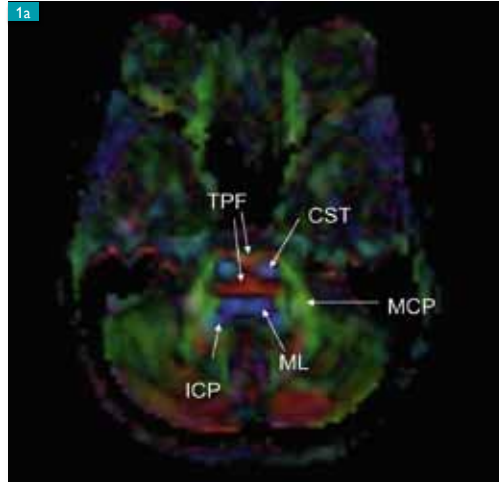
Children's Medical Center of Dallas and the University of Texas,  
Southwestern Medical Center Dallas, TX, USA.

Figure 1. Axial directionally encoded maps of major white matter tracts in the fully myelinated brain

Figure 1a. Color map through the brainstem shows the larger tracts. MCP = middle cerebellar peduncle, ICP = inferior cerebellar peduncle, CST = corticospinal tracts, TPF = transverse pontine fibers.

Figure 1b. Composite of axial color maps through the major white matter tracts in fully myelinated brain.

IFO = inferior fronto-occipital fasciculus,  
ILF = inferior longitudinal fasciculus,  
unc = uncinata,  
SCR = superior corona radiata,  
PLIC = posterior limb of the internal capsule,  
SLF = superior longitudinal fasciculus,  
AC = anterior commissure,  
ACR = anterior corona radiata.



Diffusion tensor imaging (DTI) is a non-invasive tool for studying white matter composition. The contrast in DTI is provided by water movement within tissues [1, 2]. Diffusion tensor metrics are surrogate markers of normal age-related maturational changes and disease states that affect the composition of white matter, thereby affecting the diffusion of water. It is common for DTI to be processed using a single-tensor model; that is, to assume there is only one dominant fiber direction within each voxel.

The most commonly described parameter of water diffusion is fractional anisotropy (FA). FA is a unit-less value ranging from 0 to 1. Increasing anisotropy is indicative of preferential directional water diffusion [2, 3]. The eigenvalues  $\lambda_1$ ,  $\lambda_2$  and  $\lambda_3$  denote the major individual directional vectors of water diffusion. They are used to derive the FA. When the eigenvalues are equal, diffusion of water is isotropic and FA approaches zero [1-3]. When the eigenvalues differ significantly; the diffusion of water is anisotropic and FA increases.

By definition and regardless of the direction of water diffusion, the eigenvalue parallel to the dominant axonal orientation is the largest eigenvalue and is described by  $\lambda_1$ . It is also referred to as the axial diffusivity. The smaller eigenvalues  $\lambda_2$  and  $\lambda_3$  define the radial diffusivity that describes the movement of water in directions perpendicular to the dominant axonal orientation.

Decreases in FA may be due to lower axial diffusivity that results from alterations in axonal structure or to the increased radial diffusivity that results from differences in myelin, or to some combination of both [3-5]. FA is therefore a nonspecific indicator of changes in white matter composition. In particular, in voxels containing more than one fiber, the FA calculation is inherently inaccurate, and this can lead to misinterpretation of changes.

Unlike routine MR imaging in which white matter tracts are visually indistinguishable, DTI allows the larger individual white matter tracts to be visualized as discrete anatomic structures that can be identified on directionally encoded color maps [6-8]. By definition, white matter tracts oriented left-right are seen as red, those oriented cephalocaudad are seen as blue and those oriented anterior-posterior are seen as green.

White matter tracts readily visualized by DTI include (Figures 1a and 1b):

- brainstem
- projection
- association
- limbic fibers
- commissural fibers.

Fiber tract reconstruction may be done using probabilistic tractography, which estimates the probability of fiber connections, or the continuous fiber tracking method, which traces pixels within a certain area based on anisotropy

► **Diffusion tensor imaging (DTI) is a non-invasive tool for studying white matter composition.**

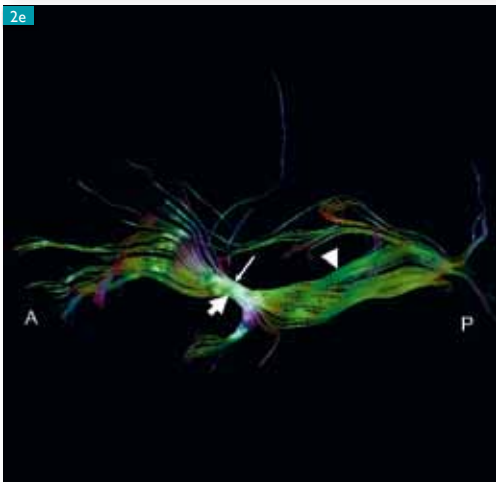
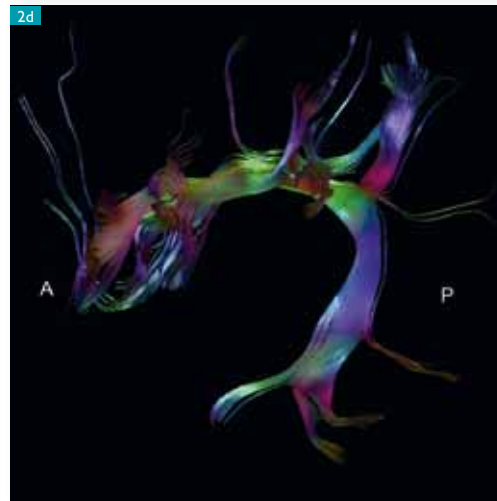
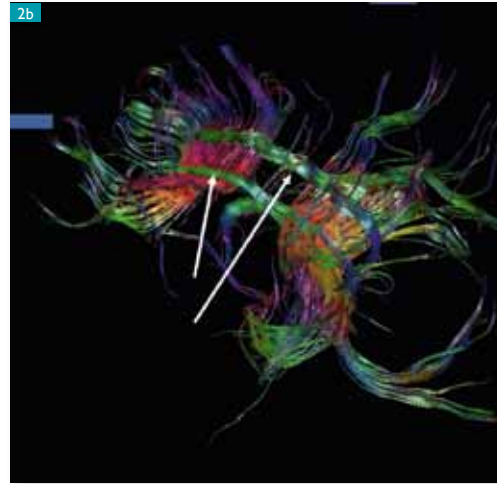
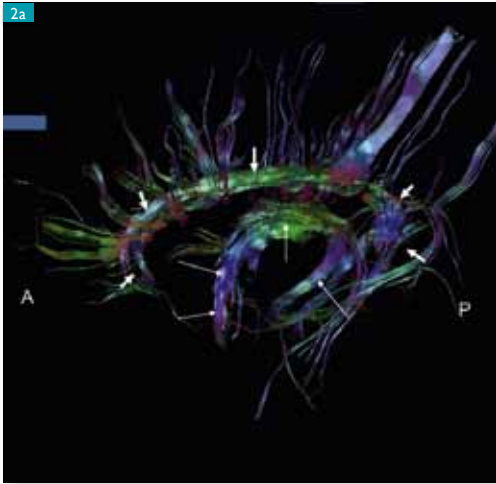


Figure 2. Tractography of white matter tracts.



Figure 2a. Normal limbic arches. Small arrows indicate the cingulum and long arrows the fornices.



Figure 2b. Oblique axial image of the paired cingulum (arrows) above the corpus callosum. Some of the callosal fibers have been removed.



Figure 2c. Coronal view of the CST. Within the cerebral hemispheres, only that portion of the CST involved in lower extremity function is visible; the fibers to the hand and face are not detectable by DTI due to the presence of other crossing fiber bundles.



Figure 2d. Sagittal view of the IFO and uncinata as seen by FT. The IFO and the uncinata are a white matter bridge between the temporal and frontal lobes. The IFO has a long, anterior-posterior course in the temporal lobe and is contiguous with the ILF (arrowheads) within the occipital regions. The uncinata fasciculus (large arrow) situated in the anterior part of the temporal lobe merges with the fibers of the IFO (long arrow).



Figure 2e. Sagittal view of the SLF, which connects the frontal, parietal, and temporal cortex

[9]. In clinical practice, tractography that utilizes the FACT (fiber association by continuous tracking method) [8] algorithm is more widely used. Examples of larger white matter tracts as seen by FT in normal children are shown in (Figures 2a to 2e).

Tractography is a mathematical estimation of white matter tracts rather than a precise anatomical depiction and fibers may appear disproportionately large due to higher FA. In addition, transections or thinning of tracts may

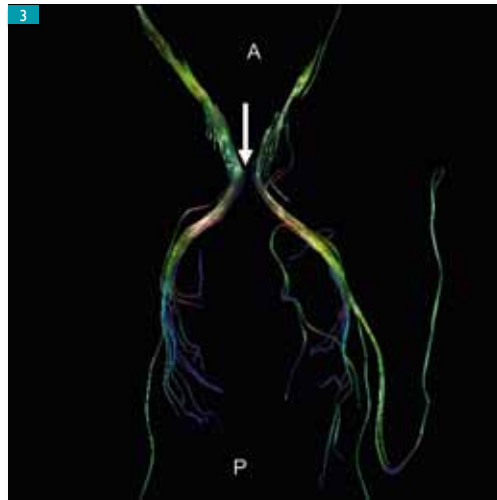
be caused either by crossing/kissing fibers, or by artifacts in the underlying data, for example, a hemorrhage.

The images derived from diffusion tensor imaging reflect the averaged water diffusion within a pixel and not the actual axonal structures. Examples of the limitations of tractography are seen in the optic pathways where the chiasm is not visible (Figure 3) as two fibers with a crossing trajectory are seen as “kissing” (><) rather than “crossing”(><) [7, 8, 9].

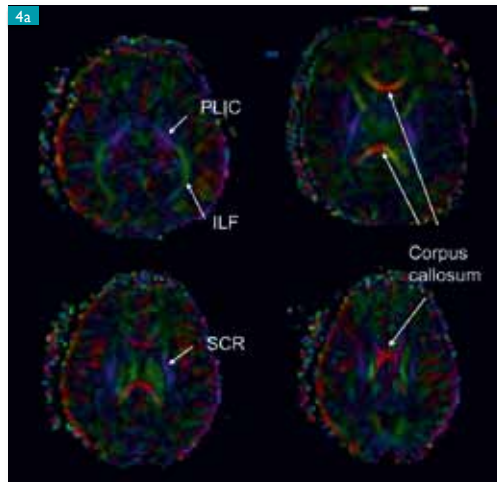
The mathematical tensor calculations are biased by the dominant axonal component; smaller tracts oriented obliquely or even perpendicular to large white matter projections may be missed by DTI. The minimum spatial voxel resolution in DTI data provided by current MR technology is in the order of a millimeter or more [8, 9].

In order to reconstruct multiple crossing fiber orientations within regions of complex white matter architecture, dozens or even hundreds of uniformly distributed diffusion directions in 3D space must be acquired to resolve intra voxel fibers orientated in different directions. At present, these large data sets are cumbersome to

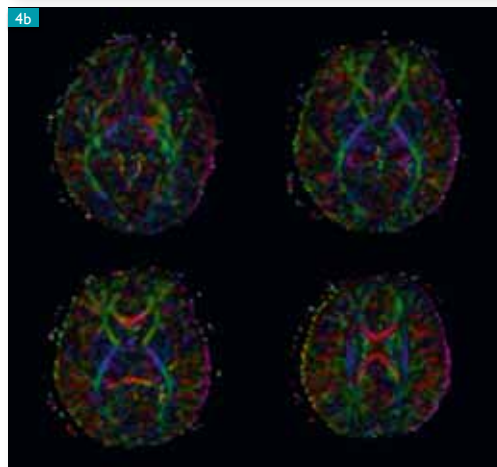
▶ Figure 3. Axial view of the optic pathways. Note apparent absence of the chiasm (arrow) due to insensitivity of DTI/FT to crossing fibers.



▶ Figure 4. Color maps of normal three-day-old and five-month-old children.



▶ Figure 4a. At birth, the PLIC, ILF, superior corona radiata (SCR), and corpus callosum are visible on the color maps.



▶ Figure 4b. By five months of age, the IFO-uncinate and anterior corona radiate are visible. The other tracts have thickened and become more obvious. Compare these images to those of the fully myelinated brain in Fig. 1b.

display and have limited clinical application although the potential research applications are enormous in terms of understanding white matter structure in normal and disease states.

### Assessment of the pediatric brain using DTI

Diffusion tensor imaging is sensitive to the change in the white matter that precede myelination; that is, increasing anisotropy [10]. Potential explanations for increasing anisotropy

include development of axolemmal membranes and early wrapping of axons by oligodendroglial processes with increases in fiber diameter and cell packing density [10, 11]. The net result of these macromolecular changes is impedance of physiologic movement of water perpendicular to the axon and accelerated diffusion parallel to the axons.

During normal early childhood, FA within white matter increases because of either disproportionate decreases in the three eigenvalues, or increases in axial diffusivity along with decreases in radial diffusivity [10, 11]. Age-related increases in FA are most pronounced during the first two years of life and continue to lesser degrees in regions of the brain involved in cognition and higher-order functioning [11, 12]. Different white matter tracts mature at different rates and the fronto-temporal white matter appears to develop more slowly than other regions.

As cerebral white matter matures, changes are visible on the anisotropy maps as well as directionally encoded color maps. Examples of anisotropy and color maps for infants and children of increasing ages are shown in (Figures 4a and 4b; compare with Figure 1b). Certain white matter tracts are identifiable on the color maps at in very young children, although the white matter tracts are thinner and have lower anisotropy than in older children.

These tracts include the internal capsules, corpus callosum, fornix and cingulum, inferior fronto-occipital and inferior longitudinal fasciculus. At birth, the anisotropy of peripheral white matter is close to that of cortex; by three months the anisotropy of the U-fibers has matured sufficiently that subcortical white matter is identifiable on the color maps.

The most accurate and precise means of quantifying the diffusion tensor data, which is most often the FA, is controversial. Different methodologies include voxel-based analysis, tractography, region of interest (ROI) analysis, and tract-based spatial statistics (TBSS) [9, 13, 14]. TBSS is an automated observer-independent method of aligning fractional anisotropy images from multiple subjects to allow group wise comparisons of DTI data [13].

Voxel-based morphometry is observer independent and allows whole brain comparison of groups of subject [14]. However, the image data must be spatially normalized and smoothed, which can blur differences between subjects or groups. Tractography takes bulk-averaged tissue properties in each voxel and through

mathematical modeling infers the dominant fiber orientation within each voxel [9].

Problems using tractography include insensitivity to crossing fibers, limited spatial resolution during image acquisition, and the inherent mathematical uncertainty [1, 2, 9]. ROI analysis is tedious, subject to sampling error, imprecise, and insensitive to changes occurring outside the region of interest but manual measures may show additional important variances.

FA decreases in most disease states that affect white matter; changes in FA values are therefore not specific for any disease entity. Alterations in white matter anisotropy are nonetheless being studied in many conditions some of which are unique to children [16, 17, 18].

### Applications of DTI in acquired white matter diseases

DTI has potential application in children with strokes, brain tumors, trauma, and metabolic and storage disorders. In the acute setting, DTI usually lacks the sensitivity to restrict diffusion of diffusion-weighted imaging and it is therefore not used as a diagnostic tool. In hyper acute strokes in neonates, the acutely infarcted brain may show increased anisotropy rather than lower FA in addition to restricted diffusion (Figure 5).

In the subacute setting, DTI may show loss of integrity of the regional projection and association fibers that may be more extensive than the actual infarction as well as early Wallerian degeneration. Before the age of five years, the pediatric brain retains a sufficient degree of plasticity. Considerable function may be regained after a stroke; significantly more than is usually seen after a cerebrovascular accident occurs in an adult.

In combination with functional MR imaging which can be used to identify secondary somatosensory cortex recruited after a stroke, DTI may provide insight as to how the regional white matter “rewires” to connect the uninjured brain. Children with closed head injury are being studied using fMRI and DTI to evaluate the severity of injury, the implications for cognitive performance, and brain plasticity.

An important potential application of DTI is in children with tumors in whom operative morbidity may be lessened by the avoidance of intact white matter tracts, especially in deep hemispheric and brainstem tumors (Figure 6a and 6b) [20]. DTI has limited application in

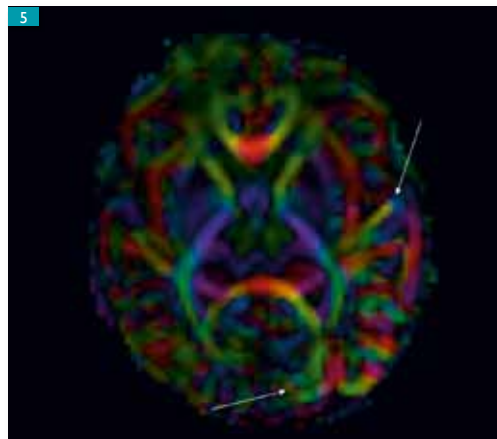


Figure 5. Directionally encoded color map in a neonate with a new infarct in the left parietal lobe. Note increased anisotropy within the acutely infarcted tissue (arrows).

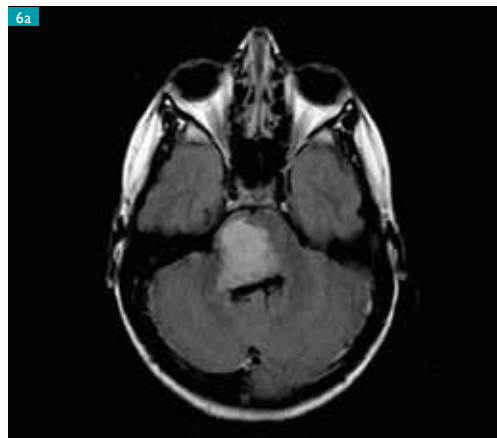


Figure 6. Six-year-old with tumor arising from the brain stem.

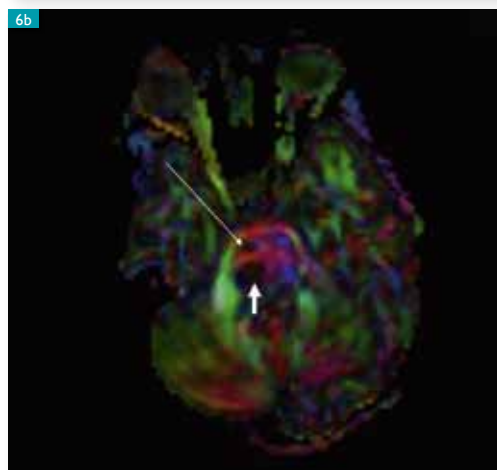


Figure 6a. Axial T2 image shows a tumor within the right middle cerebellar peduncle.

Figure 6b. Axial color map shows loss of anisotropy within the right medial lemniscus resulting in lack of blue (short arrow). The right CST (long arrow) is attenuated and has diminished anisotropy.

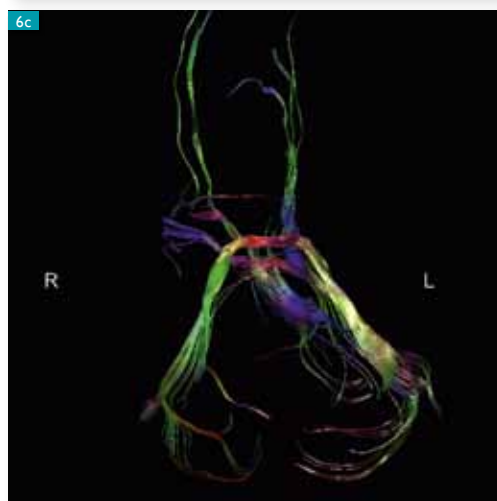


Figure 6c. Coronal image derived from tractography shows leftward displacement of brainstem tracts.

Figure 7. Color map and tractography of limbic structures in a seven-day-old with callosal agenesis.

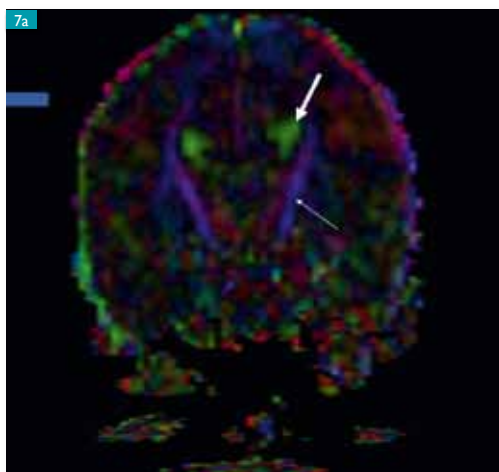


Figure 7a. Coronal color map shows cingulum, fornix, and Probst bundles fused together into a triangular-shaped structure (thick arrow). Thin arrow indicates the CST.

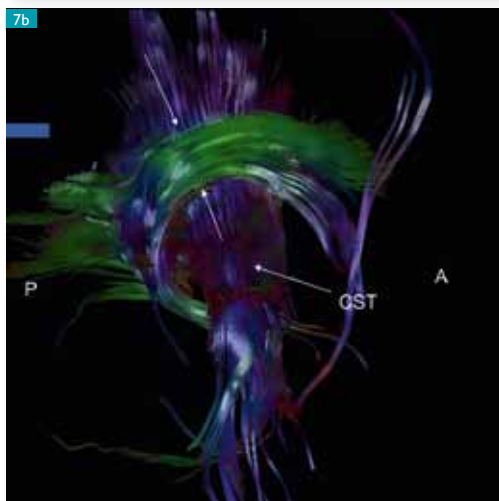


Figure 7b. Sagittal projection of the fused inner and outer limbic arches (arrows) derived from FT.

Figure 8. Near-total callosal agenesis seen by tractography.



Figure 8a. Note rudimentary corpus callosum (arrow) dorsal to the expected location of the commissural plate.

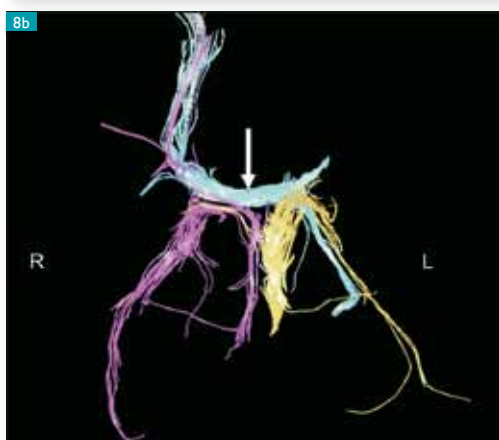


Figure 8b. Tractography of the rudimentary callosal fibers (arrow) depicted in blue shows apparent connections between the right parasagittal neocortical axons and the left fornix. The forniceal fibers are depicted in orange. The pink right-sided forniceal fibers appear intertwined with the fibers of the right parasagittal neocortex.

extra-axial tumors and those arising from within the ventricles, as tumors in these locations as a rule, do not affect the regional white matter.

### Application of DTI to congenital brain malformations

DTI can be used in the study of congenital brain malformations associated with abnormalities of larger white matter tracts. There are scattered reports of cerebral malformations studied with DTI including callosal agenesis, cortical dysplasia, holoprosencephaly, lissencephaly, and the Chiari II malformation [20-23] (Figures 7 to 13). DTI and FT may provide detail of white matter tracts not possible with pathologic dissection as dissection by its nature disrupts fibers and cannot distinguish adjacent white matter tracts.

#### Callosal agenesis/dysgenesis

Congenital anomalies of the corpus callosum include complete agenesis, partial agenesis with preservation of the rostral corpus callosum, and variable dysgenesis ranging from hypoplasia to gross thickening. In callosal agenesis, the bundles of Probst when present are seen as longitudinally oriented fibers coursing along the medial wall of the lateral ventricles (Figure 7a) [20]. The fornices are dysplastic, often deficient, and widely separated; the Probst bundles are fused with the rudimentary cingulum and the dysplastic fornices (Figure 7b).

In partial callosal agenesis, the preserved callosal fibers may appear by fiber tractography to connect both neocortex and archicortex (Figures 8a and 8b) suggesting disordered axonal migration. DTI also suggests that in some patients, gross thickening of a dysplastic corpus callosum may be due to anomalous course of supracallosal fibers (Figures 9a and 9b).

#### Cortical dysplasia

Areas of cortical dysplasia (Figures 10a and 10b) may be difficult to identify by DTI given the relatively poor spatial resolution of DTI, and the low fractional anisotropy of subcortical white matter even in the fully myelinated brain. Identification of cortical dysplasia using DTI is even more problematic in the brain of the infant and young child in whom myelination of peripheral white matter is incomplete.

In the fully myelinated brain, DTI may show areas of reduced anisotropy and increased diffusivity within the region of dysplastic brain. Some patients also have abnormalities of diffusion metrics in cerebral parenchyma that appears normal on conventional T1- and

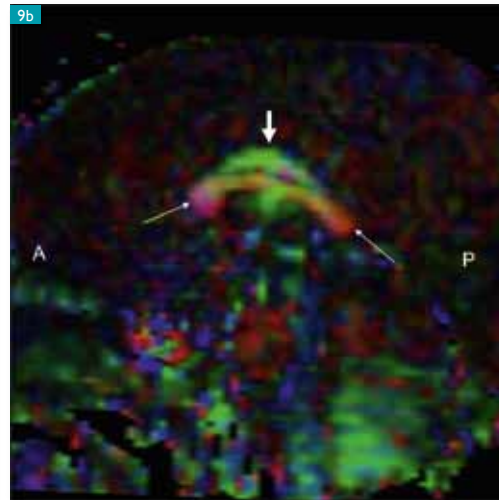


Figure 9. Callosal dysgenesis as seen by DTI.



Figure 9a. Sagittal T1 image from a two-year-old with developmental delay and seizures shows marked thickening of the mid portion of a foreshortened corpus callosum.



Figure 9b. The sagittal color map shows the corpus callosum (thin arrows) seems embedded in anomalous fibers oriented preferentially dorsal-ventral and therefore seen as green (thick arrow).

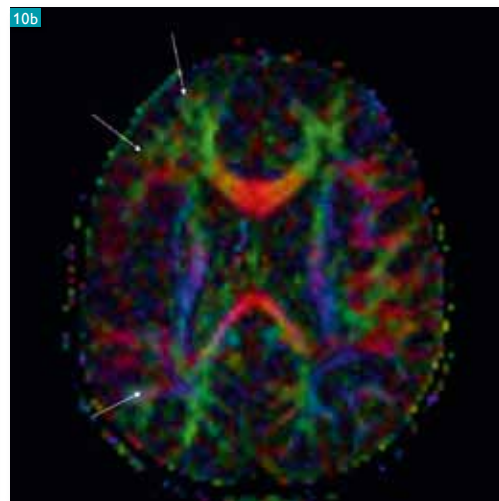


Figure 10. Right peri-Sylvian cortical dysplasia as seen by DTI.



Figure 10a. Axial T2 images show extensive cortical dysplasia.



Figure 10b. On the color map, note the disorganized white matter (arrows) of the right peri-Sylvian region, which is more extensive than the cortical abnormalities. Compare with the white matter of the contralateral cerebrum.

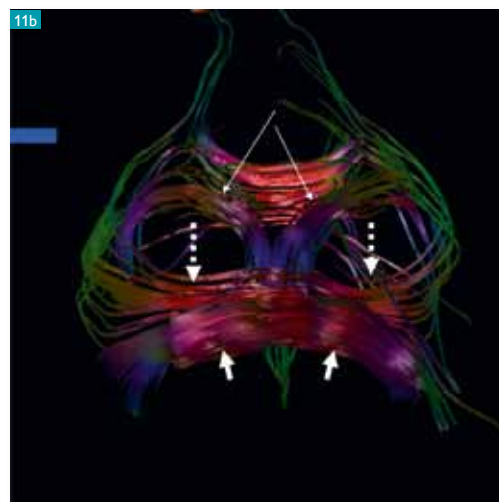
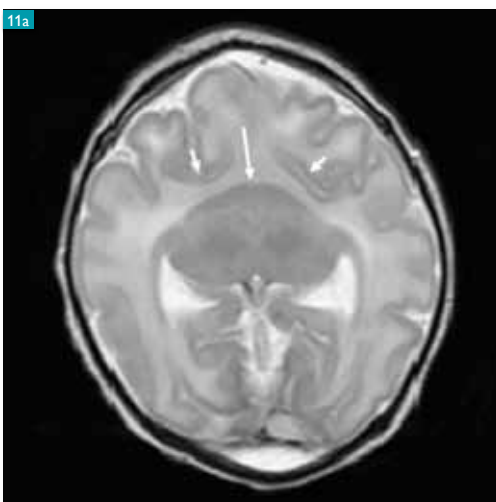


Figure 11. DTI in infant with semilobar holoprosencephaly.



Figure 11a. Axial T2 image shows fusion of the thalami and caudates (arrow). The Sylvian fissures (short arrows) are displaced ventrally.



Figure 11b. Coronal image derived from FT. The fused caudates (short arrows) are seen as a thick red band ventral to tract assumed to be the fronto-occipital fasciculus (dotted arrows). Note the thickened forniceal structures (long arrows) not visible with routine MR imaging.

T2-weighted images. Performing a voxel-by-voxel comparison of brains with cortical dysplasia to those of normal controls requires normalization of all brains into a common space in order to minimize the overall variability in size and shape between brains. As in functional MR imaging, the brains are normalized to Talairach space using one of many software programs available in the public and private domain.

### Holoprosencephaly

Holoprosencephaly is a complex malformation of the brain and face characterized with respect to the degree of formation of the ventricular system as alobar, semilobar, lobar, or of the middle-hemisphere variant. Holoprosencephaly is due to failure of induction or abnormal fusion of normally paired and separate neocortex, caudates, and claustrum [21].

Figure 12. DTI in infant with lissencephaly

▶ Figure 12 a. Axial T2 image shows wide vertically oriented Sylvian fissures, lack of sulcation, linear gray/white junction, thickened cortex and thinned white matter.



▶▶ Figure 12b. Axial image derived from FT shows thick brush-like fibers (arrows) corresponding to the thick densely cellular fourth layer of neurons in arrested migration having a persistent parallel orientation.

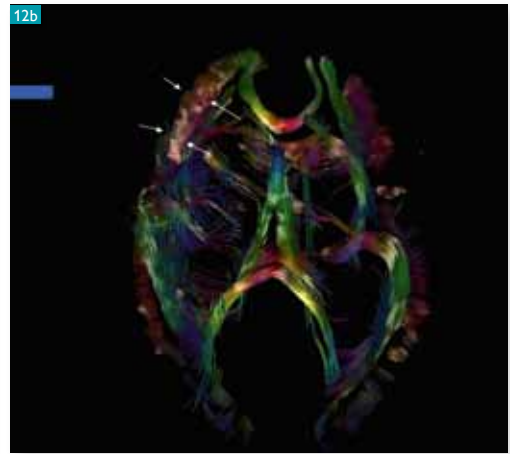
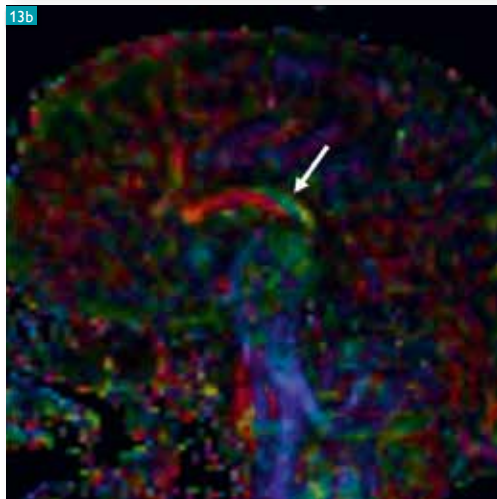


Figure 13. Dysplastic corpus callosum in a patient with Chiari II malformation.

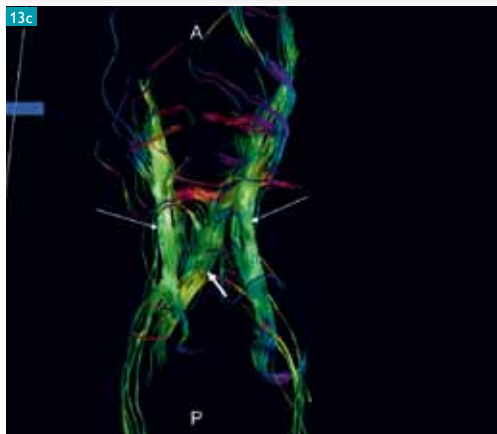
▶ Figure 13a. Sagittal T2 image shows the corpus callosum is foreshortened and somewhat nodular



▶ Figure 13b. Sagittal color map shows anomalous supracallosal fibers (arrow).



▶ Figure 13c. Axial top-down image from FT shows the cingulum (long arrows) and the anomalous supracallosal fiber (arrow).



In an example of semilobar holoprosencephaly, tractography (Figure 11) shows large white matter tracts within the cerebrum not apparent on routine MR imaging. With large symmetric fiber bundles having the expected course of the frontooccipital fasciculus connected across the midline in the subfrontal region and dysplastic forniceal-like structures embedded in the basal ganglia (Figures 11a and 11b) [21]. As seen by DTI, hypoplasia of the middle cerebellar peduncles correlates with the severity of frontal lobe underdevelopment and increasing severity of the prosencephalic malformation.

### Lissencephaly

Lissencephaly is an uncommon cerebral malformation characterized by thickened and undersulcated cortex and layers of gray matter embedded within deep white matter. The cerebral cortex is normally composed of six horizontal cell layers while the lissencephalic cortex has four cell layers. The two most superficial layers of cortex in the lissencephalic brain are formed by the neurons that migrated normally early in gestation, while the deeper layers are composed of neurons in migratory arrest.

The third cell layer contains astrocytes, oligodendroglial cells, and dysplastic neurons, and the thickest, densely cellular fourth layer shows radial orientation, limited cellular differentiation, and no lamination. DTI in lissencephaly shows peripheral subcortical brush-like fibers corresponding to the densely cellular fourth layer. The parallel organization of glial fibers in the cerebral cortex that normally involutes when intra-cortical connectivity is established later in gestation in the normal brain persists in lissencephaly. (Figures 12a and 12b) [22]. As in many other severe cerebral malformations, the limbic system in lissencephaly is dysplastic.

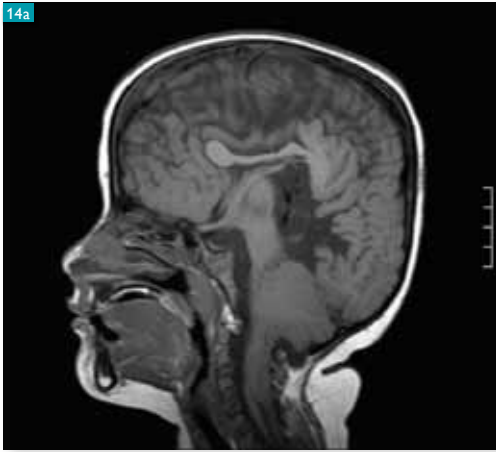


Figure 14. Severe hypoplasia in a patient with Chiari II malformation.

Figure 14a. Sagittal T1 image shows a constricted posterior fossa, cerebellar hypoplasia, and an elongated brainstem that lacks the belly of the pons.

Figure 14b. Sagittal image derived from FT. Note absence of the transverse pontine fibers that should be seen as bundles of red along the ventral aspect of the brainstem.

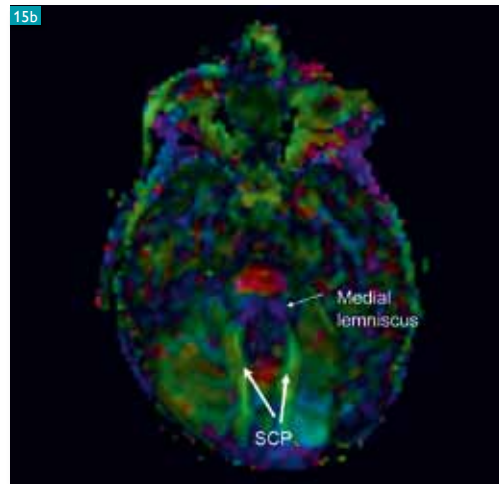


Figure 15. Joubert syndrome as seen by DT.

Figure 15a. Axial T2 image shows vermian hypoplasia and enlarged superior cerebellar peduncles (arrows).

Figure 15b. Axial color map shows the CST and medial lemniscus are not separated by transverse pontine fibers. Compare with Figure 1a. Arrows indicate enlarged superior cerebellar peduncles.

### Chiari II malformation

The Chiari II malformation is a relatively common CNS malformation almost invariably associated with a myelomeningocele [22]. The hallmark of the Chiari II malformation is a constricted posterior fossa, wide foramen magnum, and variable caudal displacement of dysplastic brainstem and cerebellar vermis into the upper cervical canal [23]. DTI suggests some patients with the Chiari II malformation have dysplastic supracallosal fibers (Figures 13a and 13b).

Brainstem abnormalities may be identifiable in patients with the Chiari II malformation and appear to be related to the extent of brainstem and cerebellar hypoplasia. More severe cerebellar hypoplasia seems to be associated with hypoplasia of the transverse pontine fibers while the medial lemniscus and corticospinal tracts are preserved (Figures 14a and 14b). The superior and inferior cerebellar peduncles are often underdeveloped.

### Joubert syndrome

Joubert syndrome was initially described as a clinical diagnosis; the “molar tooth sign” is the radiologic hallmark of Joubert syndrome although there is considerable variability in the

hindbrain abnormalities [24]. There are reports of diffusion tensor abnormalities of brainstem tracts in patients with Joubert syndrome. The variability of DTI abnormalities may parallel the severity of the malformation and ranges from normal to absence of the transverse pontine fibers such that the corticospinal tracts and medial lemniscus are juxtaposed (Figures 15a and 15b). By DTI, the fibers of the superior cerebellar peduncles did not decussate in the mesencephalon and the corticospinal tracts do not cross in the caudal medulla

### Conclusion

In conclusion, DTI has numerous potential applications in the pediatric brain both in the normal and disease states. Further technical refinements are needed to improve the spatial resolution of diffusion tensor imaging, in addition to increasing the sensitivity of DTI to crossing fibers without making DTI too time-consuming for clinical use ■

► **DTI has numerous potential applications in the pediatric brain.**

## References

- [1] Basser PJ, Jones DK. *Diffusion-Tensor MRI: Theory, Experimental Design and Data Analysis – A Technical Review*. NMR Biomed. 2002; 15: 456-467.
- [2] Basser PJ, Pajevic S, Pierpaoli C, Duda J, Aldroubi A, et al. *In Vitro Fiber Tractography using DT-MRI data*. Magn Reson Med. 2000; 44: 625-632.
- [3] Jespersen SN, Kroenke CD, Ostergaard L, Ackerman JH, Yablonskiy DA. *Modeling Dendrite Density from Magnetic Resonance Diffusion Measurements*. NeuroImage. 2007; 34(4): 1473-1486.
- [4] Song SK, Yoshino J, Le TQ, Lin S-J, Sun S-W, Armstrong RC. *Demyelination Increases Radial Diffusivity in Corpus Callosum of Mouse Brain*. NeuroImage. 2005; 26(1): 132-140.
- [5] Harsan LA, Poulet P, Guignard B, Steibel J, Parizel N, de Sousa PL, Boehm N, et al. *Brain Demyelination and Recovery Assessment by Noninvasive In Vivo Diffusion Tensor Magnetic Resonance Imaging*. Journal of Neuroscience Research. 2006; 83(2): 392-402.
- [6] DaSilva AFM, Tuch DS, Weigell MR, Hadjikhani N. *A Primer on Diffusion Tensor Imaging of Anatomical Substructures*. Neurosurg Focus. 2003; 15: 1-4.
- [7] Wakana S, Jiang H, Nagae-Poetscher M, van Zijl PCM, Mori S. *Fiber Tracked-based Atlas of Human White Matter Anatomy*. Radiology. 2004; 230: 77-87.
- [8] Mori S, Kaufmann WE, Davatzikos C, Stieltjes B, Armodei L, Fredericksen K, Pearlson GD, et al. *Imaging Cortical Association Tracts in the Human Brain using Diffusion-Tensor-Based Axonal Tracking*. Magn Reson in Med. 2002; 47: 215-223.
- [9] Mukherjee P, Chung SW, Berman JI, Hess CP, Henry RG. *Diffusion Tensor MR Imaging and Fiber Tractography: Technical Considerations*. AJNR Am J Neuroradiol. 2008; 29(5): 843-852.
- [10] Hermoye L, Saint-Martin C, Cosnard G, Lee S-k, Kim J, Nassogne M-C, Menten R, et al. *Pediatric Diffusion Tensor Imaging: Normal Database and Observation of the White Matter Maturation in Early Childhood*. NeuroImage. 2006; 29(2): 493-504.
- [11] Ashtari M, Cervellione KL, Hason KM, Wu J, McIlree C, Kester H, et al. *White Matter Development During Late Adolescence in Healthy Males; a Cross-sectional Diffusion Tensor Study*. NeuroImage. 2007; 35(2): 501-510.
- [12] Giorgio A, Watkins KE, Douaud G, James AC, James S, De Stefano N, et al. *Changes in White Matter Microstructure During Adolescence*. NeuroImage. 2008; 39(1): 52-61.
- [13] Smith SM, Jenkinson M, Johansen-Berg H, Rueckert D, Nichols TE, Mackay CE, et al. *Tract-based Spatial Statistics: Voxelwise Analysis of Multi-subject Diffusion Data*. NeuroImage. 2006; 31(4): 1487-1505.
- [14] Snook L, Plewes C, Beaulieu C. *Voxel Based versus Region of Interest Analysis in Diffusion Tensor Imaging of Neurodevelopment*. NeuroImage. 2007; 34(1): 243-252.
- [15] Filippi CG, Lin DDM, Tsiouris AJ, Watts R, Packard AM, Heier LA, Ulu AM. *Diffusion-Tensor MR Imaging in Children with Developmental Delay: Preliminary Findings*. Radiology. 2003; 229: 44-50.
- [16] Nagy Z, Westerberg H, Skare S, Andersson J, Lilja A, Flodmark O, et al. *Preterm Children have Disturbances of White Matter at 11 Years of Age as Shown by Diffusion Tensor Imaging*. Pediatr Res. 2003; 54: 672-679.
- [17] Wilde E, Chu Z, Bigler ED. *Diffusion Tensor Imaging in the Corpus Callosum in Children after Moderate to Severe Traumatic Brain Injury*. J Neurotrauma. 2006; 23: 1412-1426.
- [18] Hamilton LS, Levitt JG, O'Neill J, Alger JR, Luders E, Phillips OR, et al. *Reduced White Matter Integrity in Attention-deficit Hyperactivity Disorder*. Neuroreport. 2008; 19(17): 1705-1708.
- [19] Helton KJ, Phillips NS, Khan RB, Boop FA, Sanford RA, Zou P, et al. *Diffusion Tensor Imaging of Tract Involvement in Children with Pontine Tumors*. AJNR Am J Neuroradiol. 2006; 27: 786-793.
- [20] Lee SK, Mori S, Kim DJ, Kim SY, Kim SY, Kim DI. *Diffusion Tensor MR Imaging Visualizes the Altered Hemispheric Fiber Connection in Callosal Dysgenesis*. AJNR Am J Neuroradiol. 2004; 25: 25-28.
- [21] Rollins N. *Semilobar Holoprosencephaly as seen with Diffusion Tensor Imaging and Fiber Tracking*. AJNR Am J Neuroradiol. 2005; 26: 2148-2152.
- [22] Rollins N, Reyes T, Chia J. *Diffusion Tensor Imaging in Lissencephaly*. AJNR Am J Neuroradiol. 2005; 26: 1583-1586.
- [23] Vachha B, Adams R, Rollins N. *Depiction of Limbic Tract Anomalies with Diffusion Tensor Imaging and Fiber Tract Reconstruction: Initial Investigation of Associations with Memory and Learning in Children with Myelomeningocele and Chiari II Malformation*. Radiology. 2006; 240: 194-202.
- [24] Poretti A, Boltshauser E, Loenneker T, Valente EM, Brancati F, Il'yasov K, Huisman TA. *Diffusion Tensor Imaging in Joubert Syndrome*. AJNR Am J Neuroradiol. 2007; 28(10): 1929-1933.

# Functional MRI of the sensorimotor system in newborns

**H. Boecker** Department of Radiology, University Hospital Bonn, Bonn, Germany.  
**L. Scheef**

**A. Heep** Department Neonatology, University Hospital Bonn, Bonn, Germany.

Preterm birth before 32 weeks gestational age (GA) is associated with a high incidence of periventricular white matter injury (PWMI). Early prediction of motor deficits associated with PWMI has a fundamental clinical impact on the management of extremely preterm children. Reliable early predictive measures are warranted to allow for prompt and lesion-oriented rehabilitative treatment approaches. Unfortunately, neurological examination in the first months of life is poorly predictive for later cerebral palsy [1-3].

At present, the most predictive measures regarding long-term neurodevelopmental deficits [4-6] and cerebral palsy [6-8] in preterm and term infants are provided by structural imaging techniques. PWMI can be identified during the early postnatal period by means of ultrasound imaging [9] but magnetic resonance imaging (MRI) provides a better differentiation of brain tissue and pathology [10-13]. It is therefore highly sensitive to detecting white matter and gray matter lesions [5].

It has been shown that T1-hyperintensities or cysts located in the corona radiata above the posterior limb of the internal capsule are important predictors for motor prognosis of preterm infants with PWMI [14]. Compared to ultrasound imaging, a general advantage of MRI is that subtentorial lesions can be recognized as well.

Since structural MRI allows only indirect inference upon functional states, we were interested in using functional magnetic resonance imaging (fMRI) as a non-invasive *in vivo* imaging tool for studying the sensorimotor system in the neonatal brain. This is initially described in passive sensorimotor stimulation tasks by Erberich and co-workers [15, 16]. Starting from initial block-design work and extending the initial approach by Erberich and co-workers, this review article describes the workflow of our interdisciplinary work at the University of Bonn.

Our review article is aimed at establishing reliable and safe neonatal fMRI procedures and to correlate the *in vivo* data with subsequent clinical outcome parameters. The main section of the review is focused on our published data [17, 18] of blood oxygenation level dependent (BOLD) responses. The responses are associated with unilateral passive forearm extension/flexion in a group of preterm infants with a median GA of 26.5 weeks (fMRI at term-equivalent age). The last part of the review deals with safety issues and technical developments.

## Methods

### Continuous passive sensorimotor stimulation - blocked design

Eight preterm infants with a median gestational age of 26.5 weeks (range 24-30 weeks) were included in the study, which was approved by the ethical committee of the Medical Faculty of the University of Bonn. One patient had to be excluded from the analysis because of incomplete MRI acquisition and two patients due to major movement artifacts.

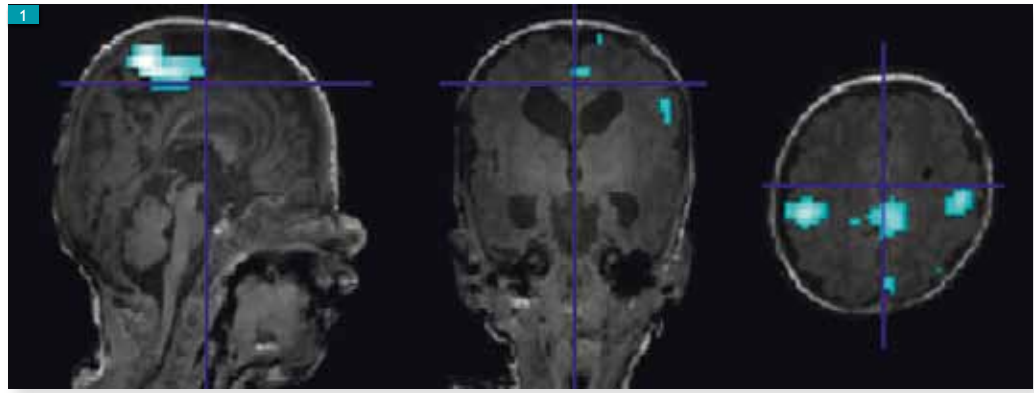
The fMRI was performed at term-equivalent (median 39 weeks post conceptional age (PCA); 38 3/7 - 39 6/7 weeks range). Stable respiratory and circulatory function by continuous monitoring during at least one week before fMRI was a prerequisite for inclusion in the study. Chloral hydrate (50 mg/kg) was administered via a gastric tube for sedation 30 minutes before MRI. During MRI, vital signs (body temperature, heart rate and oxygen saturation) were continuously monitored. Acoustic protection was performed with earplugs, mini muff acoustic shells, and headphones.

The MRI was performed on a 3.0T Achieva system (Philips Healthcare, Best, the Netherlands) using an 8-channel adult SENSE head coil. The clinical protocol consisted of a standard T1-weighted SpinEcho sequence (TR/TE/flip: 580 ms/13 ms/90°, 22 slices,

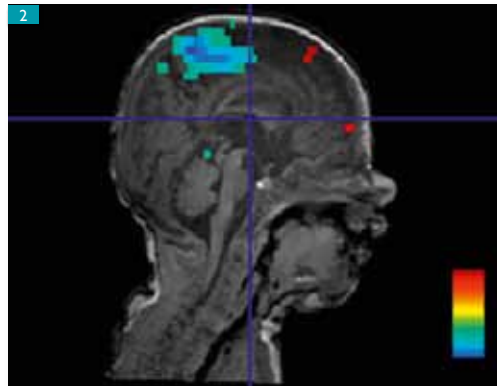
► **fMRI is a non-invasive method for studying the sensorimotor system of the pediatric brain.**

► **Early pre-term birth has a high incidence of periventricular white matter injury.**

▶ Figure 1. Typical example of a neonate showing negative BOLD responses, in the sensorimotor cortex bilaterally, and in the posterior part of the supplementary motor area, to passive unilateral sensorimotor stimulation [16].



▶ Figure 2. Same child as in Figure 1 showing that negative BOLD responses (color-coded in blue; positive BOLD responses color-coded in yellow-red) were the prevailing cortical activation pattern in response to passive unilateral sensorimotor stimulation in preterm neonates [16].



▶ **fMRI of the sensorimotor system can be performed as part of a clinical MRI protocol.**

resolution:  $0.8 \times 1.0 \times 4.0 \text{ mm}^3$ ). A T2-weighted TSE-sequence (TR/TE/flip: 4200 ms/80 ms/90°, 22 slices, reconstruction resolution:  $0.6 \times 0.8 \times 4.0 \text{ mm}^3$ ) and a diffusion weighted sequence (TR/TE/flip: 2858 ms/40 ms/90°, 22 slices, reconstruction resolution:  $2.0 \times 2.0 \times 5.0 \text{ mm}^3$ ; b value: 1000 s/mm<sup>2</sup>).

High resolution T1-weighted data sets (T1-TFE, TR/TE/flip: 9.38 ms/4.32 ms/8°, 120 slices, spatial resolution: slice thickness 0.78 mm in-plane  $0.78 \text{ mm} \times 0.83 \text{ mm}$ ) were obtained for anatomical overlay of the fMRI data (TE/TR/flip: 35 ms/2.60 ms/90°, spatial resolution:  $1.88 \times 1.88 \times 3.50 \text{ mm}^3$ ). Passive sensorimotor stimulation was induced by a physician in the scanning room via manual traction of one forearm at a frequency of ~1 Hz.

The sensorimotor stimulation blocks, each of 20s duration, were repeated five times per stimulation side, alternating with an equal amount of rest (no movement) blocks. The data was analyzed with the SPM5 software (Wellcome Department of Imaging Neuroscience, London, United Kingdom) based on Matlab 7.1 (The Mathworks Inc, Natick, MA) and included spatial realignment, co registration to the individual T1-weighted MRI and spatial smoothing (6-mm isotropic Gaussian kernel). Whole-brain voxel-based statistical analyses were performed between the movement and rest conditions on a single-subject basis.

## Results

The fMRI was well tolerated by all infants and no adverse effects of the sedation were observed under continuous monitoring for vital signs. The manipulation of the hand did not induce disruption of sleep under sedation. SPM5 analyses revealed that passive unilateral sensorimotor stimulation was associated with a consistent bilateral activation pattern involving the sensorimotor cortex in 9/10 trials [17].

An exemplary case showing bilateral sensorimotor cortex activation is given in Figure 1.

As predicted, based on previous studies [14, 15], the prevailing BOLD response was a negative BOLD signal (N= 7/10 datasets), as clearly shown in Figure 2.

## Discussion

Our experience shows that fMRI of the sensorimotor system can be performed as part of a clinical MRI protocol in extremely preterm high-risk infants. The published ten data sets acquired in preterm infants at term-equivalent age [17] indicate a bilateral negative BOLD response in primary sensorimotor cortices as predominant activation pattern. This bilateral activation pattern is compatible with a bilaterally distributed system at this developmental stage.

The negative BOLD activation pattern is compatible with previous fMRI findings in infants born at term [15, 16] and it is thus likely (but as yet unproven) that negative BOLD responses constitute the prototypical hemodynamic response at this stage of brain maturation. However, these findings warrant confirmation in a larger cohort.

Studies relating fMRI patterns in relation to maturation status are important prerequisites for clinical fMRI applications aimed at detecting functional compromises related to brain

pathology. It has to be pointed out, however, that despite the inversion of the BOLD signal in infants, the spatial localization in primary sensor-motor cortex was robustly determined. Therefore, the presented approach, namely studies of cortical responses to passive sensorimotor stimulation, may prove helpful in determining functional impairments at an extremely early age of life.

At present, however, the small number of studied infants does not yet allow making any inference as to later motor status. Neurological examination and neurodevelopmental testing at the age of four to six months did not show a constant pathological pattern, except one child demonstrating a differing positive and unilateral BOLD response. This patient had abnormalities on neurological examination at term-equivalent age (muscular hypertonia, poor movement repertoire) and impaired motor skills in Griffith's mental development scales at four month corrected age; possibly reflecting delayed developmental organization of the sensorimotor system.

This investigation is currently being extended with the focus on the long-term neurodevelopmental follow-up investigations to validate the significance of these findings.

It is important to point out that there are several relevant safety issues that have to be carefully controlled in sedated neonates. Continuous monitoring of vital signs (body temperature, heart rate, and oxygen saturation) is required during the entire MRI procedure. Beyond strict



▲ Figure 3. Experimental setup for event-related passive stimulation of neonates.

compliance to SAR restriction, acoustic noise is another major safety issue and warrants adequate protection (ear prongs, mini muff acoustic shells, head phones) and electrophysiological monitoring with brainstem evoked response audiometry pre- and post-MRI. Experience shows the fMRI procedure is well tolerated when these issues are carefully respected.

### Future outlook

Optimized head coils for neonatal MRI are warranted to gain higher signal-to-noise contrast. For studies of the sensorimotor system, MRI-compatible devices are warranted that allow standardized and reproducible passive sensorimotor stimulation in event-related acquisitions. A mechanical, MR-compatible device (Figure 3) has been developed for passive unilateral hand extension/flexion movements in which each wrist can be stimulated independently with fully controlled speed and velocity of individual movements [19].

### Acknowledgment

We wish to thank Senior Clinical Scientist Dipl. Phys. Jürgen Gieseke from Philips Healthcare for technical advice and support ■

► **In-vivo studies of responses to passive stimulation may aid early detection of functional impairments.**

## References

- [1] Ellenberg JH, Nelson KB. *Early Recognition of Infants at High Risk for Cerebral Palsy: Examination at Age Four Months*. Dev Med Child Neurol. 1981; 23(6): 705-716.
- [2] Palmer FB. *Strategies for the Early Diagnosis of Cerebral Palsy*. J Pediatr. 2004; 145(2 Suppl): S8-S11.
- [3] Nelson KB, Ellenberg JH. *Neonatal Signs as Predictors of Cerebral Palsy*. Pediatrics. 1979; 64(2): 225-232.
- [4] Van Pul C. *Diffusion Tensor Imaging for the Detection of Hypoxic-Ischemic Injury in Newborns*. Doctoral Thesis, Eindhoven 2004.
- [5] Woodward LJ, Anderson PJ, Austin NC, Howard K, Inder TE. *Neonatal MRI to Predict Neurodevelopmental Outcomes in Preterm Infants*. N Engl J Med. 2006; 355(7): 685-694.
- [6] Sie LT, Hart AA, van Hof J, de Groot L, Lems W, Lafeber HN et al. *Predictive Value of Neonatal MRI with Respect to Late MRI Findings and Clinical Outcome. A Study in Infants with Periventricular Densities on Neonatal Ultrasound*. Neuropediatrics. 2005; 36(2): 78-89.
- [7] Constantinou JC, Adamson-Macedo EN, Mirmiran M, Fleisher BE. *Movement, Imaging and Neurobehavioral Assessment as Predictors of Cerebral Palsy in Preterm Infants*. J Perinatol. 2007; 27(4): 225-229.
- [8] Bax M, Tydeman C, Flodmark O. *Clinical and MRI Correlates of Cerebral Palsy: the European Cerebral Palsy Study*. Jama. 2006; 296(13): 1602-1608.

- [9] Roelants-van Rijn AM, Groenendaal F, Beek FJ, Eken P, van Haastert IC, de Vries LS. *Parenchymal Brain Injury in the Preterm Infant: Comparison of Cranial Ultrasound, MRI and Neurodevelopmental Outcome*. *Neuropediatrics*. 2001; 32(2): 80-89.
- [10] Cioni G, Bartalena L, Biagioni E, Boldrini A, Canapicchi R. *Neuroimaging and Functional Outcome of Neonatal Leukomalacia*. *Behav. Brain Res*. 1992; 49(1): 7-19.
- [11] Ment LR, Bada HS, Barnes P, Grant PE, Hirtz D, Papile LA et al. *Practice Parameter: Neuroimaging of the Neonate: Report of the Quality Standards Subcommittee of the American Academy of Neurology and the Practice Committee of the Child Neurology Society*. *Neurology*. 2002; 58(12): 1726-1738.
- [12] Huppi PS, Dubois J. *Diffusion Tensor Imaging of Brain Development*. *Semin Fetal Neonatal Med*. 2006; 11(6): 489-497.
- [13] Counsell SJ, Shen Y, Boardman JP, Larkman DJ, Kapellou O, Ward P et al. *Axial and Radial Diffusivity in Preterm Infants who have Diffuse White Matter Changes on Magnetic Resonance Imaging at Term-Equivalent Age*. *Pediatrics*. 2006; 117(2): 376-386.
- [14] Nanba Y, Matsui K, Aida N, Sato Y, Toyoshima K, Kawataki M et al. *Magnetic Resonance Imaging Regional T1 Abnormalities at Term Accurately Predict Motor Outcome in Preterm Infants*. *Pediatrics*. 2007; 120(1): e10-9.
- [15] Erberich SG, Panigrahy A, Friedlich P, Seri I, Nelson MD, Gilles F. *Somatosensory Lateralization in the Newborn Brain*. *Neuroimage*. 2006 Jan; 29(1): 155-161.
- [16] Erberich SG, Friedlich P, Seri I, Nelson MD, Jr., Bluml S. *Functional MRI in Neonates using Neonatal Head Coil and MR Compatible Incubator*. *Neuroimage*. 2003; 20(2): 683-692.
- [17] Heep A, Scheef L, Jankowski J, Born M, Zimmermann N, Sival D et al. *Functional Magnetic Resonance Imaging of the Sensorimotor System in Preterm Infants*. *Pediatrics* 2009; 123(1): 294-300.
- [18] Boecker H, Scheef L, Jankowski J, Zimmermann N, Born M, Heep A. *Current Stage of fMRI Applications in Newborns and Children During the First Year of Life*. *Röfo*. 2008; 180(8): 707-714.
- [19] Scheef L, Plein M, Jankowski J, Heep A, Boecker H, Holz D. *Development of a MR-Compatible Passive Sensorimotor Stimulation Device for Neonates*. *European Society of Magnetic Resonance in Neuropediatrics, 9<sup>th</sup> Congress, 2007, Tübingen, Germany*.

Fourteen years of Medicamundi archives are now available online. They can be accessed via:

[www.philips.com/medicamundi](http://www.philips.com/medicamundi)

# 7T MRI research in neurology: initial results and future research applications

**A.G. Webb**  
**M.J. Versluis**  
**M.A. van Buchem**  
**H.E. Kan**  
**W. M. Teeuwisse**  
**M.J.P. van Osch**

C.J. Gorter Center for High Field MRI,  
Department of Radiology,  
Leiden University Medical Center,  
Leiden,  
the Netherlands.

The C.J. Gorter Center for High Field Magnetic Resonance Imaging (MRI) at the Leiden University Medical Center was established within the Department of Radiology in late 2007. The aim of the center is the development of new methods and protocols for high field clinical MRI in a variety of patient populations, in parallel with performing studies of correlative disease models in animals. In particular, the Center has recently installed a Philips Achieva 7T whole-body MRI system, one of only two in the Netherlands.

Strong collaborations exist within the Virtual Institute for Seven Tesla Applications (VISTA), a Dutch initiative of researchers from the University Medical Centers in Leiden, Utrecht and Nijmegen, and from the FC Donders Center for Cognitive Neuroimaging in Nijmegen. The 7T system presents major technical challenges to be able to achieve the full advantages of the high magnetic field. This article summarizes progress in neurological applications during the first year of research with the 7T scanner at Leiden.

## Background

The past twenty years have seen a steady increase in the magnetic field strengths used for clinical MRI. If one compares, for example, 7T vs. 3T the major advantages of the high field can be summarized as:

- an increased signal-to-noise (S/N) allowing higher spatial resolution or reduced scanning times
- a significantly increased sensitivity to differences in tissue magnetic susceptibility at the micro/mesoscopic scale, essentially introducing a new contrast mechanism
- an increased spectral resolution for localized MR spectroscopy.



Figure 1a. The Philips Achieva 7T system installed in Leiden in 2007.

The major challenges include:

- far greater signal inhomogeneity within the patient due to the interaction of high frequency (298 MHz) electromagnetic energy with the body
- higher energy deposition, as measured by the specific absorption ratio (SAR), in the patient with the potential of localized “hotspots”
- a greater degree of image artifacts from macroscopic static field ( $B_0$ ) inhomogeneities at tissue/air and tissue/bone boundaries.

In addition, tissue T1 relaxation times are longer at 7T and T2 values decrease, which reduces some of the improvements in S/N from the high field. Currently, there are also many practical issues, for example the lack of radiofrequency (RF) coils in general at 7T and the lack of a body coil in particular.

The Philips 7T Achieva system installed in Leiden, shown in Figure 1a, weighs 32,000 kg and has linear dimensions of 3.7 x 2.4 x 2.6 m (length x width x height). The 5 gauss line would be about 22.5 m from the magnet isocenter. The setup at Leiden, similar to many elsewhere, has about 400 tonnes of steel for passive magnetic shielding that brings the 5 gauss line to about 6 m from magnet isocenter. For neurological

► **7T MRI offers major advantages, but also presents significant technical challenges.**

▶ Figure 1b. Commercial head coil from Nova Medical with an outer quadrature transmit/receive birdcage resonator and an inner splittable 16-element array receiver.



▶ Figure 1c. Electronics box and ODU connector used to interface custom-built RF coils with the Philips system.



▶ Figure 1d. An example of an in-house custom-built surface coil, diameter 10 cm, used for localized brain imaging.



▶ **The very high resolution is used in research into neurodegenerative diseases.**

applications, the system is delivered with a quadrature birdcage transmit coil and a 16 channel receive array, as shown in Figure 1b.

The current gradient configuration has a maximum strength of 33 mT/m with a slew-rate of 166 mT/m/ms. Two radiofrequency (RF) channels are available for proton and carbon experiments, each channel being driven by a 4 kW RF amplifier. Table motion for patients is currently only possible manually, and in the horizontal direction. The Philips system has a very simple hardware interface, illustrated in Figure 1c, which enables the use of custom-built RF coils via a standard type-N connector. One such example, constructed in Leiden, a simple transmit and receive surface coil for localized brain imaging, is shown in Figure 1d.

Based upon the advantages of high field outlined above, our current approach to developing protocols of clinical neurological relevance concentrates on three specific areas:

- high-resolution MR angiography and diffusion tensor imaging

- susceptibility and phase imaging with quantitative assessment of the distribution of the magnetic susceptibility
- localized proton MR spectroscopy.

### High-resolution magnetic resonance angiography and diffusion tensor imaging

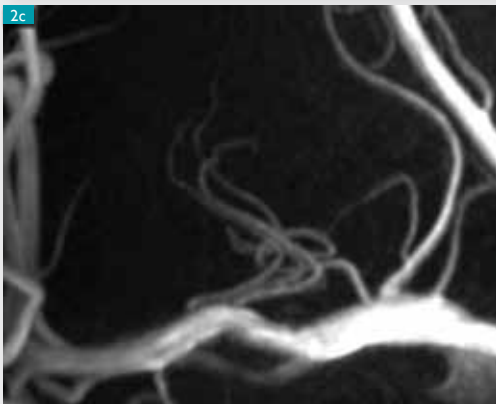
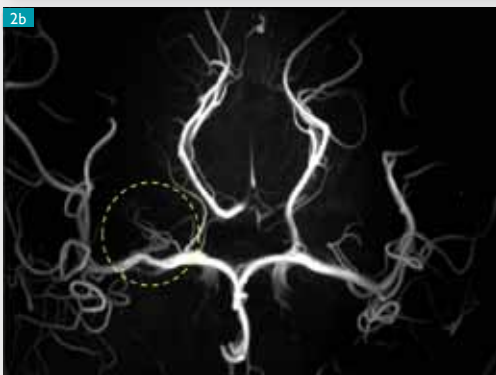
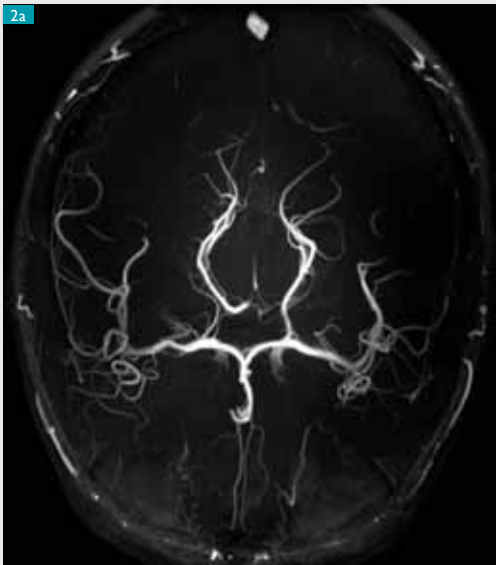
Enhanced spatial resolution is of most benefit when the dimensions of the structures of interest are very similar to that of the improved resolution. One example of direct clinical significance is high-resolution magnetic resonance angiography (MRA). Current clinical protocols at 3T typically acquire three-dimensional time-of-flight (TOF) angiograms at a spatial resolution of 1 x 1 x 1 mm and, therefore, much of the fine branching structure, which may be disrupted in vascular disease, is not visible.

At 7T, in addition to the increased spatial resolution, background tissue suppression is improved compared to 3T because of the higher tissue T1 value. The relatively low flip angles in 3D TOF sequences mean that SAR is not a major issue. The use of TOF MRA at 7T was first analyzed by the group in Utrecht [1].

Figure 2 shows a series of 3D TOF angiograms acquired at a spatial resolution of 0.23 x 0.23 x 0.23 mm. The data acquisition protocol is based on one developed recently specifically for high field [2], but the use of parallel imaging and sequence optimization allowed us to improve the spatial resolution by approximately 50% in the slice-select dimension. The very high spatial resolution gives clear visualization of the lenticulostriatal arteries, and the branching points from the major feeding artery.

This high-resolution MRA protocol is now part of ongoing clinical research at the LUMC into a number of neurodegenerative diseases that have components of small vessel disease such as cerebral autosomal dominant arteriopathy with subcortical infarcts and leukoencephalopathy (CADASIL).

The second area in which the higher spatial resolution at 7T will be clinically relevant is diffusion tensor imaging (DTI) in which the size of the white matter fiber tracts is much smaller than the imaging voxels. The most important potential confounding factors in DTI at high field is the increased macroscopic susceptibility effect. Eddy current compensation is particularly important, and significant improvements were seen with Philips' recent "blue-ball" method.

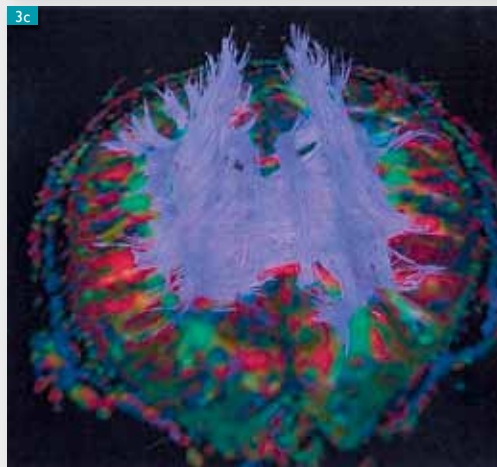
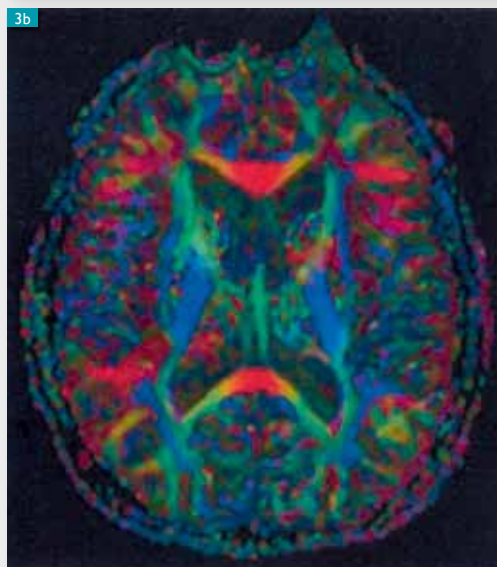
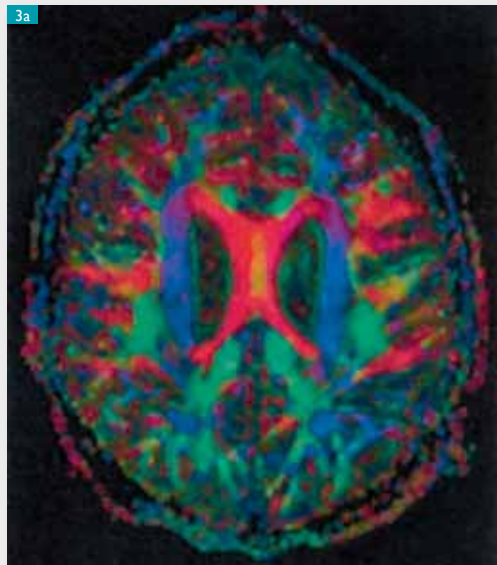


▲  
Figure 2. 3D TOF angiograms from a volunteer acquired using the 16-channel head coil with  $0.23 \text{ mm}^3$  isotropic voxels acquired in 10 minutes.

Figure 2a. Overview of the transverse maximum intensity projection (MIP).

Figure 2b. Selected slab, thickness 5 cm, through the circle of Willis.

Figure 2c. Expansion of the circled area in Figure 2b showing the lenticulostriatal arteries that branch off from a main artery and enter the basal ganglion.



▲  
Figure 3. Results from DTI of a volunteer acquired at a spatial resolution of  $1.5 \times 1.5 \times 1.5 \text{ mm}$  in ten minutes.

Figure 3a. and Figure 3b. Show two fractional anisotropy maps at different levels in the brain.

Figure 3c. Shows a fiber tract map through the corpus callosum.

Although some distortions can be seen in areas close to air/tissue and bone/tissue interfaces, the overall fractional anisotropy (FA) maps are very similar to those acquired at 3T, but at significantly higher resolution (1.5 x 1.5 x 1.5 mm) compared to the standard imaging protocol (-2.1 x 2.1 x 2.1 mm) at 3T. An example is shown in Figure 3.

### Susceptibility and phase imaging

Early work at 7T [3] showed that high field imaging was particularly sensitive to the very small differences in the magnetic susceptibility of different tissues in the brain. Furthermore, it was shown by Duyn et al. [4] that even greater tissue contrast could be generated by using the phase image rather than the standard magnitude image. An example from the 7T at Leiden is shown in Figure 4, in which fine structures within the gray matter can be visualized in the phase image, but not in the magnitude image.

The direct relevance of this type of “susceptibility-weighted” imaging is to diseases such as Alzheimer’s disease and multiple sclerosis, in which the detection of small plaques could potentially form the basis of neuroradiological diagnosis. In Alzheimer’s disease, many of these plaques are visualized as dark spots in the magnitude image, indicating the presence of iron or other metals within the plaque.

However, some plaques are virtually invisible on magnitude images but can be seen on the phase images, suggesting the absence of metal deposition, but such observations are still somewhat controversial. Quantification of susceptibility is therefore an important goal, and our approach at 7T has followed that of Jensen et al. at 3T [5] in calculating magnetic field correlation (MFC) maps using asymmetric spin echo (ASE) sequences.

These MFC maps represent measures of the spatial heterogeneity in the magnetic field susceptibility, with high values of the MFC having been shown to correspond to areas of the brain with high iron concentration. Since the MFC scales as the square of the magnetic field strength, measurement at 7T is much more sensitive than at 3T. Figure 5 shows an example of an MFC map obtained at 7T from a volunteer.

Currently, clinical studies are being performed on patients with Alzheimer’s and Huntington’s disease to quantify the deposition of iron in plaques in the former case, and the altered biodistribution of iron in different parts of the basal ganglia in the latter.

### Localized proton spectroscopy

The range of metabolite resonance frequencies increases linearly with field strength and therefore, provided that the linewidths of the individual resonances are not broadened significantly at the higher field, the spectral resolution also increases linearly with field strength. Since metabolite T1 values and T2 values are not highly field dependent, one also expects a significant increase in S/N. This can be used to acquire spectra from smaller voxels, to improve spectral quantitation via increased S/N, or to reduce the data acquisition time, or a combination of all three.

The two most commonly used localized spectroscopy sequences are stimulated echo acquisition mode (STEAM) and point resolved spectroscopy (PRESS). Although PRESS has a theoretical factor of two higher S/N than STEAM, PRESS requires a much longer echo time and suffers from a higher chemical shift artifact than STEAM and so our current protocols use the STEAM sequence.

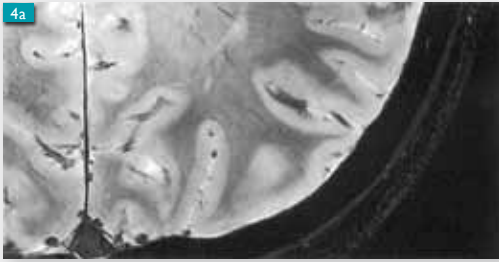
Ongoing studies include Huntington’s disease and familial hemiplegic migraine. Figure 6a shows a spectrum acquired from the frontal lobe of a healthy volunteer. In addition to the resonances from creatine, choline and N-acetylaspartate (NAA), which are observable at 3T (albeit at much lower S/N), metabolites such as GABA can be detected at 7T. This is due to the increased spectral resolution, as they are not observed at 3T. Figure 6b shows a spectrum from the migraine study, in which the high spectral quality allows the concentrations of several coupled and singlet resonances to be quantified using commercial software such as the LC-model.

The improved spectral resolution can also be used to address basic research questions. In collaboration with Dr. Itamar Ronen at Boston University, we are investigating the diffusion properties of NAA and NAAG to determine the ability to quantitate NAA diffusion at lower field strengths. At 1.5T and 3T, the spectral resolution is not sufficient to separate the NAA and NAAG peaks, and so the measured diffusion coefficient is a weighted average of the two metabolites.

At 7T the resonances from NAA and NAAG can be at least partially resolved, as shown in Figure 6, and therefore separate diffusion coefficients can be measured. Preliminary results suggest that the diffusion coefficient of NAA is approximately 30% lower than that of NAAG.

► **Detection of small plaques could aid neuroradiological diagnosis.**

► **Clinical studies are being performed in Alzheimer’s and Huntington’s disease.**

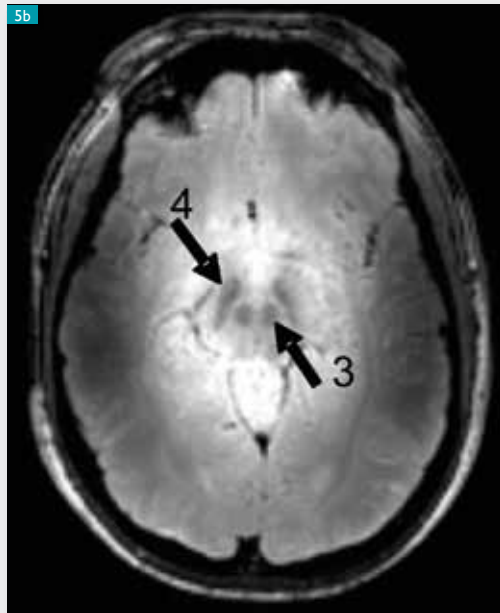
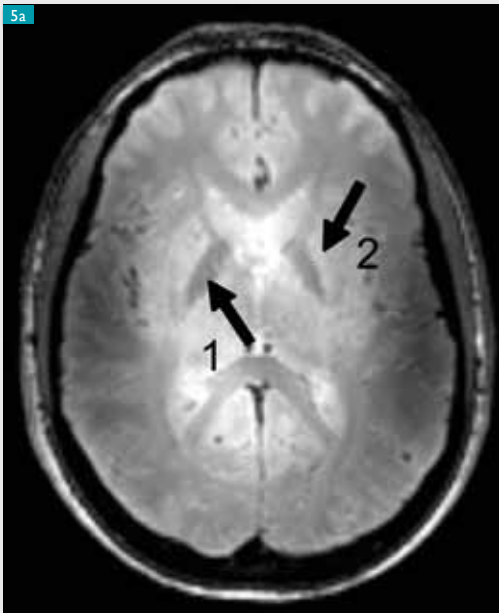


▲ Figure 4a. Image in magnitude mode. Fine details within the white matter can be seen due to small differences in magnetic susceptibility. The image is from a heavily T2\*-weighted gradient echo sequence with a TE of 30 ms.



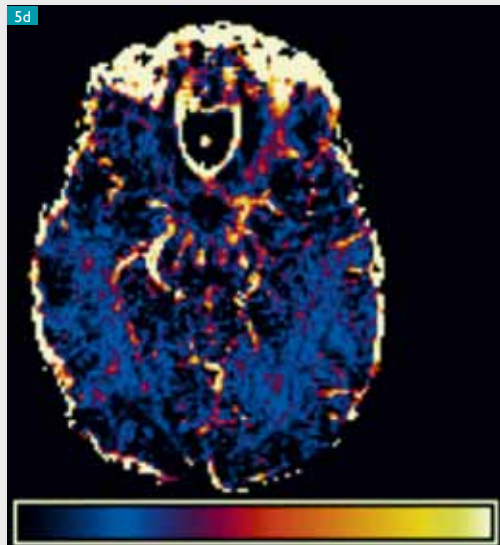
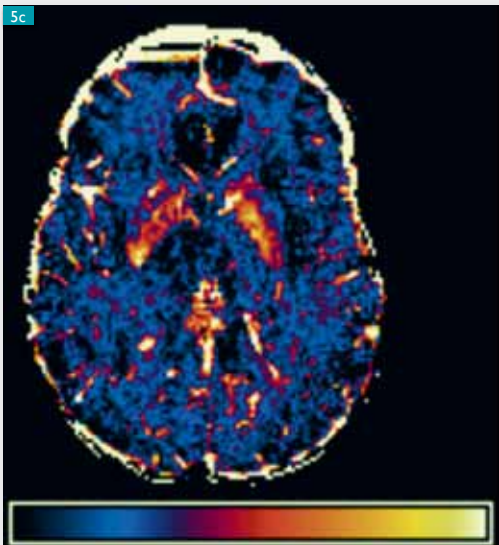
▲ Figure 4b. The corresponding phase image shows even more information than the magnitude image, including substructures within the gray matter.

Figure 4. Enlargement of the temporal lobe of a volunteer.



▲ Figures 5a, b. Two slices from ASE sequence showing the following areas: (arrow 1) globus pallidus, (arrow 2) putamen, (arrow 3) red nuclei, (arrow 4) substantia nigra.

Figure 5. Calculation of an MFC map from 7T images obtained from a volunteer.



▲ Figures 5c, d. Calculated MFC maps from the corresponding areas. A high value of the MFC is seen in all four areas. Total acquisition time for all the ASE images was eight minutes.

Figure 6. Comparison of spectra acquired from the frontal lobe of a healthy volunteer and a patient with familial hemiplegic migraine.

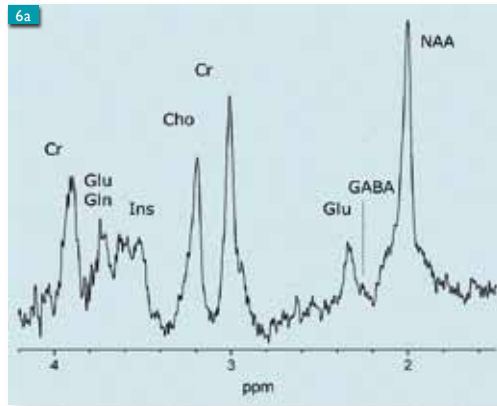


Figure 6a. Spectrum acquired from the frontal lobe of a volunteer, showing a small peak from GABA. The spectrum was acquired with a STEAM sequence (TR/TE/TM = 2000/19/25 ms, BW 4kHz, 2048 data points and 128 averages).

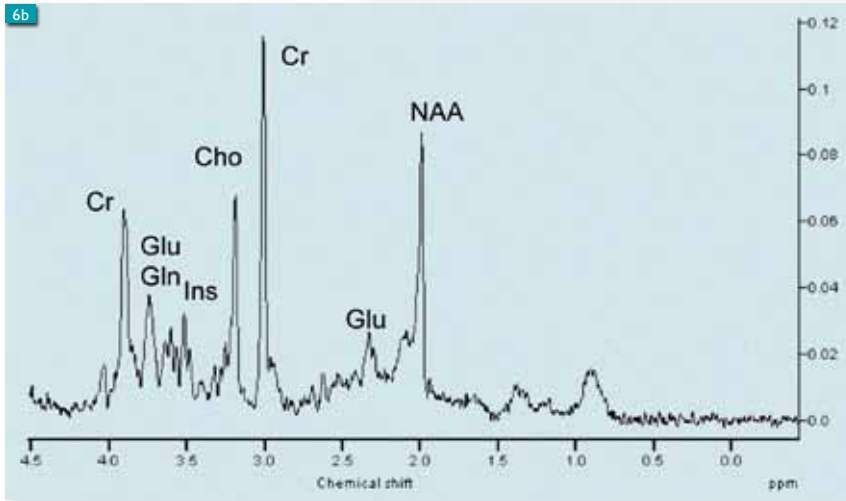


Figure 6b. Localized proton spectrum acquired from the cerebellum of a patient with migraine using identical parameters to those in 6a.

► **Using the magnet bore as a waveguide could be an alternative to complicated transmit arrays for body coils.**

### New radiofrequency technology for 7T and above

The design of RF coils for high magnetic fields is particularly challenging due to the strong interaction between the electromagnetic energy and the patient: the dimensions of the body at 298 MHz are a substantial fraction of a wavelength and so both constructive and destructive interference can occur within the patient.

Although conventional RF coil designs can be adapted for very high magnetic fields, there are some intriguing possibilities of designing new types of coils specifically for high field. For example, the idea of using the magnet bore itself as a waveguide for energy from an antenna placed well away from the patient has recently been suggested as a promising method for obtaining large field-of-view images [6].

Figure 7a shows a setup at Leiden in which a 35 cm square patch antenna positioned just outside the bore of the magnet. Figure 7b shows that the field-of-view excited by the travelling wave from the antenna is very large, typically greater than the linear region of the gradients. Figure 7c shows results obtained by transmitting with the antenna and receiving using the local surface coil shown in Figure 1d.

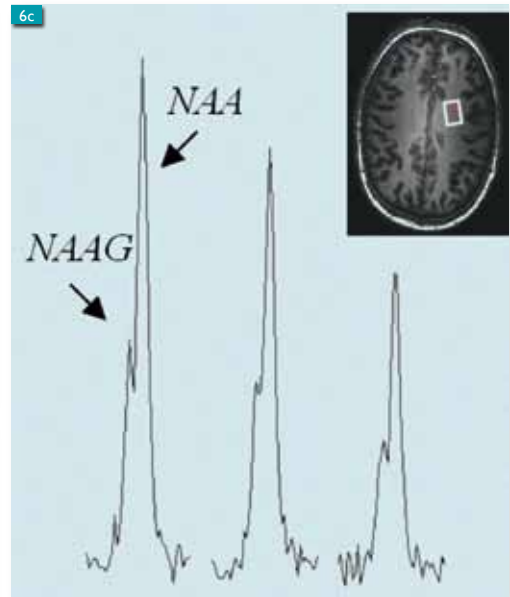


Figure 6c. NAA and NAAG signals with increasing diffusion weighting ( $b=0, 591$  and  $1461$  s/mm<sup>2</sup>). Sixty-four signal averages were used. Spectra are the average of three diffusion directions to produce the trace diffusion coefficient.

Although the images obtained are not yet of clinical quality, these new approaches show considerable promise for the future, since they may form alternatives to complicated transmit arrays for a “body coil” at high fields.

### Patient acceptance of 7T

Aside from protocol and technique development, it is also important that 7T MRI be compatible with patient studies in terms of patient acceptance of the entire procedure. The results of a survey of volunteers and patients who have undergone a 7T scan are shown in Figure 8. The time duration of a scan is currently limited to one hour by the Ethics Committee at the Leiden University Medical Center.

The majority of these studies have been neurological, but the development of in-house RF coils has enabled a number of cardiac and musculoskeletal studies to be performed. The results of the survey show that the most common effect is dizziness when entering the magnet, suggesting that very slow table motion should be used. Overall, there is very little difference among the experiences of volunteers and patients between having 3T and 7T scans.

### Future clinical directions

As of 2009, 7T human MRI research is a field dominated academically by technical innovations in RF design, sequence optimization for both

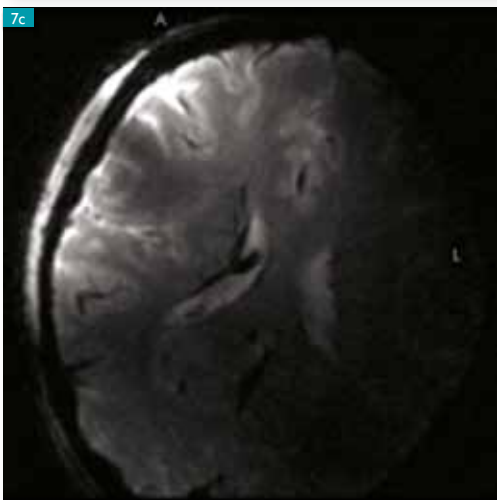


Figure 7. Experimental set up with a square patch antenna.

Figure 7a. Photograph of a patch antenna, resonant at 298 MHz, which is connected to the Philips Achieva 7T interface box. The patient lies in the center of the magnet with the head approximately 60 cm away from the antenna. The bore of the magnet acts as a waveguide, which allows a travelling wave to pass down the bore.

Figure 7b. Large field-of-view image from a volunteer acquired with the patch antenna. The field-of-view in the head-foot direction is about 55 cm, and is limited only in software by the linear region of the gradients.

Figure 7c. One slice from a data set using the antenna to transmit the signal, and a local surface coil placed at the top left of the image to receive it.



improved image contrast and controlled patient safety, and fundamental research areas such as functional imaging. However, at many sites throughout the world a significant number of patient studies in the areas of neurology, cardiology and musculoskeletal imaging are

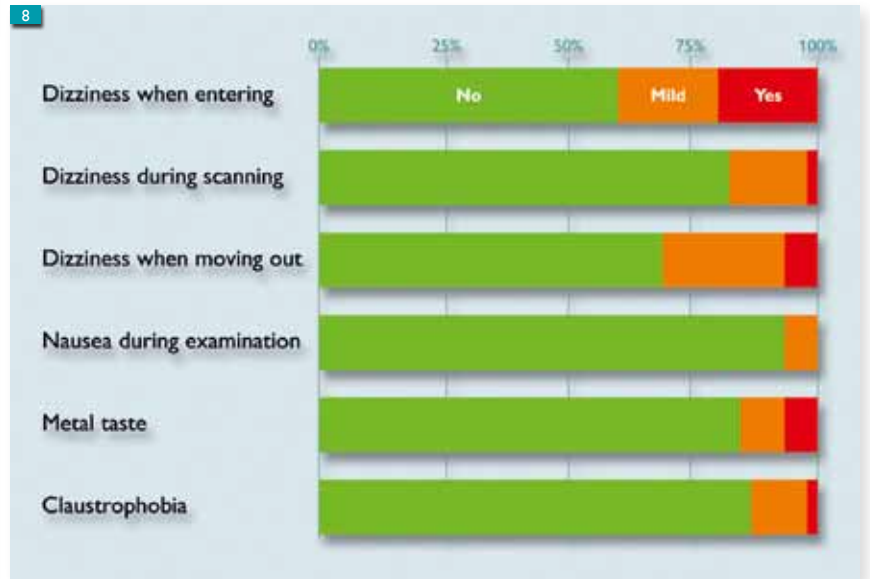


Figure 8. Summary of a survey of 55 volunteers and patients who underwent a 7T scan.

now beginning. The use of 7T MRI is clearly not anticipated to replace that of 3T for general clinical diagnosis, but to supplement it for specific, well-defined types of scans.

Twenty years of intensive commercial and academic developments meant that the transition from 1.5T to 3T was essentially entirely comprehensive in terms of increased image quality. In large part, this was because no fundamental changes in hardware beyond those for 1.5T were needed. The situation is completely different when comparing 3T with 7T MRI. Patient dimensions are now a substantial fraction of the wavelength of the RF irradiation and, particularly for body imaging; this requires a fundamental redesign of data acquisition and hardware.

In our view, it is important to define specific types of examinations that will benefit from the higher magnetic field. For example, standard imaging protocols such as T1, T2 and proton density weighting can all be run with excellent results at 7T, but essentially produce images with no greater diagnostic value (and often considerably lower value) than those at 3T.

► **7T requires a fundamental redesign of data acquisition and hardware.**

► **The clinical potential for heteronuclear imaging and spectroscopy will be investigated.**

Although higher spatial resolution is often touted as a reason for moving to higher fields, the S/N increases approximately in proportion to the field strength [7]. That means that the best that can be achieved under ideal conditions is an isotropic increase in resolution by a factor of about 30% in each dimension or, alternatively, a reduction in slice thickness by a factor of between two and two-and-a-half.

weighted scanning and/or localized proton spectroscopy. In the future, we plan to investigate the clinical potential for heteronuclear imaging and spectroscopy, a general area in which 3T simply does not have the sensitivity. Potential targets include  $^{13}\text{C}$  spectroscopy for studying metabolism in Alzheimer patients,  $^{23}\text{Na}$  for studies of migraine, and  $^{31}\text{P}$  for Huntington's disease ■

Our research approach is therefore is to use 3T scanning for standard morphological imaging, and the 7T for supplemental scans including high-resolution angiography, susceptibility-

## References

- [1] Zwanenburg JJ, Hendrikse J, Takahara T, Visser F, Luijten PR. *MR Angiography of the Cerebral Perforating Arteries with Magnetization Prepared Anatomical Reference at 7T: Comparison with Time-of-Flight*. J Magn Reson Imaging. 2008; 28(6): 1519-1526
- [2] Kang CK, Park CW, Han JY, Kim SH, Park CA, Kim KN et al. *Imaging and Analysis of Lenticulostriate Arteries using 7.0-Tesla Magnetic Resonance Angiography*. Magn Reson Med. 2009; 61(1): 136-144.
- [3] Li TQ, van Gelderen P, Merkle H, Talagala L, Koretsky AP, Duyn J. *Extensive Heterogeneity in White Matter Intensity in High-Resolution T2\*-Weighted MRI of the Human Brain at 7.0 T*. Neuroimage. 2006; 32(3): 1032-1040.
- [4] Duyn JH, van Gelderen P, Li TQ, de Zwart JA, Koretsky AP, Fukunaga M. *High-Field MRI of Brain Cortical Substructure Based on Signal Phase*. Proc Natl Acad Sci USA. 2007; 104(28): 11796-11801.
- [5] Jensen JH, Szulc K, Hu C, Ramani A, Lu H, Xuan L et al. *Magnetic Field Correlation as a Measure of Iron-Generated Magnetic Field Inhomogeneities in the Brain*. Magn Reson Med. 2009; 61(2): 481-485.
- [6] Brunner DO, De Zanche N, Paska J, Froehlich J, Pruessmann KP. *Traveling Wave MR on a Whole-Body System*. Int Soc Magn Reson Med; Toronto 2008.
- [7] Vaughan JT, Garwood M, Collins CM, Liu W, DelaBarre L, Adriany G et al. *7T vs. 4T: RF Power, Homogeneity, and Signal-to-Noise Comparison in Head Images*. Magn Reson Med. 2001; 46(1): 24-30.

# Dynamic whole-spine MRI of contortionists

**W.W. Orrison, Jr**  
**T.G. Perkins**

Touro University College of Osteopathic Medicine, Henderson, NV, USA.  
Amigenics Inc., Las Vegas, NV, USA.  
Spring Valley Nevada Imaging Center, Las Vegas, NV, USA.

Many athletic activities involve extreme spinal stress, but few involve such extreme forms of spinal mobility as that of circus contortionists. In this study, five female contortionists from a Mongolian circus school, between 20 and 49 years of age, were examined using a 3T cylindrical MR imaging system (Philips Achieva) to assess pathological changes that might be associated with the contortionists' act, in which the body is twisted into extreme positions.

Additional whole-spine dynamic images were obtained in two of contortionists using the Philips Panorama High Field Open (HFO) 1T open MR system (Figure 1) in order to define the range of motion achieved during extreme contortion.

## Materials and methods

Whole-spine MR images were obtained in all five of the participants on a Philips Achieva 3.0T system, with participants in a supine position.

Sagittal whole-spine images were acquired using a T2-weighted TSE sequence with TF 36, 270 mm FOV, 5 mm slice thickness, 234 x 304 imaging matrix, and TR/TE 3901/120.

Coronal whole-spine images were acquired with a similar sequence, with TR/TE 4682/120.

The images were acquired with three linked image stacks, and fused into a single image using the MR imaging system's software (Philips MobiView).

Transverse cervical spine images were acquired using a balanced FFE sequence with 210 mm FOV, 4.0 mm slice thickness, 280 x 224 matrix, and TR/TE 4.6/2.3. Transverse lumbar and thoracic spine images were obtained using a T2-weighted TSE sequence with TF 16, 220 mm FOV, 6 mm slice thickness, 202 x 256 matrix, and TR/ TE 2485/110.

In two of the five participants, whole-spine dynamic imaging was performed using the Philips



Panorama HFO system with the participant in a series of extreme contorted positions.

▲ Figure 1. The Philips Panorama HFO 1T open MR system.

The Panorama HFO has a unique, integrated quadrature body coil, and provides access to a variety of patients who would otherwise be difficult or impossible to image with MRI. This not only includes patients with claustrophobia, but also patients who are unable to enter other MRI systems due to size, body habitus, or a requirement for unusual positioning such as the extreme examples of contortionists presented in this article.

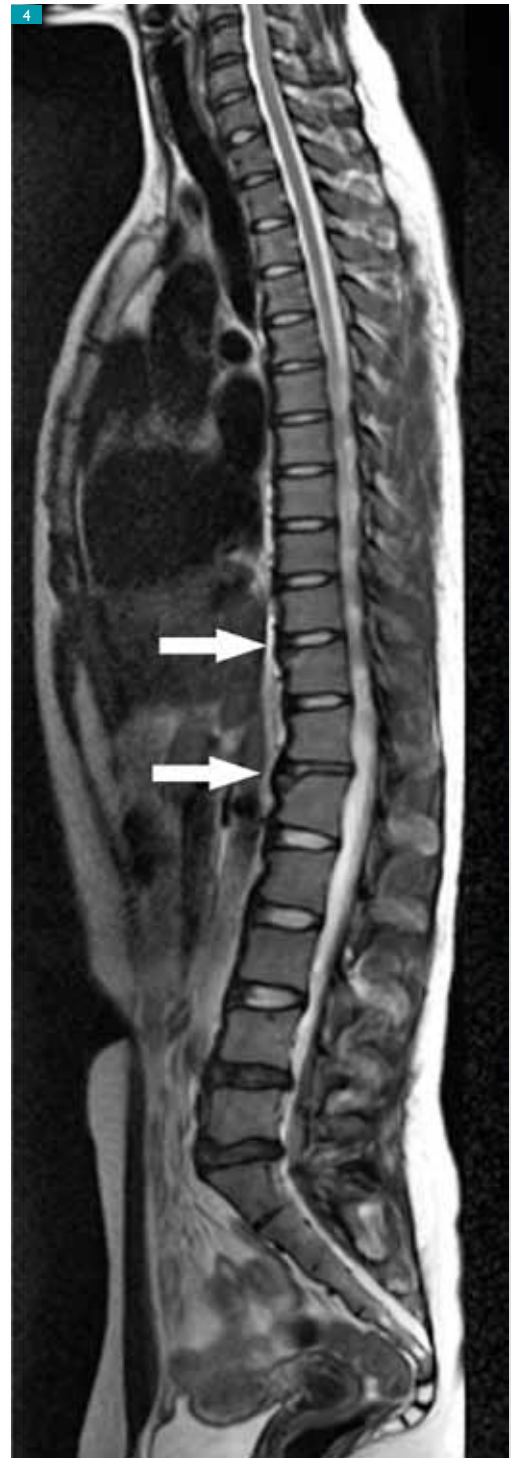
The Panorama HFO's open access and wide, movable patient table made it possible to accommodate the contortionists during imaging in both the flexion and extension positions. The study would have been impossible to perform in a conventional cylindrical scanner.

► **Whole-spine dynamic images were obtained in two contortionists.**

▶ Figure 2. 3.0T sagittal T2-TSE image showing lack of normal cervical and lumbar curvature.

▶ Figure 3. 3.0T coronal T2-TSE image showing mild dextroscoliosis.

▶▶ Figure 4. 3.0T sagittal 3.0T T2-TSE image showing anterior limbus fractures at T11 and L1 (arrows).



### Whole-spine dynamic imaging

In this study, whole-spine MRI was very valuable in evaluating the spinal anatomy and pathological conditions of the participants. The dynamic real-time imaging during active contortion in the Panorama HFO provided a unique opportunity to demonstrate the severe stressors imposed by extreme extension of the spine. Advantages offered by the Panorama HFO's wide-open patient space include the ability to examine the entire spine in full motion through flexion and extension, improved resolution, and direct visualization of the spinal cord, intervertebral discs, and paraspinous soft tissues.

In the future, this method may also be used in other applications involving limited spinal motion and vertebral, disc or spinal cord displacement, such as pain management and traumatic spine injuries.

### Image interpretation

Image interpretation was performed with evaluation of specific anatomical observations:

- scoliosis
- straightening of normal cervical lordosis
- degenerative intervertebral discs
- annular tears
- disc bulges

- osteophytes
- anterosuperior limbus vertebrae fractures, defined as separation of the rim of the annular apophysis.

### Data analysis

Vertebral body angles were determined using a commercial DICOM viewing and analysis program (Philips DICOM Viewer, Philips Healthcare). The precision of the angle measurements was limited by the digital resolution of the images and the analysis program, resulting

▶ **The entire spine could be examined in full motion through flexion and extension.**



◀◀

Figure 5. Patient in the full extension position within the aperture of the Panorama HFO.



◀

Figure 6. Sagittal image from a high-speed dynamic series obtained with the Panorama HFO demonstrating full spinal extension. Images acquired using FFE, 400 mm FOV, 12 mm slice thickness, 128 x 256 matrix and TR/TE 7.3/3.7 with a 45° flip angle and a scan time of 0.96 sec per slice.

in an estimated precision of  $\pm 2.5^\circ$  per vertebral body. Vertebral scoliosis angles were determined utilizing the Cobb angle method. Reformatting of images was performed using OsiriX.

## Results

While the contortionists are comfortable in flexion positions (bending forward), they cannot maintain the extension positions (bending backward) for more than a few minutes.

Abnormalities that were found include anterior limbus fractures, in which a tiny segment of bone separates from the edge of the vertebral ring. The images showed that all five participants in this study had extremely straight spines in the sagittal plane, without the normal cervical and lumbar curvature (Figure 2). This could be of genetic origin, or could be the result of training from a very young age. In addition, all participants had a mild dextroscoliosis, presumably due to their training (Figure 3). Three of the five participants had anterosuperior limbus fractures at T-11 and the upper lumbar levels (Figure 4).

The 3T high-field MR images provided excellent detail of pathological changes including intervertebral disc degeneration. In the two participants who underwent dynamic whole-spine imaging using the Philips Panorama HFO system the regions of pathology corresponded to the areas of maximum angulation identified during extreme extension.

As might be expected, the most severe degenerative changes and complaints of back pain were associated with the older participants.

A total of three posterior cervical intervertebral disc bulges were identified in two of the contortionists, and lumbar disc bulges in three of the participants.

Thoracic anterior osteophyte formation was noted in two participants and lumbar anterior osteophyte formation with disc degeneration in two others.

A total of four anterosuperior limbus fractures were identified in three of the five participants: two limbus fractures (T-11 and L-1) in a 23-year-old individual (Figure 4), one limbus fracture (L-3) in a 22-year-old individual, and one limbus fracture (L5) in a 25-year-old individual.

## Spinal range of motion

The spinal Range of Motion (ROM) was measured in the Panorama HFO system, which allowed the participants unrestricted freedom of movement from full extension to full flexion (Figures 5, 6). The ROM was remarkable, with a range of  $238^\circ$  from full extension ( $-188^\circ$ ) to full flexion ( $+50^\circ$ ). Total vertebral extension was measured from the third cervical level (C-3) to the fifth lumbar level (L-5). The levels of greatest angulation were at the midcervical, thoracolumbar, and lower lumbar spine. The hip joints made the primary contribution to overall flexion, while extension positions involved greater segmental vertebral motion and contributed substantially to the entire ROM.

## Discussion

To the best of our knowledge, this is the first medical imaging study to evaluate a group of contortionists and to report pathological findings associated with this activity. The most significant pathological findings, in our view, were the anterior limbus fractures.

A limbus fracture is a traumatic separation of a segment of bone from the endplate at the edge of the vertebral ring at the site of the attachment of the intervertebral disc. The fracture arises when the disc material herniates between the uncalcified peripheral ring apophysis of the endplates and the central cartilage. Because calcification and fusion of these elements generally occurs between 18 and 25 years of age, limbus fractures are most commonly encountered in adolescents and young adults.

► **The spinal range of motion was a remarkable  $238^\circ$  from full extension to full flexion.**

Much of the literature is concerned with posterior fractures [1], in which the protruding disc may compress neural tissues, but in the study reported here, all the fractures observed were of the anterior limbus.

Various classifications have been proposed. Epstein's [2] is the most comprehensive and, although it applies principally to posterior fractures, it does indicate the range of appearances of vertebral rim fractures. Type I fractures are simple avulsions of the cortex of the end plate, so thin that no obvious defect is present in the vertebral body although an arcuate fracture fragment is visible. Type II fractures are similar in position but include medullary bone and there is a defect in the vertebral body. Type III fractures are small and lateral. Type IV fractures run the full height of the vertebral body and extend to both vertebral endplates. All the fractures detected in our study would be classified as Type II.

The mechanism of limbus fractures is uncertain. They may result from a back injury, but in many cases, there is no trauma but a history of shearing and stress. The anterior limbus fractures encountered in these contortionists are likely related to hyperextension. One possibility is that when these contortionists hyperextend, the limbus fractures. There appears to be very little stress on the spinal column during flexion, with most of the flexion occurring at the hips (more than 180°) and with the contortionists able to hyperflex for long periods comfortably.

However, they can only maintain hyperextension for a few minutes and experience back pain when holding the hyperextended positions for a longer period. Thus, it appears that the major stress on the spine occurs during hyperextension in these remarkable individuals. Since this study, the troupe has altered its training regimen and other exercises to minimize these types of injuries.

The participants with limbus fractures described the initial onset of back pain as an episode of pain occurring during contortion activities. The onset and duration of the back pain, often lasting up to six months, may coincide with the vertebral pathology identified by MR imaging

but this cannot be confirmed because lumbar spine MR imaging studies predating the onset of symptoms were not available.

We hypothesize that the anterior limbus fractures represent traumatic avulsion fractures of the anterosuperior vertebral endplates related to extreme extension. This hypothesis, however, is based on a small sample size, given the limited number of practicing contortionists. Future research on a larger group of contortionists and investigations of their acute spinal injuries would help to confirm our assertion.

## Conclusion

The dynamic images show the unusual degree of angulation of the spine during extreme extension and the remarkable increase in width of the anterior intervertebral disc space in this position as compared with the width in the flexion position. The availability of whole-spine dynamic MR imaging allows for diagnoses of conditions such as generalized or localized limitations in motion; abnormal vertebral, intervertebral disc, or spinal cord displacement; and as demonstrated here, unusual degrees of spinal mobility.

While this study was focused on a unique class of athletes, we believe the methods presented here can be applied to any patient experiencing a pathological condition of the spine that is not localized to one specific spinal region. Future research may open the use of whole-spine dynamic MR imaging into areas such as pain management and traumatic spinal injuries.

## Acknowledgments

This article is based on a study carried out in cooperation with Randal R. Peoples, Janette W. Powell, Eric H. Hanson, Travis H. Snyder and Timothy L. Mueller, published in the *Journal of Neurosurgery: Spine* [3]. The author gratefully acknowledges the technical expertise provided by technicians Jon B. Gibson, Wendy Hopkins and Evelyn Robertson, and the contortion coach Angelique J. Talvat. The study was supported in part by a grant from Philips Healthcare ■

► **The anterior limbus fractures are likely related to hyperextension.**

► **These methods could be applied to any spinal pathology that is not limited to one specific region.**

## References

- [1] Beggs I, Addison J. *Posterior Vertebral Rim Fractures*. *BJR*. 1998; 71: 567-572.
- [2] Epstein NE. *Lumbar Surgery for 56 Limbus Fractures*. *Spine*. 1992; 17(12): 1489-1496.
- [3] Peoples RR, Perkins TG, Powell JW, Hanson EH, Snyder TH, Mueller TL, Orrison WW. *Whole-Spine Dynamic Magnetic Resonance Study of Contortionists: Anatomy and Pathology*. *J Neurosurg Spine*. 2008; 8: 501-509.

# Molecular imaging in dementia: journey to the end of the night

**V. L. Villemagne** Centre for PET, Austin Hospital, Heidelberg, Victoria, Australia.  
The Mental Health Research Institute of Victoria, Parkville, Victoria, Australia.

**G. J. O'Keefe** Centre for PET, Austin Hospital, Heidelberg, Victoria, Australia.

Dementia is characterized by a progressive loss of mental function altering the normal activities of daily living, affecting principally memory and executive functions as well as leading to personality changes. The progressive nature of neurodegeneration suggests an age-dependent process that ultimately leads to synaptic failure and neuronal damage in cortical areas of the brain essential for memory and higher mental functions [1]. In the absence of specific biological markers, direct pathologic examination of brain tissue remains as the only definitive method for establishing a diagnosis [2, 3].

Currently, the clinical diagnosis of dementia is based on progressive impairment of memory, decline in at least one other cognitive domain, changes in personality, and the exclusion of other diseases [4]. A period of up to five years of prodromal decline in cognition, known as Mild Cognitive Impairment (MCI), usually precedes the formal diagnosis of dementia [5, 6]. About 40–60% of carefully characterized subjects with MCI will subsequently progress to meet criteria for Alzheimer's disease (AD) over a three to four year period [7].

Alzheimer's disease represents about 60% of the cases of dementia in the elderly. AD is an irreversible, progressive neurodegenerative disorder clinically characterized by memory loss, cognitive and functional decline [8]. It leads invariably to death, usually within seven to ten years after diagnosis. AD not only has devastating effects on the sufferers and their caregivers, but it also has a tremendous socioeconomic impact on families and the health system, a burden that will only increase in the upcoming years [9, 10].

While AD is the most common cause of dementia in the elderly, post mortem studies have found dementia with Lewy bodies (DLB) to account for 20% of cases [11]. Although the pathological hallmark of DLB is the finding of cortical Lewy bodies, the majority of cases also show extensive cortical amyloid deposition [11]. Parkinson's disease (PD) is one of the most common neurological disorders, affecting approximately 1% of individuals older than 60 years [12].

The major neuropathological findings are a loss of pigmented dopaminergic neurons in the substantia nigra and the presence of Lewy bodies. However, cortical A $\beta$  may be present when PD patients develop dementia along with Lewy bodies in the neocortex. This suggests a central role for A $\beta$  in several types of dementia.

Frontotemporal lobe degeneration FTLD accounts for 20% of cases of dementia in post mortem studies [13]. Neuropathologically, there is atrophy of frontal and temporal lobes, severe neuronal loss, gray and white matter gliosis, and superficial laminar spongiosis, with absence of amyloid aggregates. In many cases, there is accumulation of insoluble tau or TDP43 within neurons and glia [14].

Molecular neuroimaging techniques such as positron emission tomography (PET) have been used to explore *in vivo* the molecular mechanisms of dementia at their sites of action. This permits detection of subtle pathophysiological changes in the brain at asymptomatic stages, when there is no evidence of anatomic changes on computer tomography CT or magnetic resonance imaging MRI [15].

Molecular neuroimaging thus possesses greater potential for accurate, early, and differential diagnosis as well as monitoring of disease progression and therapeutic effects [16]. These techniques have been extensively used to examine cerebral glucose metabolism, neurotransmitter and neuroreceptor systems along with the enzymes associated with their synthesis and metabolism, neuroinflammatory processes as well as specific markers of disease.

## Glucose metabolism

Fluorodeoxyglucose (FDG) PET, mainly used for the differential diagnosis of dementia, is the neuroimaging technique that yields the highest prognostic value, providing a diagnosis of presymptomatic AD two or more years before the full dementia picture is manifested [17, 18]. Several studies have evaluated regional cerebral glucose metabolism with FDG PET.

► **Without specific biological markers, only direct pathological examination can provide a definitive diagnosis.**

► **Molecular neuroimaging has great potential for accurate, early and differential diagnosis.**

A typical pattern of reduced temporoparietal FDG uptake with sparing of the basal ganglia, thalamus, cerebellum, and primary sensorimotor cortex is typical of AD [19]. Patients with DLB present with hypometabolism in the occipital and temporoparietal areas, with relative preservation of the posterior cingulate gyrus while FTLD patients present with reduced frontal and temporal metabolism (Figure 1).

Single Photon Emission Computed Tomography (SPECT) studies evaluating regional cerebral blood flow (rCBF) have shown a similar pattern as the one described for FDG-PET studies, with relative rCBF paucity in the temporoparietal regions [20]. FDG-PET might improve diagnostic and prognostic accuracy, thereby reducing both disease and treatment-related morbidity of patients with AD [21] due to its high sensitivity (94%) for detecting temporoparietal hypometabolism in patients with probable AD [22].

In a multicenter study, the prognostic value of FDG-PET showed a high degree of sensitivity (93%) and moderate specificity (73%) for prediction of progressive dementia [18]. Posterior cingulate and temporoparietal hypometabolism was observed in MCI patients when compared to controls. Progression of some of these patients to probable AD showed an additional bilateral hypometabolism in prefrontal areas, with further reductions in the posterior cingulate and parietal cortex. No such changes were observed in the MCI group that remained stable [23].

## Neurotransmitter systems

Molecular imaging techniques can also assess neurotransmitter systems *in vivo*. The evaluation of neurotransmitter functions in the brain is helpful for the determination and monitoring of treatment protocols, prediction of disease progression, as well as for the early diagnosis of dementia. Though the focus of neuroreceptor studies in AD has been the study of nicotinic acetylcholine receptors (nAChRs), several other neurotransmitter/neuroreceptor systems were also evaluated in dementia [24-29].

In a variety of central processes, nAChRs have been implicated, such as memory and cognition [30]. Abnormally low densities of nAChRs have been measured *in vitro* in autopsy brain tissue of AD patients. There is great interest in developing radiotracers to image nAChRs noninvasively in order to evaluate receptor impairments, even at a presymptomatic stage of AD, as well as monitoring drug treatment outcomes [31].

Typical cerebral distribution of nAChR in elderly control subjects is shown in Figure 2. PET studies revealed a reduced uptake and binding of  $^{11}\text{C}$ -nicotine in the temporal and frontal cortices of AD patients [32]. However, studies using 2- $^{18}\text{F}$  fluoro-A-85380 found no evidence of *in vivo* nAChR loss in early AD despite significant cognitive impairment [33]. Functional imaging of cholinergic neurotransmission is a useful strategy for the determination of the treatment protocol of demented patients.

Treatment with cholinergic drugs, such as Tacrine and Aricept (donepezil), in AD patients could lead to recovery of the nAChRs in the brain, as visualized by PET. Tacrine treatment increased cerebral blood flow, cerebral glucose utilization, and uptake of  $^{11}\text{C}$ -nicotine to the brain paralleled by improved neuropsychological performance. Changes in nicotinic receptors and blood flow were observed after three weeks of treatment while changes in glucose metabolism were measured after three months of treatment [34, 35].

Functional studies have also evaluated enzymes directly involved in the hydrolysis of acetylcholine (ACh). PET studies using  $^{11}\text{C}$  MP4A and  $^{11}\text{C}$  PMP have shown markedly reduced acetylcholinesterase (AChE) activity in AD [36] while studies with  $^{11}\text{C}$  donepezil revealed lower binding in AD patients, reductions that correlated with dementia severity [37]. These tracers have also been used to assess AChE occupancy by orally administered AChE inhibitors [38].

Dopaminergic neuronal loss in DLB and PD with dementia can be assessed by examining dopaminergic terminals with PET or SPECT, using ligands specific for the dopamine transporter, such as  $^{123}\text{I}$   $\beta$  CIT,  $^{123}\text{I}$  FPCIT or  $^{11}\text{C}$ -WIN [39], or for the vesicular monoamine transporter type 2 (VMAT2) with tracers such as  $^{11}\text{C}$ -DTBZ or  $^{18}\text{F}$ -AV133 (Figure 3) [40]. Evaluation of dopamine synthesis by  $^{18}\text{F}$  FDOPA PET also showed a marked reduction in striatal accumulation in DLB patients [41], suggesting that the assessment of dopaminergic terminals would help in the differential diagnosis of dementia.

## Neuroinflammation

Microglial activation is a useful indicator of neuroinflammation and can be used to assess anti-inflammatory therapies. Activated microglia has been examined using  $^{11}\text{C}$ -PK11195, a tracer for the peripheral benzodiazepine receptor (PBR). Studies with  $^{11}\text{C}$ -PK11195 PET demonstrated

► **FDG-PET might improve diagnostic and prognostic accuracy.**

► **Molecular imaging can assess neurotransmitter systems *in vivo*.**

a significant increase in microglial activation in AD brains, and while a correlation with dementia severity has been shown [42], the increase in microglial activation is not associated with A $\beta$  deposition [43]. Efforts are focused on developing PBR radiotracers that are more sensitive [44].

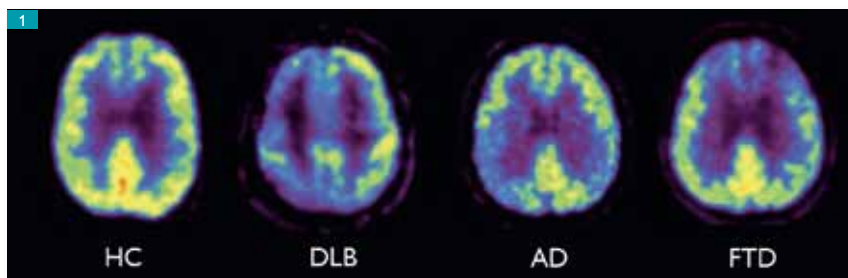
## Amyloid imaging

Neurofibrillary tangles (NFT) and A $\beta$  senile plaques are the neuropathological hallmarks of AD. Whilst NFTs are intraneuronal bundles of paired helical filaments mainly composed of the aggregates of an abnormally phosphorylated form of tau protein [45], neuritic plaques consist of dense extracellular aggregates of amyloid  $\beta$ -peptide (A $\beta$ ) [46], surrounded by reactive gliosis and dystrophic neurites. A $\beta$  is a 4 kDa 39–43 amino acid metalloprotein derived from the proteolytic cleavage of the amyloid precursor protein (APP), by  $\beta$  and  $\gamma$ -secretases [47].

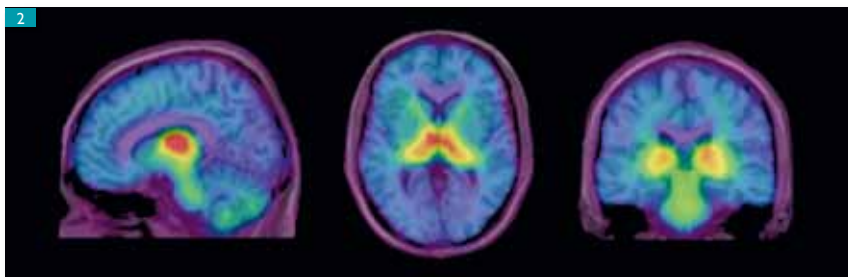
To date, all evidential analysis strongly supports the notion that an imbalance between the production and the removal of A $\beta$ , leading to its progressive accumulation, is central to AD pathogenesis [48]. While at this point there is no cure for AD, a deeper understanding of the molecular mechanisms of A $\beta$  formation, degradation, and neurotoxicity is being translated into new therapeutic and molecular imaging approaches [8, 49].

Amyloid imaging is providing quantitative information on A $\beta$  burden *in vivo*, leading to new insights into A $\beta$  deposition in the brain and facilitating research of dementing diseases [50]. The most successful and widely used of the currently available amyloid tracers,  $^{11}\text{C}$ -PiB has been shown to possess high affinity for fibrillar A $\beta$ . This allows the examination of a large spectrum of diseases where A $\beta$  may play a role, as well as in other neurodegenerative diseases associated with misfolded proteins such as prion diseases, synucleopathies or tauopathies (Figure 4) [51–53].

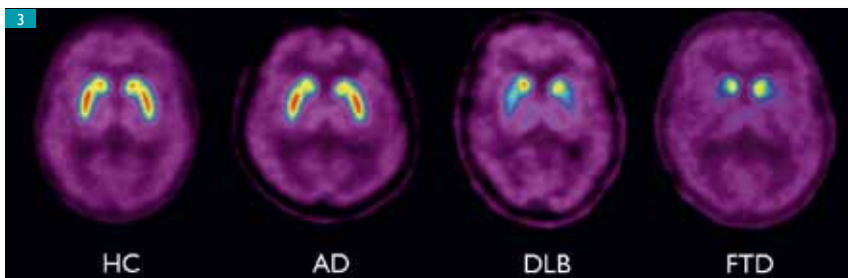
On visual inspection cortical retention of  $^{11}\text{C}$ -PiB, regardless of disease severity, is markedly elevated in AD [50]. The regional brain distribution is similar in both AD and DLB being highest in frontal, cingulate, precuneus, striatum, parietal, and lateral temporal cortex (Figure 4). The regional retention of  $^{11}\text{C}$ -PiB reflects the regional density of A $\beta$  plaques, as reported at autopsy [54] as when measured by quantification of immunohistochemical staining of brain slices, with a higher plaque density in the frontal cortex than in hippocampus, consistent with previous neuropathological and PiB PET reports [50, 55].



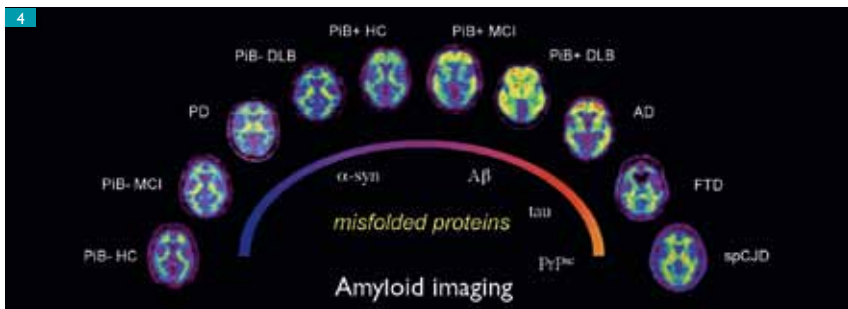
▲ Figure 1. Typical patterns of glucose metabolism as measured by FDG in healthy elderly controls (HC), dementia with Lewy bodies (DLB), Alzheimer's disease (AD) and frontotemporal dementia (FTD).



▲ Figure 2. PET-MRI fused images showing the regional distribution of nicotinic acetylcholine receptors (nAChR) in an elderly healthy control as measured by 2- $^{18}\text{F}$ -A85380.

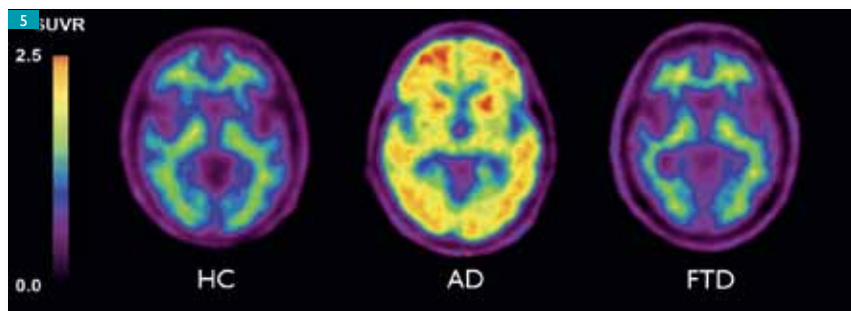


▲ Figure 3. Representative transaxial PET images of  $^{18}\text{F}$ -AV133 binding to the vesicular monoamine transporter type 2 (VMAT2) in a healthy control (HC) subject, Alzheimer's disease (AD), dementia with Lewy bodies (DLB), and frontotemporal dementia (FTD) patients.

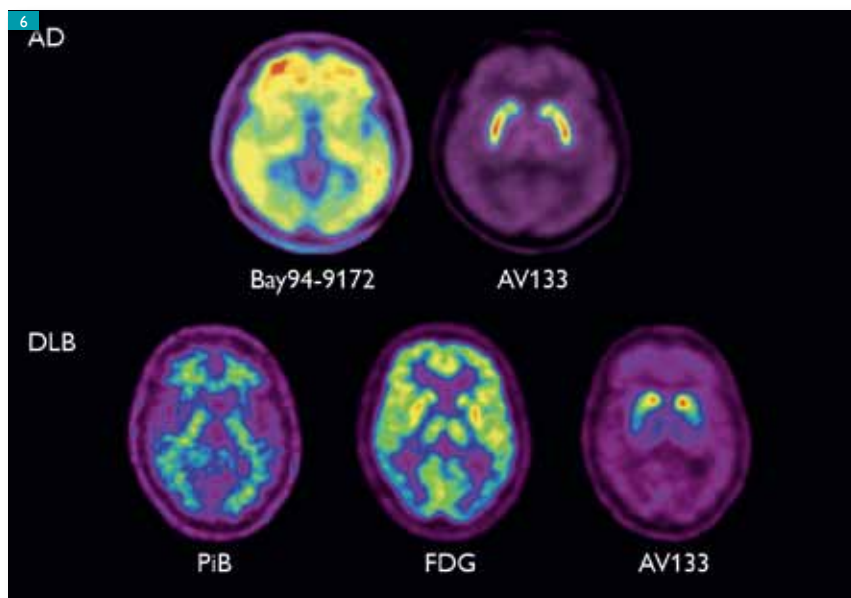


Both quantitative and visual assessment of  $^{11}\text{C}$ -PiB-PET images presents a pattern of  $^{11}\text{C}$ -PiB retention that seems to replicate the sequence of A $\beta$  deposition found at autopsy [56]. With initial deposition being found in the orbitofrontal cortex and gyrus rectus, followed by the cingulate gyrus and precuneus, the remaining prefrontal cortex and lateral

▲ Figure 4. Amyloid imaging with  $^{11}\text{C}$ -PiB in the spectrum of neurodegenerative diseases characterized by the aggregation of misfolded proteins, such as A $\beta$ ,  $\alpha$ -synuclein, tau and PrPsc.



▲ Figure 5. Transaxial PET images obtained with a novel  $^{18}\text{F}$  labeled radiotracer  $^{18}\text{F}$ -BAY94-9712, showing high cortical and subcortical gray matter retention in the Alzheimer's disease (AD) patient, while no cortical retention is observed in neither the healthy age-matched control (HC) nor the frontotemporal dementia (FTD) patient.



▲ Figure 6. Multimodality imaging. Combination of amyloid and VMAT2 imaging in an Alzheimer's disease (AD) patient where despite the high retention of  $^{18}\text{F}$ -BAY94-9712 there is no reduction of striatal monoaminergic terminals as assessed by  $^{18}\text{F}$ -AV133 (top row). Combination of amyloid, FDG and VMAT2 imaging in a dementia with Lewy bodies (DLB) patient where there is no retention of  $^{11}\text{C}$ -PiB, glucose hypometabolism is observed in the lateral occipital cortex and marked reduction of monoaminergic terminals as assessed by  $^{18}\text{F}$ -AV133 is observed in the striatum (bottom row).

temporal cortex, and finally to the parietal cortex.

The  $\text{A}\beta$  burden as measured by PiB, matches histopathological reports of  $\text{A}\beta$  distribution in aging and dementia. It appears to be more accurate than FDG for the diagnosis of AD [57] and is an excellent aid in the differential diagnosis of AD from FTD [50, 58] (Figure 4). The ApoE  $\epsilon 4$  status is associated with higher  $^{11}\text{C}$ -PiB retention [50].

High striatal  $\text{A}\beta$  deposition seems to be typical for carriers of familial forms of AD, whilst ApoE  $\epsilon 4$  carriers, independent of diagnosis or disease severity, present with higher  $\text{A}\beta$  burden than non- $\epsilon 4$  carriers. Characterization of the binding properties of PiB has shown that despite binding to other misfolded proteins *in vitro*, PiB is extremely selective for  $\text{A}\beta$  at the concentrations achieved during a PET scan.  $\text{A}\beta$  burden as assessed by PET does not correlate with measures of cognition or cognitive decline in AD [50].

Approximately 30% of apparently healthy older people, and 50–60% of people with mild cognitive impairment, present with cortical  $^{11}\text{C}$ -PiB retention (Figure 4). In these groups,  $\text{A}\beta$  burden does correlate with episodic memory and rate of memory decline [59]. These observations suggest that  $\text{A}\beta$  deposition is not part of normal ageing, supporting the hypothesis that  $\text{A}\beta$  deposition occurs well before the onset of symptoms and is likely to represent preclinical AD [50, 59]. Further longitudinal observations, coupled with different disease-specific tracers and biomarkers are required not only to confirm this hypothesis, but also to better elucidate the role of  $\text{A}\beta$  deposition in the course of AD.

Development of promising new  $\text{A}\beta$  imaging ligands labeled with isotopes having longer radioactive half-lives and acceptable radiation exposure, such as the case of  $^{18}\text{F}$ -BAY94-9712 [60] (Figure 5), will permit widespread application of this technique. They will also provide the accurate, reliable, and reproducible quantitative statements of  $\text{A}\beta$  burden, essential for therapeutic trial recruitment and for the evaluation of disease-specific treatments directed at removing  $\text{A}\beta$ .

As new treatments in clinical trials are aimed at preventing or slowing AD progression, either by preventing  $\text{A}\beta$  generation or deposition, or increasing the clearance of  $\text{A}\beta$ , the role of imaging and quantifying  $\text{A}\beta$  burden *in vivo* is becoming increasingly crucial, being acknowledged as part of newly proposed diagnostic criteria [61]. Although these treatments are aimed at AD, amyloid imaging findings suggest that they may have value in other dementias such as DLB, where  $\text{A}\beta$  deposition is present.

## Conclusion

Most dementias are characterized by a progressive decline in cognitive function, having a devastating effect on both the sufferer and their caregivers, inflicting a tremendous socioeconomic impact not only on families but also on the public health system. As a common risk factor for many neurodegenerative diseases is age, the increasing age of the population in developed countries suggests that if unchecked, these disorders will become increasingly prevalent and burdensome to our societies.

The clinical diagnosis is typically based on progressive cognitive impairments whilst excluding other diseases. Clinical diagnosis of sporadic disease is however challenging, often presenting mild and non-specific symptoms attributable to diverse and overlapping pathology presenting

similar phenotypes. In most cases, confirmation of diagnosis still relies on autopsy.

The neurodegenerative process usually begins decades before symptoms are evident, making early identification based on structural neuroimaging extremely difficult. This in turn precludes early intervention with disease-modifying medications during the presymptomatic period, which by arresting neuronal loss would presumably achieve the maximum benefits of such therapies.

Therefore, a change in the diagnostic paradigm is needed where diagnosis moves away from identification of signs and symptoms of neuronal failure, indicating that central compensatory mechanisms have been exhausted and extensive synaptic and neuronal damage is present, to the non-invasive detection of specific biomarkers for particular traits underlying the pathological process [62].

Given these disorders' complexity and sometimes overlapping characteristics, and despite recent advances in molecular neurosciences, it is unlikely that a single biomarker will be able to provide the diagnostic certainty required for the early detection of neurodegenerative diseases like AD. Especially those biomarkers needed to identify the at-risk individuals before the development of the typical phenotype.

Consequently, a multimodality approach combining biochemical and neuroimaging

methods is needed [63]. Multitracer studies such as the ones shown in Figure 6 can explore different molecular processes increasing the specificity of the diagnosis while helping select and customize treatment to potentially prevent or delay functional and irreversible cognitive loss.

Because new treatment strategies to prevent or slow disease progression through early-intervention are being developed and implemented there is an urgent need for early disease recognition. That is reflected in the necessity of developing sensitive and specific biomarkers, specific for a particular trait or traits underlying the pathological process, as adjuncts to clinical and neuropsychological tests. Molecular imaging might be able to address some of these important issues.

Dementia is a progressive journey to the end of the night. Maybe molecular imaging can assist us to get closer to the threshold of a new dawn, help us find a way out of the labyrinth, turning the whole journey to the end of the night, into a journey into the day.

## Acknowledgments

This work was supported in part by the National Health and Medical Research Council of Australia, the Austin Hospital Medical Research Foundation, Neurosciences Victoria, and NHMRC Grant 509166 ■

► **Maybe molecular imaging can turn the journey to the end of the night into a journey into the day.**

## References

- [1] Selkoe DJ. *Alzheimer's Disease is a Synaptic Failure*. Science. 2002; 298(5594): 789-791.
- [2] Jellinger K. *Morphology of Alzheimer Disease and Related Disorders*. In: Maurer K, Riederer P, Beckmann H, Eds. *Alzheimer Disease: Epidemiology, Neuropathology, Neurochemistry, and Clinics*. Berlin: Springer-Verlag; 1990. 61-77.
- [3] Masters CL, Beyreuther K. *The Neuropathology of Alzheimer's Disease in the Year 2005*. In: Beal MF, Lang AE, Ludolph AC, Eds. *Neurodegenerative Diseases: Neurobiology, Pathogenesis and Therapeutics*. Cambridge: Cambridge University Press; 2005. 433-440.
- [4] McKhann G, Drachman D, Folstein M, Katzman R, Price D, Stadlan EM. *Clinical Diagnosis of Alzheimer's Disease: Report of the NINCDS-ADRDA Work Group under the Auspices of Department of Health and Human Services Task Force on Alzheimer's Disease*. Neurology. 1984; 34: 939-944.
- [5] Petersen RC. *Mild Cognitive Impairment: Current Research and Clinical Implications*. Semin Neurol. 2007; 27(1): 22-31.
- [6] Petersen RC, Stevens JC, Gangali M, Tangalos EG, Cummings JL, DeKosky ST. *Practice Parameter: Early Detection of Dementia: Mild Cognitive Impairment (an evidence-based review)*. Report of the Quality Standards Subcommittee of the American Academy of Neurology. Neurology. 2001; 56(9): 1133-1142.
- [7] Petersen RC, Smith GE, Waring SC, Ivnik RJ, Tangalos EG, Koken E. *Mild Cognitive Impairment: Clinical Characterization and Outcome*. Arch Neurol. 1999; 56(3): 303-308.
- [8] Masters CL, Cappai R, Branham KJ, Villemagne VL. *Molecular Mechanisms for Alzheimer's Disease: Implications for Neuroimaging and Therapeutics*. J Neurochem. 2006; 97(6): 1700-1725.
- [9] Schneider J, Murray M, Banerjee S, Mann A. *EURO CARE: A Cross-national Study of Co-resident Spouse Carers for People with Alzheimer's Disease: I—Factors Associated with Carer Burden*. Int J Geriatric Psychiatry. 1999; 14(8): 651-661.

- [10] Johnson N, Davis T, Bosanquet N. *The Epidemic of Alzheimer's Disease. How can We Manage the Costs?* Pharmacoeconomics. 2000; 18(3): 215-223.
- [11] McKeith IG, Dickson DW, Lowe J, Emre M, O'Brien JT, Feldman H, et al. *Diagnosis and Management of Dementia with Lewy Bodies: Third Report of the DLB Consortium.* Neurology. 2005; 65(12): 1863-1872.
- [12] McKeith IG, Mosimann UP. *Dementia with Lewy Bodies and Parkinson's Disease.* Parkinsonism Relat Disord. 2004; 10 Suppl 1: S15-18.
- [13] Mott RT, Dickson DW, Trojanowski JQ, Zhukareva V, Lee VM, Forman M, et al. *Neuropathologic, Biochemical, and Molecular Characterization of the Frontotemporal Dementias.* J Neuropathol Exp Neurol. 2005; 64(5): 420-428.
- [14] Sergeant N, Delacourte A, Buée L. *Tau Protein as a Differential Biomarker of Tauopathies.* Biochimica Biophys Acta. 2005; 1739(2-3): 179-197.
- [15] Villemagne VL, Fodero-Tavoletti M, Pike Kerry E, Cappai R, Masters CL, Rowe CC. *The ART of Loss: Abeta Imaging in the Evaluation of Alzheimer's Disease and other Dementias.* Mol Neurobiol. 2008; 38(1): 1-15.
- [16] Silverman DH, Phelps ME. *Application of Positron Emission Tomography for Evaluation of Metabolism and Blood Flow in Human Brain: Normal Development, Aging, Dementia, and Stroke.* Mol Genet Metab. 2001; 74(1-2): 128-138.
- [17] Silverman DH, Gambhir SS, Huang HC, Schwimmer J, Kim S, Small GW, et al. *Evaluating Early Dementia With and Without Assessment of Regional Cerebral Metabolism by PET: A Comparison of Predicted Costs and Benefits.* J Nucl Med. 2002; 43(2): 253-266.
- [18] Silverman DH, Small GW, Chang CY, Lu CS, Kung de Aburto M, Chen W, et al. *Positron Emission Tomography in Evaluation of Dementia: Regional Brain Metabolism and Long-term Outcome.* JAMA. 2001; 286(17): 2120-2127.
- [19] Coleman RE. *Positron Emission Tomography Diagnosis of Alzheimer's Disease.* Neuroimaging Clin N Am. 2005; 15(4): 837-846.
- [20] Camargo EE. *Brain SPECT in Neurology and Psychiatry.* J Nucl Med. 2001; 42(4): 611-623.
- [21] Silverman DH, Cummings JL, Small GW, Gambhir SS, Chen W, Czernin J, Phelps ME. *Added Clinical Benefit of Incorporating 2-deoxy-2-[18F]fluoro-D-glucose with Positron Emission Tomography into the Clinical Evaluation of Patients with Cognitive Impairment.* Mol Imaging Biol. 2002; 4(4): 283-293.
- [22] Small GW, Mazziotta JC, Collins MT, Baxter LR, Phelps ME, Mandelkern MA, et al. *Apolipoprotein E Type 4 Allele and Cerebral Glucose Metabolism in Relatives at Risk for Familial Alzheimer Disease.* JAMA. 1995; 273(12): 942-947.
- [23] Drzezga A, Lautenschlager N, Siebner H, Riemenschneider M, Willoch F, Minoshima S, et al. *Cerebral Metabolic Changes Accompanying Conversion of Mild Cognitive Impairment into Alzheimer's Disease: a PET Follow-up Study.* Eur J Nucl Med Mol Imaging. 2003; 30(8): 1104-1113.
- [24] Sedvall G, Nybäck H, Farde L, Persson A. *Neurotransmitter Receptor Imaging in Alzheimer's Disease.* J Neural Transm Suppl. 1987; 24: 43-48.
- [25] Higuchi M, Yanai K, Okamura N, Meguro K, Arai H, Itoh M, et al. *Histamine H (1) Receptors in Patients with Alzheimer's Disease Assessed by Positron Emission Tomography.* Neuroscience. 2000; 99(4): 721-729.
- [26] Kemppainen N, Ruottinen H, Nägren K, Rinne JO. *PET Shows that Striatal Dopamine D1 and D2 Receptors are Differentially Affected in AD.* Neurology. 2000; 55(2): 205-209.
- [27] Kepe V, Barrio JR, Huang S, Ercoli L, Siddarth P, Shoghi-Jadid K, et al. *Serotonin 1A Receptors in the Living Brain of Alzheimer's Disease Patients.* Proc Natl Acad Sci USA. 2006; 103(3): 702-707.
- [28] Cohen RM, Andreason PJ, Doudet DJ, Carson RE, Sunderland T, et al. *Opiate Receptor Avidity and Cerebral Blood Flow in Alzheimer's Disease.* J Neurol Sci. 1997; 148(2): 171-180.
- [29] Piggott MA, Owens J, O'Brian J, Colloby S, Fenwick J, Wyper D, et al. *Muscarinic Receptors in Basal Ganglia in Dementia with Lewy Bodies, Parkinson's Disease and Alzheimer's Disease.* J Chem Neuroanat. 2003; 25(3): 161-173.
- [30] Villemagne VL, Musachio JL, Scheffel U. *Nicotine and Related Compounds as PET and SPECT Ligands.* In: *Neuronal Nicotinic Receptors: Pharmacology and Therapeutic Opportunities.* New York: John Wiley & Sons; 1998. 235-250.
- [31] Horti AG, Villemagne VL. *The Quest for Eldorado: Development of Radioligands for in vivo Imaging of Nicotinic Acetylcholine Receptors in Human Brain.* Curr Pharm Des. 2006; 12(30): 3877-3900.
- [32] Nordberg A. *In vivo Detection of Neurotransmitter Changes in Alzheimer's Disease.* Ann N Y Acad Sc. 1993; 695: 27-33.
- [33] Ellis J, Villemagne VL, Pradeep N, Mulligan R, Gong S, Smith C, et al. *Nicotinic Receptor Imaging with 2-[18F] F-A-85380 PET does not Differentiate early Alzheimer's Disease Patients from Healthy Controls.* J Nucl Med. 2007; 48(Suppl. 2): 7P.
- [34] Nordberg A, Amberla K, Shigeta M, Lundqvist H, Viitanen M, Hellström-Lindahl E, et al. *Long-term Tacrine Treatment in Three Mild Alzheimer Patients: Effects on Nicotinic Receptors, Cerebral Blood Flow, Glucose Metabolism, EEG, and Cognitive Abilities.* Alzheimer Dis Assoc Disord. 1998; 12(3): 228-237.
- [35] Nordberg A, Lundqvist H, Hartvig P, Andersson J, Johansson M, Hellström-Lindahl E, et al. *Imaging of Nicotinic and Muscarinic Receptors in Alzheimer's Disease: Effect of Tacrine Treatment.* Dement Geriatr Cogn Disord. 1997; 8(2): 78-84.
- [36] Iyo M, Namba H, Fukushi K, Shinotoh H, Nagatsuka S, Suhara T, et al. *Measurement of Acetylcholinesterase by Positron Emission Tomography in the Brains of Healthy Controls and Patients with Alzheimer's Disease.* Lancet. 1997; 349(9068): 1805-1809.
- [37] Okamura N, Funaki Y, Tashiro M, Kato M, Ishikawa Y, Muruyama M, et al. *In vivo Visualization of Donepezil Binding in the Brain of Patients with Alzheimer's Disease.* Br J Clin Pharmacology. 2008; 65(4): 472-479.

- [38] Shinotoh H, Aotsuka A, Fukushi K, Nagatsuka S, Tanaka N, Ota T, et al. *Effect of Donepezil on Brain Acetylcholinesterase Activity in Patients with AD Measured by PET*. *Neurology*. 2001; 56(3): 408-410.
- [39] O'Brien JT, Colloby S, Fenwick J, Williams D, Firbank M, Burn D, et al. *Dopamine Transporter Loss Visualized with FP-CIT SPECT in the Differential Diagnosis of Dementia with Lewy Bodies*. *Arch Neurol*. 2004; 61(6): 919-925.
- [40] Kung MP, Hou C, Goswami R, Ponde DE, Kilbourn MR, Kung HF. *Characterization of Optically Resolved 9-Fluoropropyl-Dihydrotetabenazine as a Potential PET Imaging Agent Targeting Vesicular Monoamine Transporters*. *Nucl Med Biol*. 2007; 34(3): 239-246.
- [41] Hu XS, Okamura N, Arai H, Higuchi M, Matsui T, Tashiro M, et al. *<sup>18</sup>F-Fluorodopa PET Study of Striatal Dopamine Uptake in the Diagnosis of Dementia with Lewy Bodies*. *Neurology*. 2000; 55(10): 1575-1577.
- [42] Edison P, Archer HA, Gerhard A, Hinz R, Pavese N, Turkheimer FE, et al. *Microglia, Amyloid, and Cognition in Alzheimer's Disease: An [<sup>11</sup>C](R) PK11195-PET and [<sup>11</sup>C] PIB-PET Study*. *Neurobiol Dis*. 2008; 32(3): 412-419.
- [43] Okello A, Edison P, Archer HA, Turkheimer FE, Kennedy J, Bullock R, et al. *Microglial Activation and Amyloid Deposition in Mild Cognitive Impairment: a PET Study*. *Neurology*. 2009; 72(1): 56-62.
- [44] Doorduyn J, de Vries EF, Dierckx RA, Klein HC, et al. *PET Imaging of the Peripheral Benzodiazepine Receptor: Monitoring Disease Progression and Therapy Response in Neurodegenerative Disorders*. *Curr Pharm Des*. 2008; 14(31): 3297-3315.
- [45] Michaelis ML, Dobrowsky RT, Li G. *Tau Neurofibrillary Pathology and Microtubule Stability*. *J Mol Neurosci*. 2002; 19(3): 289-293.
- [46] Masters CL, Simms G, Weinman NA, Multhaup G, McDonald BL, Bayreuther K. *Amyloid Plaque Core Protein in Alzheimer Disease and Down Syndrome*. *Proc Natl Acad Sci USA*. 1985; 82(12): 4245-4249.
- [47] Cappai R, White AR. *Amyloid Beta*. *Int J Biochem Cell Biol*. 1999; 31(9): 885-889.
- [48] Villemagne VL, Cappai R, Barnham KJ, Cherny RA, Opazo C, Novakovic KE, et al. *The A $\beta$  centric Pathway of Alzheimer's Disease*. In: Barrow CJ, Small BJ, Eds. *Abeta Peptide and Alzheimer's Disease*. London: Springer-Verlag; 2006. 5-32.
- [49] Masters CL, Beyreuther K. *Alzheimer's Centennial Legacy: Prospects for Rational Therapeutic Intervention Targeting the Abeta Amyloid Pathway*. *Brain*. 2006; 129(Pt 11): 2823-2839.
- [50] Rowe CC, Ng S, Ackerman U, Gong SJ, Pike K, Savage G, et al. *Imaging Beta-Amyloid Burden in Aging and Dementia*. *Neurology*. 2007; 68(20): 1718-1725.
- [51] Mathis CA, Bacskai BJ, Kajdasz ST, McLellan ME, Frosch MP, Hyman BT, et al. *A Lipophilic Thioflavin-T Derivative for Positron Emission Tomography (PET) Imaging of Amyloid in Brain*. *Bioorg Med Chem Lett*. 2002; 12(3): 295-298.
- [52] Price JC, Klunk WE, Lopresti BJ, Lu X, Hoge JA, Ziolkowski SK, et al. *Kinetic Modeling of Amyloid Binding in Humans using PET Imaging and Pittsburgh Compound-B*. *J Cereb Blood Flow Metab*. 2005; 25(11): 1528-1547.
- [53] Ye L, Morgenstern JL, Gee AD, Hong G, Brown J, Lockhart A. *Delineation of Positron Emission Tomography Imaging Agent Binding Sites on Beta-Amyloid Peptide Fibrils*. *J Biol Chem*. 2005; 280(25): 23599-23604.
- [54] Ikonomic MD, Klunk WE, Abrahamson EE, Mathis CA, Price JC, Tsopelas ND, et al. *Post-Mortem Correlates of In Vivo PiB-PET Amyloid Imaging in a Typical Case of Alzheimer's Disease*. *Brain*. 2008; 131(Pt 6): 1630-1645.
- [55] Leinonen V, Alafuzoff I, Aalto S, Suolonen T, Savolainen S, N agren K, et al. *Assessment of Beta-Amyloid in a Frontal Cortical Brain Biopsy Specimen and by Positron Emission Tomography with Carbon 11-labeled Pittsburgh Compound B*. *Arch Neurol*. 2008; 65(10): 1304-1309.
- [56] Thal DR, R ub U, Orantes M, Braak H. *Phases of A Beta-Deposition in the Human Brain and its Relevance for the Development of AD*. *Neurology*. 2002; 58: 1791-1800.
- [57] Ng S, Villemagne VL, Berlangieri S, Lee ST, Cherk M, Gong SJ, et al. *Visual Assessment versus Quantitative Assessment of <sup>11</sup>C-PIB PET and <sup>18</sup>F-FDG PET for Detection of Alzheimer's Disease*. *J Nucl Med*. 2007; 48(4): 547-552.
- [58] Rabinovici GD, Furst AJ, O'Neil JP, Racine CA, Mormino EC, Baker SL, et al. *<sup>11</sup>C-PIB PET Imaging in Alzheimer Disease and Frontotemporal Lobar Degeneration*. *Neurology*. 2007; 68(15): 1205-1212.
- [59] Villemagne VL, Pike KE, Darby D, Maruff P, Savage G, Ng S, et al. *Abeta Deposits in Older non-Demented Individuals with Cognitive Decline are Indicative of Preclinical Alzheimer's Disease*. *Neuropsychologia*. 2008; 46(6): 1688-1697.
- [60] O'Keefe GJ, Saunders TH, Ng S, Ackerman U, Tochon-Danguay HJ, Chan JG, et al. *Radiation Dosimetry of Beta<sup>+</sup>-Amyloid Tracers <sup>11</sup>C-PiB and <sup>18</sup>F-BAY94-9172*. *J Nucl Med*. 2009; 50(2): 309-315.
- [61] Dubois B, Feldman H, Jacova C, DeKosky S, Barberger-Gateau P, Cummings J, et al. *Research Criteria for the Diagnosis of Alzheimer's Disease: Revising the NINCDS-ADRDA Criteria*. *Lancet Neurol*. 2007; 6(8): 734-746.
- [62] Clark CM, Davatzikos C, Borthakur A, Newberg A, Leight S, Lee VM-Y, et al. *Biomarkers for Early Detection of Alzheimer Pathology*. *Neurosignals*. 2008; 16(1): 11-18.
- [63] Shaw LM, Korecka M, Clark CM, Lee VM-Y, Trojanowski JQ. *Biomarkers of Neurodegeneration for Diagnosis and Monitoring Therapeutics*. *Nat Rev Drug Discov*. 2007; 6(4): 295-303.

# Three-dimensional real-time *in vivo* magnetic particle imaging

J. Borgert  
B. Gleich  
J. Rahmer

Philips Research Laboratories, Hamburg, Germany.

H. Dahnke

Philips Healthcare, Hamburg, Germany.

J. Weizenecker

Karlsruhe University of Applied Sciences, Karlsruhe, Germany.

*The research described in this article was originally published in a Letter to the Editor in Physics in Medicine and Biology [1]. This is available at <http://stacks.iop.org/0031-9155/54/L1>, and includes additional images and films.*

► **MPI is a new tomographic imaging technique using iron oxide based nanoparticles.**

Magnetic particle imaging (MPI) is a new tomographic imaging method invented in 2001 by Philips Research, first published in Nature in 2005 [2] and shortly afterwards in Medicamundi [3]. MPI uses the magnetic properties of iron oxide based nanoparticles, called tracer materials in the context of MPI, to determine the local concentration. The measurement is inherently quantitative in that it shows exactly how much material is present at a certain spot. Furthermore, MPI promises to deliver high spatial and temporal resolution with a sensitivity exceeding that of magnetic resonance imaging (MRI) [4, 5, 6] in the detection of iron oxide.

► **MPI promises to deliver high spatial and temporal resolution.**

Although MPI is capable of rapid three-dimensional (3D) dynamic imaging of magnetic tracer materials, until now only static [2, 3] and dynamic two-dimensional (2D) phantom [7] experiments with high tracer concentrations have been demonstrated. To pave the way for meaningful clinical applications, the next important step was to demonstrate that 3D imaging would work *in vivo* while limiting the tracer dose to clinically approved concentrations.

MPI can use commercial tracer materials made from iron oxide. These are generally known as superparamagnetic iron oxides (SPIOs). One such material is Resovist<sup>®</sup>, made by Bayer Schering Pharma [8], that is approved for use as an MRI contrast agent in the diagnosis of liver carcinoma.

This report demonstrates that a single bolus injection of from 8  $\mu\text{mol}$  (Fe)/kg up to 45  $\mu\text{mol}$

(Fe)/kg Resovist<sup>®</sup> is enough to acquire three-dimensional real-time volumetric images of a beating mouse heart. This is with an acquisition time of 21.5ms per volume and a spatial resolution sufficient to resolve all heart chambers. As no breath hold was required during image acquisition, and no retrospective triggering was needed during reconstruction, the above represents the raw performance of the imaging system.

While these abilities are convincing, the ultimate question remains: What are the medical applications that would benefit from MPI? Because the tracer material is formulated for intravenous injection, the obvious applications are those that can capitalize on the material staying in the blood stream for a certain time. One widespread application that meets this criterion is the diagnosis and assessment of cardiovascular disease (CVD).

One of the most important aspects of CVD is coronary artery disease (CAD). It is responsible for the condition known as myocardial infarction, with unstable or stable angina, which is commonly referred to as a “heart attack”. All of these conditions are caused by either a partial closure (stenosis), or a complete obstruction (occlusion), of vessels that supply the heart muscle with blood, resulting in necrosis of the heart muscle.

In acute cases, a direct referral to the cath lab for catheterization and angiography, with the option to intervene by angioplasty and stenting, is still the most common course of action. However, in subacute cases, a clear

trend to replace this invasive step with non-invasive methods gave rise to the use of contrast enhanced computed tomography (CT) [9, 10] for coronary angiography. Consequently, only those patients that show a stenosis or obstruction in the CT exam will be subject to an intervention.

In most cases, these diagnostic steps are preceded by other examinations to determine the status of the heart, such as electrocardiography (ECG). They can also include a determination of the levels of certain enzymes released following cell death in the heart muscle. These include creatine phosphokinase (CPK) and more recently, troponin [11]. In some countries, the diagnostic process is combined with a cardiac stress/rest test using single photon emission computed tomography (SPECT) [12]. Sometimes positron-emission tomography (PET) [13, 14] is used to determine the myocardial perfusion. Areas of decreased perfusion can indicate the presence of a stenosis or occlusion, increasing the diagnostic evidence and indicating the need for intervention.

All of this information is collected to develop a comprehensive understanding of the state of the patient's heart. MPI can possibly provide an alternative source of information for both the diagnostic and the interventional scenario for cardiovascular disease. To be more specific, most of the information that is now collected by deploying diverse modalities can be acquired by MPI alone.

As shown in the study presented in this article in a pre-clinical setting, the tracer material can be followed through various parts of the heart and the cardiovascular system. After the material has entered the right atrium by way of the vena cava, it is possible to assess wall motion of the right ventricle and the ejection dynamics into the pulmonary vessel system. In a similar manner, left ventricle wall motion and ejection dynamics complete the function information picture.

In a next step, the coronary blood supply can be imaged in a similar manner to an angiography performed in the cath lab. However, the information delivered by MPI is three-dimensional and acquired without the use of any harmful radiation. Immediately after imaging the coronary blood supply, the myocardial vitality can be assessed by measuring myocardial perfusion. In a similar way to the cardiac stress/rest test using SPECT or PET, this information will be correlated to the state of the coronaries with respect to stenosis or occlusions.

As a result, most of the information used today to form a comprehensive overview of the state of the cardiovascular system, could be acquired with MPI in a single session. However, determination of the levels of the enzymes CPK and troponin in the blood, indicating cell death in the heart-muscle, would still have to be done separately.

MPI could also address future diagnostic options, for example, determination of plaque burden. Using MPI, a quantitative measurement of the accumulated iron, and therefore the plaque burden, is within reach. There is widespread research effort into deciphering the accumulation processes that could be exploited to label vulnerable plaque with iron oxide [15]. The coatings of the tracer materials determine the physiological properties and the pharmacokinetics of the tracer. Therefore, it may be possible that improved tracer materials with custom made coatings to support the accumulation process will lead to vast improvements in efficiency of the method.

For other diseases, determination of the blood supply of certain tissues, such as tumor tissue in the case of cancer, could provide interesting diagnostic information. New studies have investigated the importance of measuring micro-vascularization for tumor staging [16].

Specifically during therapy, monitoring of the blood supply can indicate the success of the therapy by showing a decrease in the blood supply. Similar to the case with plaque, there are ongoing investigations into whether iron oxide based tracer materials have the potential to migrate into tumor tissue or lymph nodes after systemic injection [17].

Focusing on the imaging of the cardiovascular system of a mouse, this article indicates that medical applications of MPI that make use of an injection of tracer materials into the blood stream are indeed feasible. This article goes on to show that it is possible to track a bolus injection through the cardiovascular system of a living mouse using 3D MPI is now possible. Being able to use tracer concentrations between 8 and 45  $\mu\text{mol (Fe)/l}$ , and with 40  $\mu\text{mol (Fe)/l}$  still being considered a safe dosage, the sensitivity is already high enough for imaging clinically approved dosages of commercially available MRI contrast agents.

All studies have been approved and carried out in accordance with the appropriate local guidelines and regulations.

► **MPI could acquire comprehensive information on the cardiovascular system in a single session.**

► **A quantitative assessment of plaque burden is now within reach.**

# MPI: the basic principles

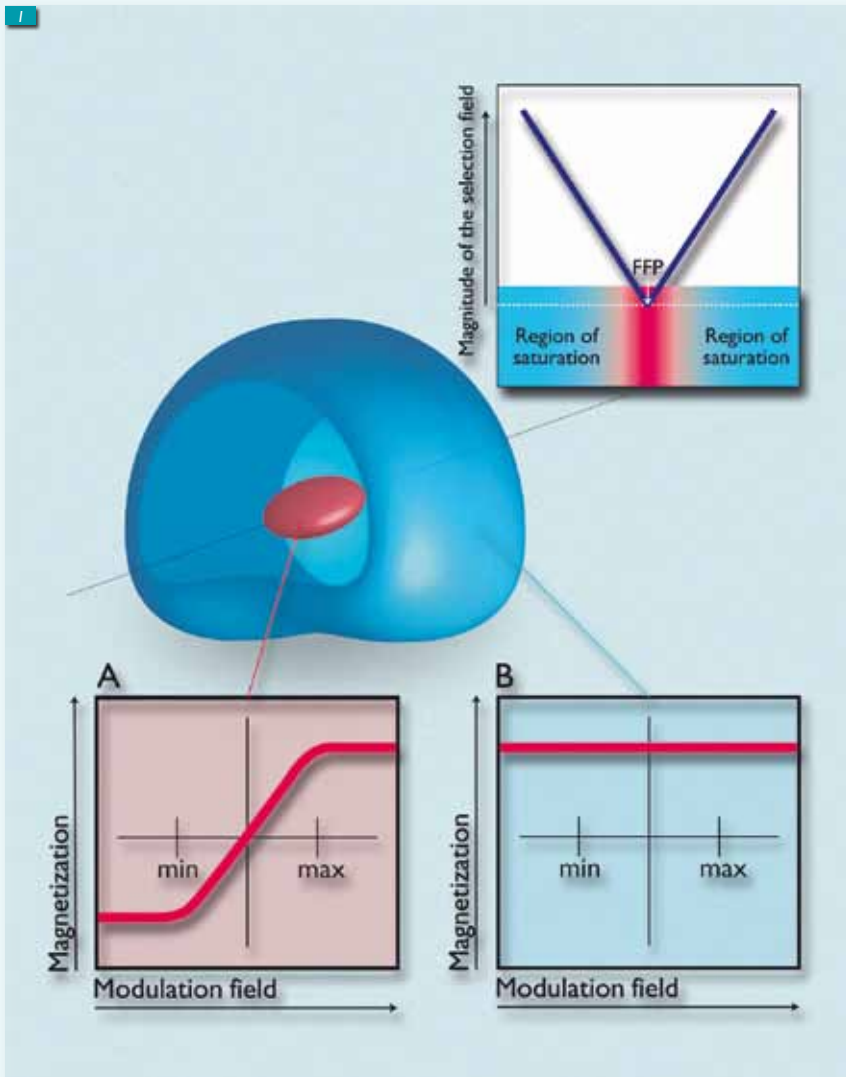


**Figure 1.** Principle of MPI: a “selection field” is applied that is relatively high at the edges but approaches zero in the center. This central point is referred to as the “field-free point” (FFP). Any magnetic material outside the FFP, i.e. located in the high field, will be saturated and therefore remains unaffected by an applied radio-frequency field, while magnetic material within the closely defined FFP will be free to respond.

If an additional weak radio-frequency field is applied, the magnetization of material at the FFP (A) will start to oscillate, inducing a signal in the detection circuit, while magnetic material in the saturated areas will be unaffected (B). This signal can thus be unambiguously assigned to the narrow field-free region. By systematically varying the position of the field-free area in the object, a map can be created that gives the spatial distribution of the magnetic particles.

Magnetic Particle Imaging (MPI) is a new imaging technique based on the magnetic properties of iron oxide based nanoparticles. The measurement is inherently quantitative, and promises to deliver high spatial and temporal resolution with a sensitivity exceeding that of conventional magnetic resonance imaging (MRI).

In MPI, a “selection field” is applied that is high at the edges but approaches zero in the center. This central point is referred to as the “field-free point” (FFP). Any magnetic material outside the FFP, i.e. located in the high field, will be saturated and therefore unaffected by any applied radio-frequency field, while magnetic material within the closely defined FFP will be free to respond (Figure 1).

If an oscillating “modulation field” is applied, the magnetic material in the FFP will respond with oscillations at the same frequency as the applied field, but much weaker. However, the induced oscillations are accompanied by a series of higher harmonic frequencies. These higher frequencies can be separated from the applied signal by appropriate filtering, providing a signal that can be unambiguously assigned to the narrow FFP. The resolution in MPI is determined solely by the size of the area of non-saturated particles around the FFP, independently of the size of the detectors, making it possible to achieve a resolution of 1 mm or less.

Scanning the FFP through the region of interest provides the data for a tomographic image. The FFP can be scanned through the region of interest by applying three additional orthogonal homogeneous magnetic fields, referred to as “drive fields”. The drive field in the vertical (z) direction is produced by the selection field coils. The drive fields in the two orthogonal (x, y) directions are produced by dedicated coils, which are driven at the same amplitude. Appropriate adjustment of the drive fields can position the FFP at any desired point within the object.

## Technical introduction

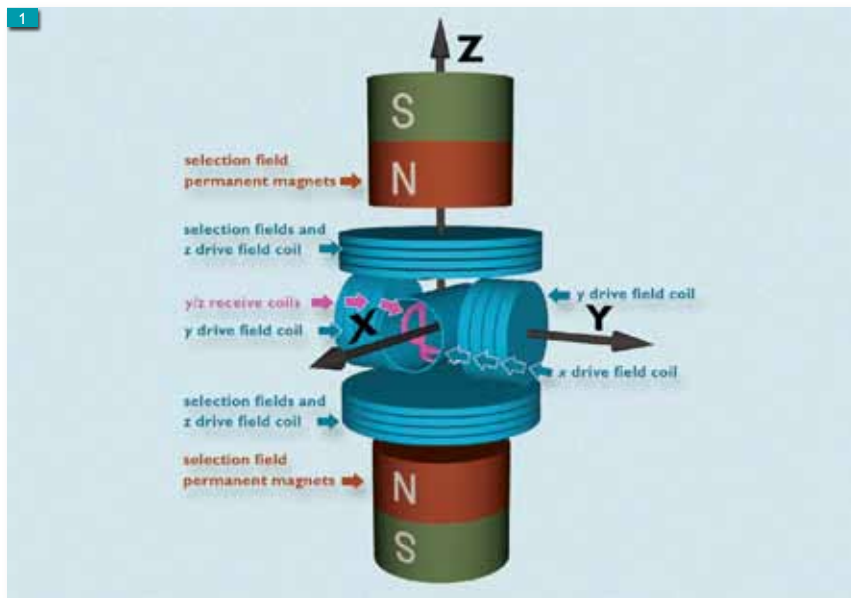
The basic principles of MPI are outlined in the Intermezzo accompanying this article. Articles with more detail have been published previously in Nature [2] and Medicamundi [3]. In brief, MPI requires ferromagnetic nanoparticles as a tracer material, a static magnetic field (“selection field”), an oscillating field (“drive field”), and signal receive coils. The basic scanner setup is schematically shown in Figure 1. The selection field provides a single field-free point in space (FFP), while it is non-zero at all other spatial positions. This field topology can be achieved using a Helmholtz-type coil set up supplied with opposing currents.

In close vicinity to the FFP, the orientation of the magnetization of the ferromagnetic nanoparticles will easily align with an applied oscillating drive field. At all other positions, the orientation is forced to align with the local selection field direction. Since the particles have a non-linear magnetization curve, magnetization reorientation occurring around the FFP induces a signal in the receive coils at the drive field frequency  $f_0$  and its higher harmonics.

The signal is proportional to the concentration of particles at this position. If the FFP is moved over the object in a sufficiently dense trajectory, it can be used to image the local particle concentration. For fast spatial encoding, the FFP can be moved using homogeneous oscillating fields. It turns out, that sufficiently large drive field amplitude induces one-dimensional motion of the FFP over the object enabling one-dimensional spatial encoding.

To encode three spatial coordinates, two additional orthogonal drive fields are necessary. If the respective drive frequencies differ only slightly, the FFP will follow a three-dimensional Lissajous trajectory. Broadband acquisition of the signal generated by the changing particle magnetization under the influence of the FFP motion yields the MPI signal. The image is reconstructed from the information encoded in the higher harmonics and combinations of the three drive frequencies.

To establish the relation between frequency response and spatial position, a calibration scan with a dedicated voxel-sized reference sample has to be performed once for a given combination of scanner set up and tracer material. The “system function” acquired in this calibration scan is necessary for solving the inverse reconstruction problem [18].



The original MPI scanner setup [2, 3] combined one-dimension FFP motion as described above with orthogonal mechanical FFP movement to achieve two-dimensional spatial encoding. However, the mechanical spatial encoding scheme was far too slow to be useful for practical medical applications. A second drive field was introduced to overcome the speed limitations for two-dimensional imaging [7]. Real-time MPI with 25 frames per second was demonstrated in phantom experiments using a two-directional Lissajous FFP trajectory.

While these experiments required tracer concentration orders of magnitude higher than clinically applicable dosages, simulations [18] indicated that imaging with physiologically tolerable tracer dosages could be feasible. Despite these theoretical findings, agglomeration of the nanoparticles due to contact with tissue could not be excluded for *in-vivo* imaging. This would strongly degrade the MPI signal while leaving the MRI performance almost unchanged.

To realize the level of speed and sensitivity required for volumetric *in-vivo* imaging, several innovations and improvements had to be introduced into the scanner concept previously used for dynamic two-directional imaging.

## Methods

Figure 1 schematically shows the basic setup of the 3D scanner. The scanner has an effective bore of 32 mm. A pair of permanent magnets and a pair of coils produces the selection field gradient. The permanent magnets contribute  $3 T\mu_0^{-1}m^{-1}$  and the coils  $2.5 T\mu_0^{-1}m^{-1}$  to the

▲ Figure 1. Schematic scanner setup. The mouse was inserted into the x drive/receive-coil cylinder using an animal support. The bore diameter is 32 mm. The selection field is generated by both the permanent magnets and the coil pair in z direction. The drive field coils can move the FFP in all three spatial coordinates. For signal reception, each spatial component of the magnetization is detected by a corresponding receive coil. In the x direction, the drive field coil is also used for signal reception.

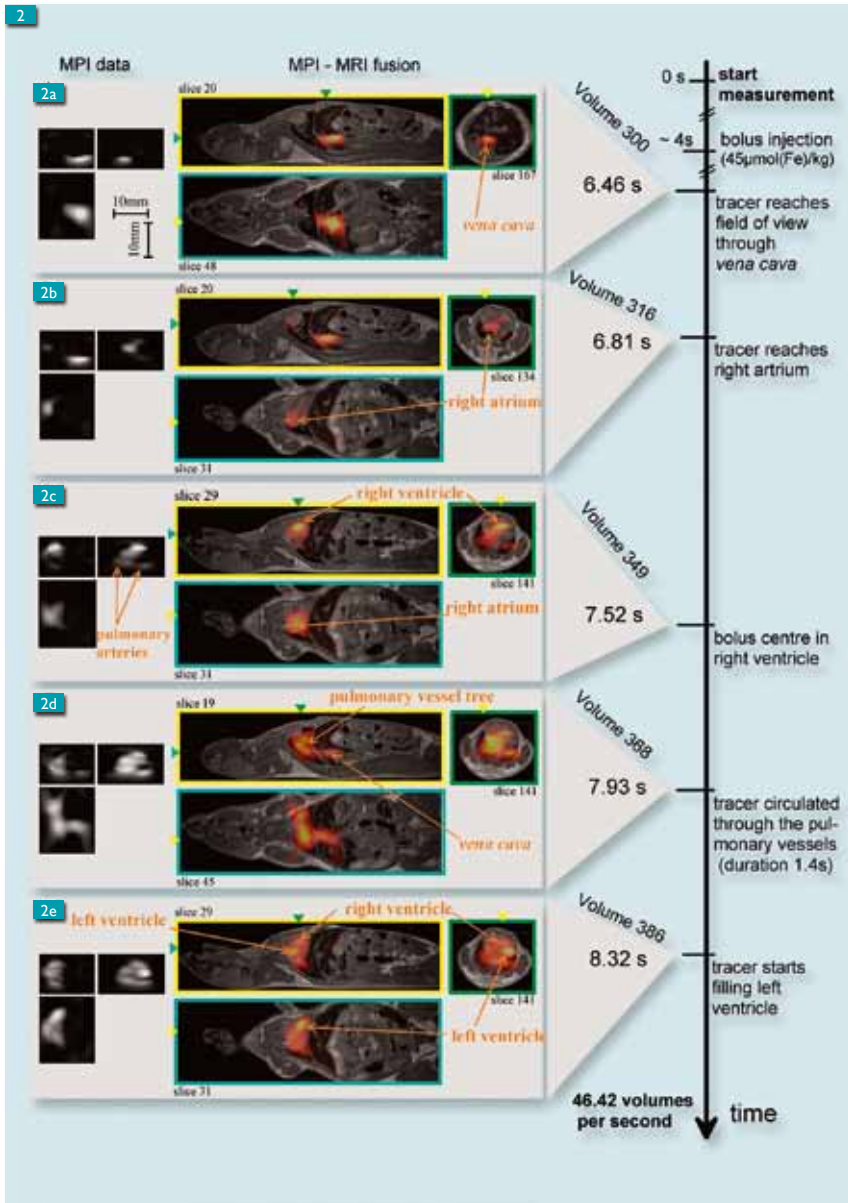


Figure 2. Dynamic MPI images (left) fused with static MRI images (acquisition time 23 min) in orthogonal views at selected points in time. The MPI video acquisition (21.5 ms per volume) was started before injecting the tracer (Resovist®) into the tail vein. The colored triangle in the color frame indicates the position of the orthogonal slice in the image framed in the corresponding color. The position of the slices in the MRI volume is also given by the three numbers at the corners of the frames and is not always kept constant between the different images. The time axis on the right side describes the successive phases of the bolus passage. The spatial and temporal resolution enables resolution and identification of all heart chambers as well as parts of the vessel tree.

magnetic field gradient, respectively. This gradient strength is achieved in the vertical direction in the yellow-framed images in Figure 2.

The scanner uses three sets of drive field coils to enable three-dimensional imaging. The drive field  $H_D$  with amplitude  $18m T\mu_0^{-1}$  in the vertical direction is produced by the selection field coils. The drive fields in the two orthogonal directions are produced by dedicated coils, which are driven at the same amplitude.

The three drive field frequencies are chosen to move the FFP along a three-dimensional Lissajous trajectory. Frequencies for the three directions are  
 $2.5 \text{ MHz}/99 \approx 25.25 \text{ kHz}$ ,  
 $2.5 \text{ MHz}/96 \approx 26.04 \text{ kHz}$  and  
 $2.5 \text{ MHz}/102 \approx 24.51 \text{ kHz}$ , respectively.

The Lissajous trajectory has a repetition time of 21.5 ms, corresponding to encoding 46.42 volumes per second, and covers a volume of about  $20.4 \times 12 \times 16.8 \text{ mm}$ .

The size of the gaps in the Lissajous pattern was chosen to match the desired resolution of approximately 1 mm. Two saddle-type receive coil pairs are aligned approximately perpendicular to the bore. In the axial direction, the solenoid drive field coil is also used for receiving the signal.

A new receive amplifier concept was implemented to reduce noise by a frequency dependent factor of between 5 and 100. In an ideal scanner, receive-chain noise is only generated by current fluctuations in the patient. In reality, coil noise and receive-amplifier noise contribute to the noise level. MRI achieves patient-dominated noise, because the small signal bandwidth allows mitigation of the amplifier noise contribution by resonant matching.

This strategy fails in MPI, since the receive signal is distributed over a wide frequency range. To provide the essential noise reduction, we designed a liquid cooled J-FET based amplifier reaching an input noise voltage of  $80 \text{ pV}/\sqrt{\text{Hz}}$  (input capacity 1 nF) over the relevant frequency band from 50 kHz to 1 MHz. In addition, the noise voltage of the receiving coils alone is  $50 \text{ pV}/\sqrt{\text{Hz}}$  so the total noise is about  $100 \text{ pV}/\sqrt{\text{Hz}}$ . In the present set up, the noise contribution of the mouse is negligible due to its small size and the associated low coil loading [19].

Before starting the animal experiments, the system was first calibrated to secure a functioning system. It was measured on a grid of  $34 \times 20 \times 28$  with a voxel size of  $(0.6 \text{ mm}^3)$  using a small reference sample of undiluted (500 m mol (Fe)/l) Resovist® (Bayer Schering Pharma, Berlin). To a certain degree, the chosen voxel size is arbitrary, however, it should be smaller than the true resolution. That is determined by particle properties, selection field gradient strength, and the level of regularization used in image reconstruction [18].

In other words, in MPI, voxel size is not equivalent to image resolution. The reference sample was in the form of a cube with the

extensions exactly matching the voxel size of the grid. It was positioned and measured at all voxel positions of the grid. Positioning was performed using a robot (Flachbettanlage 1, Iselautomation KG, Eichenzell, Germany). The data acquisition time per grid point was 0.6 seconds. The total measurement time including robot motion and background measurement was about six hours.

For reconstruction, the functional  $\|GC^p - U^p\|^2 + \lambda \|C^p\|^2$  was minimized using a row relaxation method called algebraic reconstruction technique (ART) [20, 21]. Here, the matrix  $G$  represents the system function,  $U$  the measured mouse data,  $C$  the desired image, and  $\lambda$  a regularization parameter chosen to adjust the balance between signal-to-noise ratio (SNR) and resolution for best visual image impression. True image resolution depends on the regularization parameter and is usually lower than the voxel resolution.

The iterative reconstruction approach does not require the inversion or factorization of the huge 3D system function matrix and furthermore, allows for easy integration of reconstruction constraints into the iteration to account for *a priori* knowledge. This feature has been used to improve image quality by the exclusion of non-physical negative tracer concentrations in the image.

Image resolution and SNR are not completely homogeneous over the entire field of view (FOV) because of the physical constraint of having a different selection field gradient strength in at least one direction. In our case, the gradient in anterior-posterior (AP) direction (vertical direction in the yellow and green framed images in Figure 2) had twice the strength of the orthogonal gradients. In addition, the speed of the FFP motion is lower at the edges of the FOV, thereby stimulating only a weaker particle response. That leads to lower SNR and resolution in these regions, and a signal fade-out right at the rim.

The series of *in vivo* experiments comprised scans on 18 mice using different concentrations of Resovist® [8]. Ten of the experiments were conducted with dosages low enough for human usage. The approximate range being between the standard dosage of 8  $\mu\text{mol (Fe)/kg}$  Resovist used in MRI scans, and a dosage of 45  $\mu\text{mol (Fe)/kg}$ , which is slightly above the safe dosage of 40  $\mu\text{mol (Fe)/kg}$  for human applications [22].

Each mouse (female NMRI out bred mice, Charles River Laboratories, Sulzfeld, Germany) was anesthetized with 120 mg/kg ketamine and 16 mg/kg xylazine. An insulin syringe (BD

Micro-Fine +, 0.5 ml) filled with 20  $\mu\text{l}$  diluted Resovist was introduced to the tail vein and attached to the tail. Resovist was diluted in physiological saline solution. To achieve a dosage of 45  $\mu\text{mol (Fe)/kg}$ , a 10% dilution was prepared for a 22.4 g mouse and to achieve a dosage of 10  $\mu\text{mol (Fe)/kg}$ , a 2.5% dilution was prepared for a 24.5 g mouse.

The mouse was then placed in supine position on a cylindrical animal support with an inner diameter of 29 mm so that the heart was within the FOV after insertion into the scanner bore. The raw data acquired after bolus injection were reconstructed to 1800 three-dimensional volumes.

To relate the MPI signal to the mouse anatomy, reference MR images of the selected mice were acquired after the MPI scans. The mice were carefully transferred from the MPI system to the dedicated MRI animal support to facilitate later image fusion. The MR scanner was a commercial 3.0T human whole-body scanner (Achieva, Philips Healthcare, the Netherlands) with a dedicated mouse coil insert for high SNR signal reception.

A standard T1-weighted turbo-spin-echo (TSE) sequence was applied to acquire sagittal multi-slice data. A FOV of 48 x 80 x 27 mm was covered with an in-plane resolution of 0.25 mm and a slice thickness of 0.50 mm. Total scan time amounted to 23 minutes.

After interpolating the MPI data to the MRI resolution, image overlays were made by manual rigid-body registration using three-dimensional translations according to different anatomical landmarks such as the vena cava and the heart chambers. In the overlay images, the MPI data are displayed using a color map with a color change from red to yellow to allow easy differentiation from the grayscale MRI data and to visualize a high dynamic range.

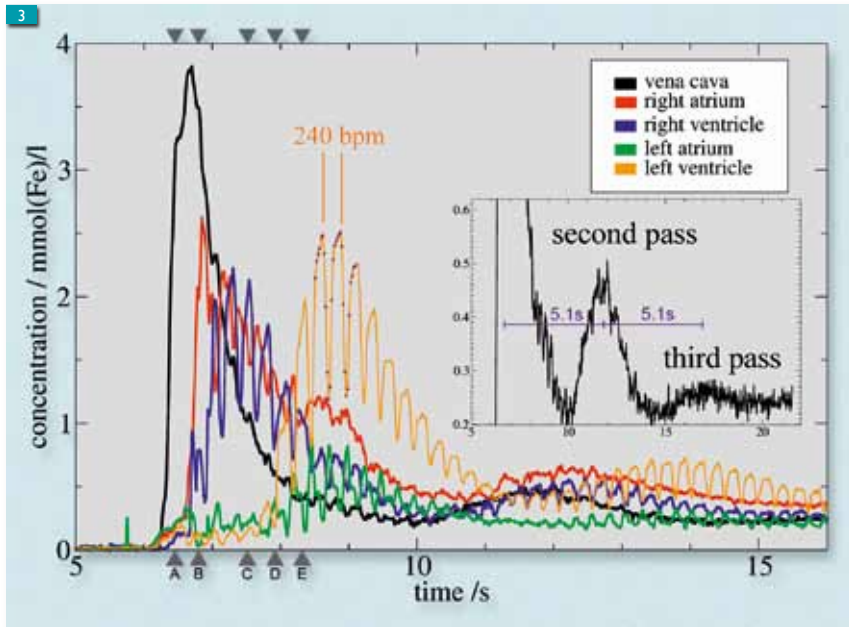
## Results

From the 18 exams, two representative results have been selected for presentation.

In Figure 2, the dynamic MPI data are displayed and compared to the static MRI data obtained with a dosage of 45  $\mu\text{mol (Fe)/kg}$  Resovist. Due to the high temporal resolution, no triggering or gating was necessary to compensate for motion. In Figure 2a, the bolus enters the FOV via the vena cava. Due to the anisotropic gradient strength described above, the MPI resolution in AP direction is better than in the orthogonal directions.

► **Ten of the 18 experiments were conducted with contrast dosages low enough for use in humans.**

► **The MPI scans were superimposed on MRI images.**



▲ Figure 3. Temporal dynamics of the tracer concentration at different locations in the vessel system for a dosage of 45  $\mu\text{mol (Fe)}/\text{kg Resovist}^{\circledR}$ . After injecting into the tail vein, the magnetic particles first arrive in the *vena cava*, then in the right atrium and then the right ventricle. As expected, the contractions of the atrium and the ventricle are out of phase. The blood needs about 1.4 seconds to pass through the pulmonary circulation before it is observed in the left atrium and the left ventricle. The apparent modulation of the concentration in synchronicity with the heartbeat is a partial volume effect, due to the small size of the mouse heart and the limited resolution of the system. The contractions of the atrium and the ventricle are out of phase, whereas the contractions of the left and right ventricle are in phase. A heart rate of 240 beats per minute is derived from the periodicity of the contractions. The small crosses on the curve of the left ventricle illustrate the sampling points. Finally, a second pass and a third pass through the body with a respective delay of about 5.1 seconds produces the shallow concentration peaks as seen in the inset. The spatial distribution of the concentration at times

Thus, in left-right direction, the MPI signal is not completely confined to the *vena cava* visible in the MR image. In Figure 2b, the tracer just reaches the right atrium. It can be deduced that the *vena cava* crosses different sagittal slices to end up at the atrium. The right ventricle fills with tracer just after the right atrium. Figure 2c displays the tracer concentration three heartbeats later. The right ventricle is clearly visible from the MPI data and matches the MRI data.

Moreover, the pulmonary arteries can be identified in the transversal slice of the MPI data. The intensity around these arteries increases over time (see Figure 2d), which can be attributed to the filling of the pulmonary veins. The small vessels in the lung contribute to an average signal. After passing the lung cycle, the tracer reaches the left heart chambers. The left ventricle can be identified clearly in Figure 2e.

In the transversal (green) and sagittal (yellow) slice of the MPI data, the left and right ventricle can be distinguished. Selected slices presented

in Figure 2 are also available online as a full video sequence at <http://stacks.iop.org/0031-9155/54/L1> showing the bolus passage.

To exploit the high temporal resolution of magnetic particle imaging, concentration dynamics at selected voxels (*vena cava*, right and left atrium, right and left ventricle) are presented in Figure 3. The bolus passage through the *vena cava* and the four heart chambers is reproduced by the time-shifted concentration maxima at the different positions. This supports the mapping of anatomical features presented in Figure 2.

From the time shift between the filling of the right and left heart-chambers, the pulmonary passage circulation time can be estimated to be about 1.4 seconds. An apparent modulation of the concentration can be observed at the heart chamber positions. The temporal onset, the modulation frequency and the opposite phase observed in the atria and the ventricles, show this corresponds to the heartbeat.

This can be attributed to a partial volume effect, due to the small size of the mouse heart and the limited resolution of the system. This creates an apparent concentration modulation, even when the real particle concentration within the heart chambers remains constant. The heart rate of the mouse can be determined from the apparent modulation to be about 240 beats per minute. That is low for a mouse, but can be expected for ketamine/xylazine anesthesia [23]. In addition, the concentration dynamics in the *vena cava* shows the second and third passage of the bolus, as displayed in the inset graph in Figure 3. The total time, which the tracer takes to pass through the whole circulatory system, is about 5.1 seconds.

The results of an experiment with a dosage of 10  $\mu\text{mol (Fe)}/\text{kg}$  are presented in Figure 4. All features discussed above can still be identified in these images, however with a higher artifact level than that observed for the 4.5 fold dosage.

## Discussion

The MPI results presented here do not indicate a drop in tracer performance in the *in-vivo* situation. The data provide a spatial and temporal resolution sufficient for the identification of different structures in the beating mouse heart. For example, the left and right pulmonary arteries with a diameter of about 500  $\mu\text{m}$  [24] can be observed, albeit not fully resolved, and are considerably smaller than the smallest coronary arteries usually treated in humans.

While with better contrast agents, high resolution imaging with MPI is potentially feasible [18], it is difficult to assess the resolution achieved with the current agent in the *in-vivo* situation. As described above, resolution also depends on the level of regularization in the reconstructed image. From the comparison of the vena cava cross-section in the MR image and the MPI image, we estimate the achieved MPI resolution to be roughly 1.5 mm in AP direction and 3 mm in the orthogonal directions.

On the other hand, the vena cava is located close to the edge of the FOV, where, as described above, the resolution is reduced. At the center, we therefore expect a higher resolution of about 1 and 2 mm for the respective directions. A resolution on this order is also found in phantom experiments [7].

### Clinical potential

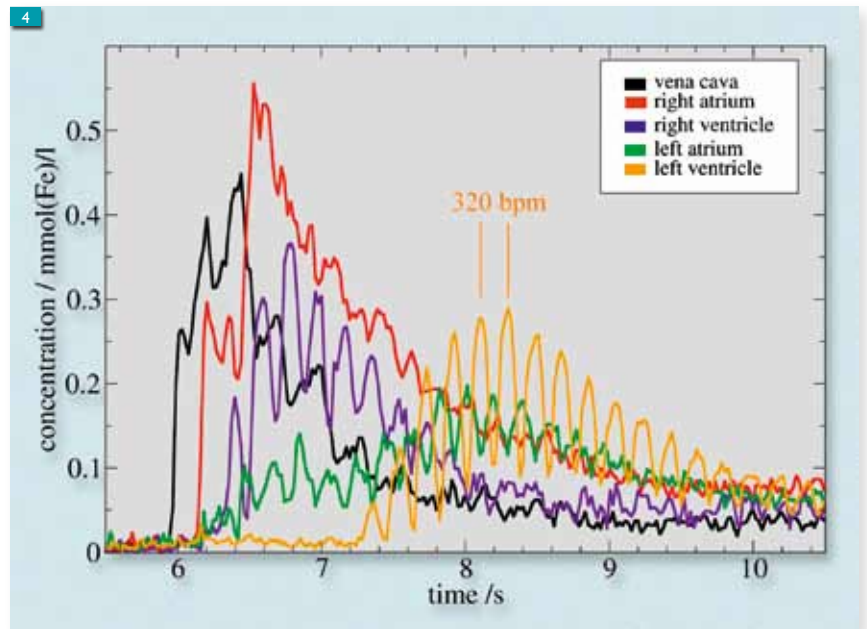
In the following, we try to assess the performance that could be expected of a human whole-body MPI scanner.

Scaling the system for human applications would increase the patient noise contribution. SNR estimations would have to noise contributions from the patient as well as those from the coil and amplifier. We estimate that with single-loop receive coils, due to the different scaling of noise contributions with size [25], amplifier noise would be dominant. With similar technology to that used in this study, SNR in the human-size system would be at around 10% of that reported here.

However, other amplifier designs (parametric amplifier, SQUID-based amplifier), cryogenic cooling of silicon J-FET amplifiers, or modified tuning could lower the amplifier noise contribution to the level of the patient noise contribution.

To compare the mouse scanner with a hypothetical improved human-size system, we have to compare the respective ratio between coil sensitivity and noise voltage at a given bandwidth.

With the current system, noise voltage as stated above is about 100 pV/ $\sqrt{\text{Hz}}$ , while receive coil sensitivity at the isocenter is about 150  $\mu\text{T}/\text{A}$  (24-loop coil, split into two circular coils with mean diameter of 18 mm and coil separation 36 mm). In a patient-noise limited human-size scanner, as described in a previous simulation study [18], patient noise voltage would be 1.8 pV/ $\sqrt{\text{Hz}}$  (at 1 MHz) and coil sensitivities would be 1.4  $\mu\text{T}/\text{A}$  (single-loop rectangular receive coil (10 x 10 cm) at 10 cm depth).



▲ Figure 4. Temporal dynamics of the tracer concentration at different locations in the vessel system for a dosage of 10  $\mu\text{mol}$  (Fe)/kg Resovist®. Following injection into the tail vein, the magnetic particles first arrive in the vena cava, then in the right atrium and the right ventricle. As expected, the contractions of the atrium and the ventricle are out of phase. The blood needs about 1.2 seconds to pass through the pulmonary circulation, after which it is seen in the left atrium and the left ventricle. The contractions of the atrium and the ventricle are again out of phase, whereas the contractions of the left and right ventricle are in phase. A heart rate of 320 beats per minute is derived from the periodicity of the contractions.

If the same particle concentration is imaged at an identical resolution using a comparable scanning sequence, SNR scales proportional to this ratio, that is for the human-size system; the expected SNR would be 52% of the SNR found in the present system. Further room for improvement exists in the tracer material, the encoding sequences, and reconstruction algorithms, potentially summing up to a factor of more than 100 [2, 3, 26].

The selection field strength of 5.5  $\text{T}\mu_0^{-1}\text{m}^{-1}$  can also be achieved over a large FOV. However, without expensive superconductors, only about 3  $\text{T}\mu_0^{-1}\text{m}^{-1}$  might be feasible. Resolution with this selection field strength would probably be slightly too low for direct assessment of the diameters of the relevant human coronary arteries. But by using the ability to quantify particle concentration (and therefore indirectly, blood volume) and the dynamic information, it should be possible to detect stenosis. On the other hand, as described above, technical improvements still offer the potential for substantially higher resolution.

Regarding patient heating, the chosen combination of drive field amplitude and frequency may be feasible. Wust et al. [27] reported that at the fourfold frequency, an amplitude of about 10 mT

is applicable to humans, corresponding to fourfold patient heating when compared with our parameters. Heating increases with the square of the frequency and the square of the drive field amplitude [19]. In the cited publication, Wust et al. [27] reported no peripheral nerve stimulation.

However, further research is required to find a drive field frequency, amplitude, and spatial distribution that would minimize the risk of stimulation. Moreover, for coronary imaging, the drive fields need to be applied for only a few seconds, allowing an increase in drive field frequency, improving the already excellent temporal resolution even further.

To cover the whole heart, an additional field similar to the drive field but at a lower frequency (less than 100 Hz) can be applied. This “focus field” can move the volume covered by the drive fields to any volume of interest. This patching method has the additional advantage that the encoding speed of the sub-volumes is unchanged, which minimizes motion artifacts within each sub-volume. From these considerations, we infer that a human scanner can be realized without significant loss in speed and resolution.

An additional potential for improving MPI can result from optimized FFP trajectories, more efficient reconstruction approaches, and improved tracer material. For the sake of technical simplicity, we used a Lissajous trajectory for the FFP motion. However, more sophisticated trajectories may be possible to improve the signal quality as discussed in [26]. Additionally, more *a priori* knowledge about the object can be used

in the reconstruction to improve image quality and speed, as it is already done in MRI [5, 6] and CT [28].

The highest potential, however, can be found in the tracer material. As already shown [2, 3], the fraction of the magnetic particles contributing to the MPI signal in Resovist® is only a few percent. Thus, the applied concentration might be lowered by at least one order of magnitude, if an adequate separation technique can be found. New approaches for particle synthesis may even improve tracer response determined by the slope of the tracer magnetization curve, allowing for lower selection field strengths and an increased spatial coverage, therefore resulting in a higher imaging speed.

To conclude, this report showed that magnetic particle imaging could image a beating mouse heart with high temporal and spatial resolution, using a commercially available MRI tracer material at clinically tolerable dosages. The results show that as a new imaging modality, MPI is capable of *in-vivo* imaging and therefore has the potential to become a clinically adopted imaging modality.

## Acknowledgments

The authors thank Dr. Bastian Tiemann and Dr. Andreas Hämisch, of the University Medical Center Hamburg-Eppendorf, for their support in carrying out the animal experiments. This work was financially supported by the German Federal Ministry of Education and Research (BMBF) under the grant number FKZ 13N9079 ■

## References

- [1] Weizenecker J, Gleich B, Rahmer J, Dahnke H, Borgert J. *Letter to the Editor: Three-Dimensional Real-Time In Vivo Magnetic Particle Imaging*. Phys Med Biol. 2009; 54: L1-L10.
- [2] Gleich B, Weizenecker J. *Tomographic Imaging using the Nonlinear Response of Magnetic Particles*. Nature. 2005; 435: 1214-1217.
- [3] Gleich B, Borgert J, Weizenecker J. *Magnetic Particle Imaging (MPI)*. Medicamundi. 2006; 50(1): 66-71.
- [4] Lauterbur PC. *Image Formation by Induced Local Interactions: Examples Employing Nuclear Magnetic Resonance*. Nature. 1973; 242: 190-191.
- [5] Tsao J, Boesiger P, Pruessmann KP. *k-t BLAST and k-t SENSE: Dynamic MRI with Frame Rate Exploiting Spatiotemporal Correlations*. Magn Reson Med. 2003; 50: 1031-1042.
- [6] Mistretta CA, Wieben O, Velkina J, Block W, Perry J, Wu Y, et al. *Highly Constrained Backprojection for Time-Resolved MRI*. Magn Reson Med. 2006; 55: 30-40.
- [7] Gleich B, Weizenecker J, Borgert J. *Experimental Results on Fast 2D-Encoded Magnetic Particle Imaging*. Phys. Med. Biol. 2008; 53: N81-N84.
- [8] Lawaczek R, Bauer H, Frenzel T, Hasegawa M, Ito Y, Kito K, et al. *Magnetic Iron Oxide Particles Coated with Carboxydextran for Parenteral Administration and Liver Contrasting*. Pre-clinical Profile of SH U555A. Acta Radiol. 1997; 38: 584-597.

- [9] Schmitt R, Froehner S, Brunn J, et al. *Congenital Anomalies of the Coronary Arteries: Imaging with Contrast-Enhanced, Multidetector Computed Tomography*. Eur Radiol. 1973; 46: 1016-1022. 2005; 15(6): 1110-1121.
- [10] TEC Assessment: *Contrast-Enhanced Cardiac Computed Tomography Angiography for Coronary Artery Evaluation*. BlueCross and BlueShield Association Technology Evaluation. May 2005.
- [11] Nienhuis MB, Ottervanger JP, Bilo HJG, Dikkeschei BD, Zijlstra F. *Prognostic Value of Troponin after Elective Percutaneous Coronary Intervention: A Meta-Analysis*. Catheter Cardiovasc Interv. 2008; 71(3), 318-324.
- [12] Kuhl DE, Edwards RG. *Image Separation Radioisotope Scanning*. Radiology 1963; 80: 653-661.
- [13] Chesler DA, Hoop B Jr, Brownell G.L. *Transverse Section Imaging of Myocardium with  $^{13}\text{NH}_4$* . J. Nucl. Med. 1973; 14: 623.
- [14] Ter-Pogossian MM, Phelps ME, Hoffman EJ, Muullani NA. *A Positron Emission Transaxial Tomography for Nuclear Medicine Imaging (PETT)*. Radiology. 1975; 114: 89-98.
- [15] Fayad ZA, Fuster V. *Clinical Imaging of the High-Risk or Vulnerable Atherosclerotic Plaque*. Circulation Research. 2001; 89: 305-316.
- [16] Saxena V, Gonzales-Gomez I, Laug WE. *A Noninvasive Multimodal Technique to Monitor Brain Tumor Vascularization*. Phys Med Biol. 2007; 52, 5295-5308.
- [17] Luciani A, Itti E, Rahmouni A, Meignan M, Clement O. *Lymph Node Imaging: Basic Principles*. Eur J Radiol. 2006; 58, 338-344.
- [18] Weizenecker J, Borgert J, Gleich B. *A Simulation Study on the Resolution and Sensitivity of Magnetic Particle Imaging*. Phys. Med. Biol. 2007, 52 (21): 6363-6374.
- [19] Vlaardingerbroek MT, den Boer JA. *Magnetic Resonance Imaging*. Springer. 2003.
- [20] Kaczmarz S. *Angenäherte Auflösung von Systemen Linearer Gleichungen*. Bull. Acad. Polon. Sci. Lett. A. 1937; 35: 355-357.
- [21] Dax A. *On Row Relaxation Methods for Large Constrained Least Square Problems*. SISC. 1993; 13(3): 570-584.
- [22] *Patient Information Leaflet for Resovist*. Schering AG. April 2004.
- [23] Janssen BJ, De Celle T, Debets JJ, Brouns AE, Callahan MF, Smith TL. *Effects of Anesthetics on Systemic Hemodynamics in Mice*. Am. J. Physiol. Heart. Circ. Physiol. 2004; 287(4) 1618-1624.
- [24] Chesler NC, Thompson-Figueroa J, Millburne K. *Measurement of Mouse Pulmonary Artery Biomechanics*. J. Biomech Eng. 2004; 126(2): 309-313.
- [25] Wang J, Reykowski A, Dickas J. *Calculation of the Signal-to-Noise Ratio for Simple Surface Coils and Arrays of Coils*. IEEE Trans. Biomed. Eng. 1995; 42(9): 908-917.
- [26] Weizenecker J, Gleich B, Borgert J. *Magnetic Particle Imaging using a Field Free Line*. J. Phys. D: Appl. Phys. 2008; 41(10): 105009.
- [27] Wust P, Gneveckow U, Johannsen M, Böhmer D, Henkel T, Kahmann E, et al. *Magnetic Nanoparticles for Interstitial Thermoablation – Feasibility, Tolerance and Achieved Temperatures*. Int. J. Hyperthermia. 2006; 22(8): 673-685.
- [28] Li M, Kudo H, Hu J, Johnson RH. *Improved Iterative Algorithm for Sparse Object Reconstruction and its Performance Evaluation with Micro-CT Data*. IEEE Trans. Nucl. Sci. 2004; 51(3): 659-666.

# 3D multimodality roadmapping in interventional neuroradiology

T. Andersson  
M. Söderman

Karolinska University Hospital, Department of Neuroradiology, Stockholm, Sweden.

D. Ruijters  
D. Babic  
R. Homan  
P. Mielekamp

Philips Healthcare, Best, the Netherlands.

► **A fused image allows better anatomical understanding and, consequently, more precise navigation.**

During minimally invasive neurovascular interventions, the fluoroscopic images with the live information on interventional endovascular devices, and pre-operative soft-tissue images (such as magnetic resonance (MR) or computed tomography (CT)), are usually shown on separate displays. This means that the interventionist has to perform a mental projection of the position of the endovascular device on to the soft-tissue data.

This article describes a method for fusing this information into a combined image, which may be of great clinical advantage, since it relieves the operator of performing this task during the intervention. Furthermore, a fused image allows a better anatomical understanding and, consequently, more precise navigation of the endovascular devices.

► **The machine-based method provides accurate real-time registration even when there are few landmarks.**

To provide the maximum benefit of such an augmented image, the live fluoroscopy data and the soft-tissue data have to be combined in real time, with minimum latency and an adequate frame rate (15 or 30 frames per second, depending on acquisition mode). The usage of the fused display during interventional treatment also requires the image to be easy to interpret, while manipulation should be interactive and simple to use. This article describes the steps that are necessary to achieve such a combined visualization [1] and discusses the clinical benefits.

Registration is the process of spatially aligning two image datasets (which may originate from different modalities), such that the corresponding morphology in both datasets overlaps. Two fundamentally different approaches can be distinguished when registering 2D fluoroscopy data to 3D volumetric data.

In the first approach, called image-based registration, the registration process is driven by the image content. There are a number of image-based 2D-3D registration algorithms

known in the literature for registering fluoroscopy images to either CT or MR images [2-7]. These algorithms, however, take a considerable amount of time to compute. Further, they need sufficient anatomical landmarks to be present in the 2D fluoroscopy image, which is not necessarily always the case.

The second approach is known as machine-based registration. With the introduction of motorized calibrated C-arm X-ray angiography, 3D reconstruction of the vasculature came within reach. Since 3D rotational angiography (3DRA) datasets are obtained with the same apparatus as the 2D fluoroscopy data, it is possible to calculate a registration, based on the state of the geometry (viewing incidence angles, source-to-detector distance, etc.) and calibration data. This, of course, assumes that there was no patient motion between acquisition of the 3DRA data and the fluoroscopy data [8-10].

This method also allows for obtaining a registration when there are insufficient landmarks present in the images (for example, due to the absence of iodinated contrast medium in the fluoroscopy images) [11]. A further advantage of machine-based registration is the fact that it can be computed in real time.

## Methods and materials

### Pre-processing steps

Before the treatment of neurovascular pathologies, soft-tissue data, such as MR or CT images, are often acquired for diagnostic purposes and/or treatment planning. The goal is to integrate the data into a fused visualization during the treatment. To achieve this objective, a 3DRA dataset is obtained at the beginning of the intervention. Before the 3DRA and soft-tissue data can be fused with the live fluoroscopy image stream, a pre-processing step has to be performed. In this step, the 3DRA

and soft-tissue dataset are registered, using an image-based registration algorithm.

Performing image registration of large 3D datasets during an interventional treatment poses a number of constraints on the registration method. In particular, the calculation time of the algorithm has to be limited, since it has to be carried out during the intervention. Since the implementation used is optimized to efficiently use the workstation's graphics hardware, it can perform the registration process within a mere eight seconds.

3DRA reconstructions may have a very high spatial resolution (a voxel can be as small as 0.15 mm), but tend to be rather noisy in the dynamic range. Therefore, the vessels, bones and intracranial sinuses are the only anatomical structures that are clearly visible and can serve as landmarks. It is therefore important that these structures are contained within the 3DRA reconstruction as well as in the soft-tissue data.

Since the focus is on cerebral applications and there are only limited local deformations of the anatomical structures within the head, a rigid registration can be used (that is, only a global translation and rotation). Rigid registration has the further property that it can be calculated relatively robustly and fast. Mutual information is used to drive the rigid registration [12], because it performs very well on intermodality registration and does not demand any *a priori* knowledge of the datasets. Optionally, the image-based registration is preceded by a rough manual registration.

A further pre-processing step forms the segmentation of the vessel tree in the 3DRA dataset. This is a moderately easy task since the iodinated contrast medium has a higher X-ray absorption than any other substance present in the dataset, and therefore the vessel structure can be rather easily distinguished from the surrounding tissues. Note that the entire pre-processing only has to be performed once, at the beginning of the intervention.

#### Registering 2D fluoroscopy to 3DRA data

The machine-based registration involves projecting the 3DRA data on to the fluoroscopy images, based on the position of the C-arm. The X-ray C-arm system can rotate over three axes (Figure 1a): rotation around the L-arm, propeller movement of the C-arm, and roll movement of the C-arm. The 3DRA dataset has to be rotated to match the orientation of the C-arm system.

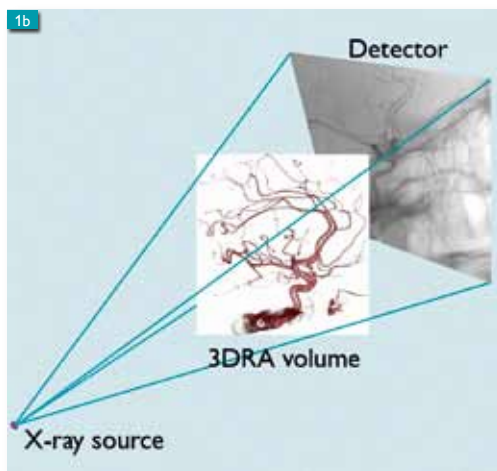
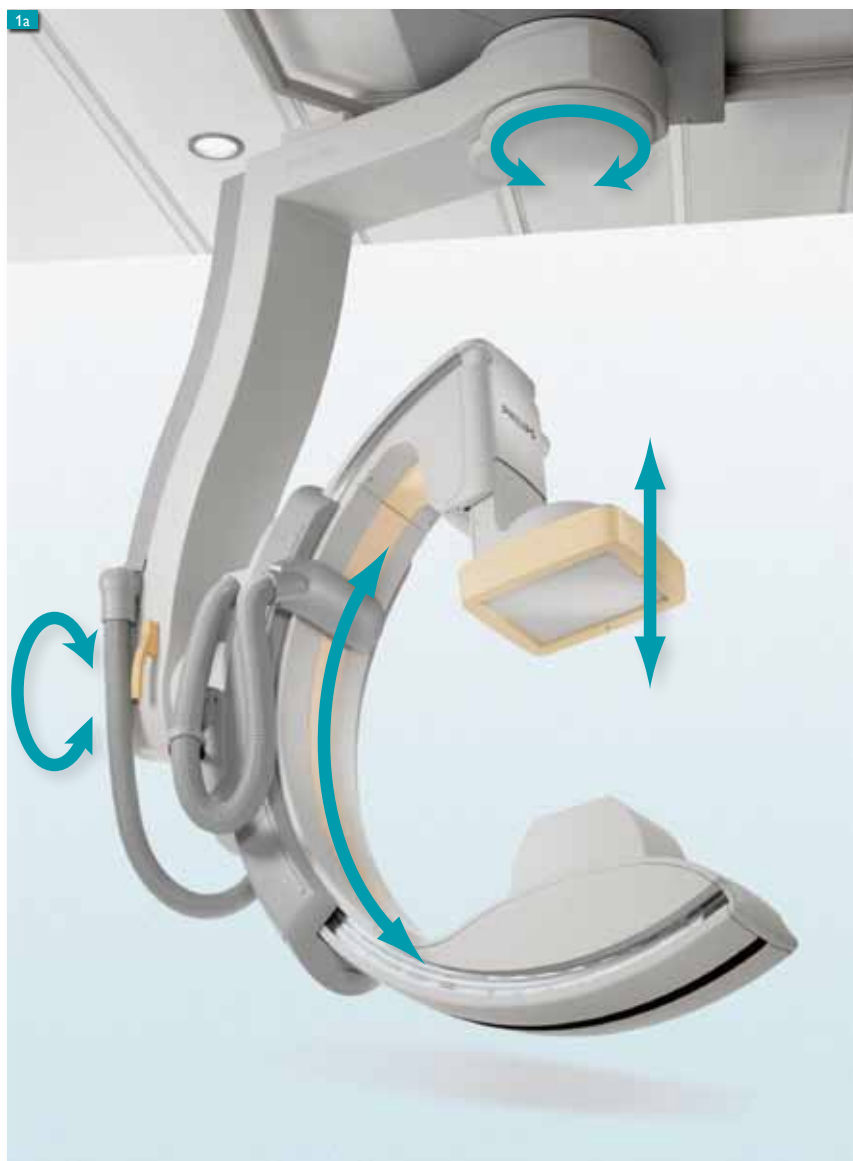


Figure 1. Registering 2D fluoroscopy to 3DRA data. The 3DRA dataset has to be rotated to match the orientation of the C-arm system.

▲  
Figure 1a. The degrees of freedom of the C-arm geometry.

◀  
Figure 1b. The virtual projection of a 3DRA dataset on a fluoroscopy image.

Rotation of the 3DRA dataset has to be further corrected for deviations from the ideal calculated orientation based on the calibration data [13, 14]. The calibration procedure only needs to be performed approximately once every six months. After the rotation of the 3DRA dataset into the appropriate orientation, there

still remains the task of projecting it with the proper perspective (Figure 1b). The perspective depends on the X-ray source-to-detector distance and the detector dimensions.

The 2D-3D correspondence between the 3DRA dataset and the fluoroscopy image can be calculated in a mere 1.5 microseconds, and thus can be done in real time. The accuracy of the calibrated machine-based 2D-3D registration was measured on five Philips Allura FD20 C-arm X-ray angiography systems. The registration was least accurate at the corners of the 3DRA reconstruction volume. The maximal deviation of the 2D fluoroscopy image and the projected 3DRA image was 0.4 mm at the corners of the reconstruction volume. The average deviation at the corners was 0.2 mm.

### Fused visualization

The visualization should unite the soft-tissue data, the 3DRA data, and the live fluoroscopy stream into a single fused image (Figure 2). It should be possible to interpret such a fused image quickly and easily during the intervention. It is therefore mandatory to combine the large amount of information in a way that is easy to digest and that conveys all the relevant information.

The fluoroscopy data that overlays the background can contain some anatomical landmarks, relevant to the physician. The most important part of the fluoroscopy image, though, is the area inside the vessels, since this is where the endovascular devices are moved. The 3DRA dataset provides a high-resolution 3D representation of the relevant vessel structures. The fluoroscopy image stream, containing the real-time status of the endovascular devices, is mapped onto the 3D vasculature.

In the combined visualization, the part of the fluoroscopy image that is not projected on top of the 3D vasculature can be suppressed, since its content makes a less significant contribution to the final image. The endovascular devices are located within the region that coincides with the 3D vessel structures, and therefore this region of the fluoroscopy image can be additionally enhanced.

The morphological MR or CT dataset holds the soft-tissue structures relevant to the procedure as well as some pathological processes that may not be visible in the 3DRA or fluoroscopy data (Figure 2a). The most relevant parts of the soft-tissue data can be visualized by choosing a slab (Figure 2d), whose location, orientation and thickness can be interactively altered by the operator at any time.

Alternatively, it is possible to select a representation of the soft-tissue data, whereby an octant, quarter, or half is cut open (Figure 3). The location and orientation of the intersection can be interactively changed. The 2D-3D registration, which was calculated in the first pre-processing step, is applied to the position of the soft-tissue data.

## Discussion

Being able to see the live fluoroscopy image within the context of the 3D vasculature and soft-tissue information is of great clinical relevance. The combination of the fluoroscopy image with the 3DRA vessel tree gives added value. This is because the guide wire and catheter positions can be located with respect to the vessel tree without additional contrast injection (Figure 2b, c). In the meantime, the C-arm position and the X-ray source-to-detector distance can be altered freely. Even during rotations of the C-arm, the machine-based 2D-3D registration will always be up to date.

The clinical interest in the so-called 3D-roadmapping has been described before [9]. The additional visualization of the soft-tissue data allows correlating the position of the guide wire and catheter to anatomical information and pathologies, which are only visible in the soft-tissue data. That this information is available in real time is the fact that makes it especially suitable for navigation.

The addition of soft-tissue visualization to the 3D-roadmapping technique, and especially high-quality MR datasets, brings extra information that may be important for the operator's decision making, and can increase safety during the procedure as well as shorten the operating time. In embolizations of brain arteriovenous malformations (b-AVMs) or intracranial tumors using liquid adhesives or particles, the exact position of the catheter tip is crucial.

The obvious goal is to embolize the pathological structures and avoid spilling over to normal vessels supplying normal brain tissue. In these situations, the complex vessel anatomy can be difficult to comprehend. In such instances, the 3D multimodality roadmapping may prove to be of great value, especially since it is possible to freely rotate the 3D volume with controls located at the interventional table.

The technique may also be of great assistance for targeting areas of a b-AVM that are to be partially embolized, thereby avoiding so-called

► **Seeing the live fluoro image in the context of the 3D vasculature and soft tissue is of great clinical relevance.**

► **Multimodality roadmapping may prove to be of great value in embolizations, where the position of the catheter tip is critical.**



◀◀  
Figure 2a. An MR image, showing an AVM and impacted brain tissue.



◀  
Figure 2b. The live fluoroscopy image without contrast agent shows the guide wire, but does not reveal its relation to the vasculature and the soft tissue.



◀◀  
Figure 2c. The fluoroscopy image mixed with the vessel tree from the 3DRA dataset adds the vascular context to the live data.



◀  
Figure 2d. The fluoroscopy image, the 3DRA vasculature and a slab from the MR data. The MR slab is positioned parallel to the view port at the guide wire tip.

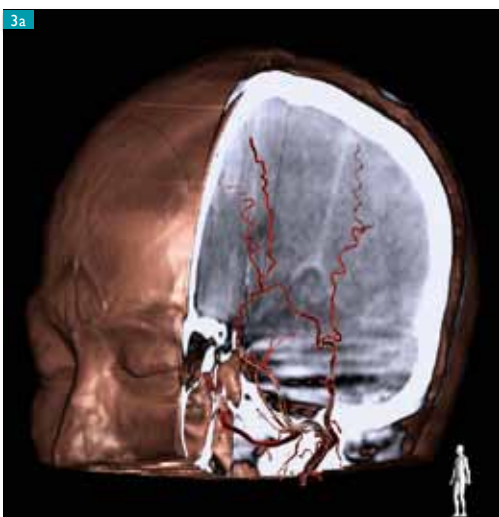
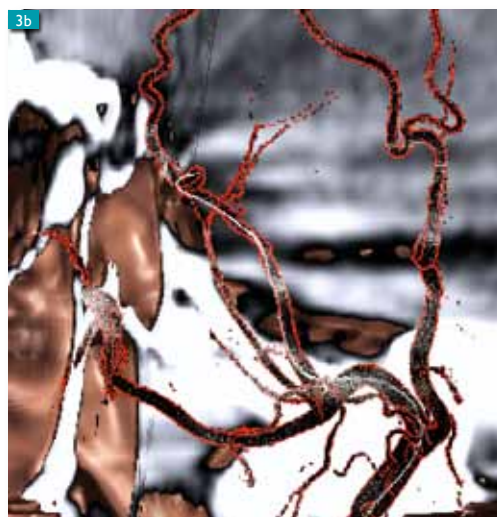


Figure 3. The soft-tissue dataset can be combined with the 3DRA data and displayed with an octant, quarter, or half cut open.



◀◀  
Figure 3a. A quarter is cut out of a soft-tissue dataset, while the 3DRA vessels are overlaid with the live fluoroscopy information.

◀  
Figure 3b. A zoomed fragment of the left image, showing the micro guide wire.

piece-meal embolization, as well as for avoiding high-risk treatment close to eloquent areas of the brain. The exact position for delivery may also be important for intra-arterial delivery of other compounds, such as cytostatic agents for tumors, growth factors for stroke and degenerative brain disorders. This is a rapidly developing and growing field of application.

## Conclusions

This article presents a method of fusing real-time fluoroscopy, 3DRA data and soft-tissue data into a combined image, and its application in neuro-endovascular procedures. The combination of the fluoroscopic image with the 3DRA vessel tree, known as 3D-roadmapping, offers the

advantage that the spatial relationship between the endovascular device and the surrounding vessel morphology can be determined without additional contrast injection, while the position of the C-arm geometry can be altered freely.

The steps necessary to achieve this data fusion are described. A fast automatic image-based registration of the 3DRA dataset and the soft-tissue dataset had to be developed in order to bring the pre-operative data in the coordinate frame of the C-arm equipment. The machine-based registration between the 2D fluoroscopy image and the 3DRA data only depends on the

incidence angles, the X-ray source-to-detector distance and the calibration data [1]. It can be easily calculated in real time. Possible clinical applications are identified, and the ways in which the presented method could be employed in those applications are demonstrated.

The strength of the described approach lies in its real-time nature, which is primarily achieved by the on-the-fly 2D-3D registration, and the fast fused visualization. The interactive real-time aspect contributes to the 3D perception of the anatomy and pathologies during an intervention ■

► **Interactive real-time registration contributes to the 3D perception of the anatomy during an intervention.**

## References:

- [1] Ruijters D, Babic D, Homan R, Mielekamp P, ter Haar Romeny BM, Suetens P. *3D Multi-Modality Roadmapping in Neuroangiography*. SPIE Medical Imaging: Visualization and Image-Guided procedures. 2007; 6509: 65091F.
- [2] Weese J, Penney GP, Desmedt P, Buzug TM, Hill DLG, Hawkes DJ. *Voxel-based 2-D/3-D Registration of Fluoroscopy Images and CT Scans for Image-Guided Surgery*. IEEE Trans. Information in Biomedicine. 1997; 1(4): 284-293.
- [3] Liu A, Bullit E, Pizer SM. *3D/2D Registration via Skeletal Near Projective Invariance in Tubular Objects*. MICCAI'98 Oct 11-13, MIT, Cambridge, MA, USA. 1998; 952-963.
- [4] Penney GP, Batchelor PG, Hill DLG, Hawkes DJ, Weese J. *Validation of a Two- to Three-Dimensional Registration Algorithm for Aligning Preoperative CT Images and Intraoperative Fluoroscopy Images*. Med. Phys. 2001; 28(6): 1024-1031.
- [5] Van de Kraats EB, Penney GP, Tomažević D, Van Walsum T, Niessen WJ. *Standardized Evaluation of 2D-3D Registration*. MICCAI'04 Sept. 26-30, St. Malo, France. 2004: 574-581.
- [6] Tomažević D, Likar B, Pernuš F. *3-D/2-D Registration by Integrating 2-D Information in 3-D*. IEEE Trans. Medical Imaging. 2006; 25(1): 17-27.
- [7] Zheng G, Zhang X, Nolte LP. *A Class of Novel Point Similarity Measures based on MAP-MRF Framework for 2D-3D Registration of X-Ray Fluoroscopy to CT Images*. ISBI'06 April 6-9, Arlington, VA, USA. 2006: 438-441.
- [8] Maintz JBA, Viergever MA. *A Survey of Medical Image Registration*. Medical Image Analysis. 1998; 2(1): 1-36.
- [9] Söderman M, Babic D, Homan R, Andersson T. *3D Roadmap in Neuroangiography: Technique and Clinical Interest*. Neuroradiology. 2005; (47): 735-740.
- [10] Gorges S, Kerrien E, Berger MO, Troussel Y, Pescatore J, Anxionnat R, Picard L. *Model of a Vascular C-Arm for 3D Augmented Fluoroscopy in Interventional Radiology*. MICCAI'05, Oct. 26-30, Palm Springs, CA, USA. 2005: 214-222.
- [11] Baert SAM, Penney GP, Van Walsum T, Niessen WJ. *Precalibration Versus 2D-3D Registration for 3D Guide Wire Display in Endovascular Interventions*. MICCAI'04 Sept. 26-30, St. Malo, France. 2004: 577-584.
- [12] Maes F, Collignon A, Vandermeulen D, Marchal G, Suetens P. *Multimodality Image Registration by Maximization of Mutual Information*. IEEE Trans. Medical Imaging. 1997; 16(2): 187-198.
- [13] Grass M, Koppe R, Klotz E, Proksa R, Kuhn MH, Aerts H, Op de Beek J, Kempkers R. *Three-Dimensional Reconstruction of High Contrast Objects using C-arm Image Intensifier Projection Data*. Computerized Medical Imaging and Graphics. 1999; 23(6): 311-313.
- [14] Gorges S, Kerrien E, Berger MO, Pescatore J, Troussel Y, Anxionnat R et al. *3D Augmented Fluoroscopy in Interventional Neuroradiology: Precision Assessment and First Evaluation on Clinical Cases*. MICCAI Workshop AMI-ARCS'06, 6 Oct, Copenhagen, Denmark. 2006.

### **Blood-brain barrier permeability: quantification with computed tomography and application in acute ischemic stroke**

*M. Wintermark, J. Hom, J. W. Dankbaar, J. Bredno and M. E. Olszewski*

Given the high costs – human and financial – associated with stroke and its aftermath, improvements to stroke treatment are of paramount importance. Recombinant tissue plasminogen activator (rt-TPA) has been shown to be effective in treating acute ischemic stroke; however, rt-TPA is currently only approved for use within a fixed time window, and it is associated with a non-negligible risk of hemorrhagic transformation. This article describes quantitative CT imaging of blood-brain barrier permeability that may enable a more widespread administration of rt-TPA in acute stroke by allowing risk-balanced, individualized treatment decisions that are based on physiology rather than time.

### **Clinical MR tractography: past, present, and future**

*K. Yamada, K. Akazawa, S. Yuen and T. Nishimura*

Diffusion tensor imaging (DTI)-based tractography was first introduced to the medical community a decade ago. Since then, it has become widely used in routine clinical practice in many different fields, including preoperative planning for brain tumors and vascular malformations. The technique elucidates the courses of the eloquent fiber tracts, such as the pyramidal tract, visual pathway, and arcuate fasciculus. Tractography was first introduced with the deterministic streamline technique. It has evolved to using complex probabilistic approaches. The latest techniques tend to require extended imaging and post-processing times. This brief review describes the past, present, and future of clinical tractography.

### **Clinical applications of diffusion tensor imaging in children**

*N.K. Rollins and J.M. Chia*

Diffusion tensor imaging (DTI), a relatively new addition to MR imaging, exploits the preferential movement of water protons within the brain along the axis of the axons. By mapping the anisotropic movement of protons, DTI shows the individual white matter tracts as discrete anatomical structures. The data can also be used to create 3D mathematical renderings of white matter, providing information about the micro-architecture of the white matter in the form of metrics, which provide information on axonal integrity and myelination. There are numerous applications of DTI in the pediatric brain from birth onwards, in normal and disease states.

### **Functional MRI of the sensorimotor system in newborns**

*H. Boecker, L. Scheef and A. Heep*

Neonatal functional MRI (fMRI) allows non-invasive *in vivo* mapping of dedicated brain circuits at the early stages of development. This article summarizes the current experience at the University Hospital in Bonn in establishing and optimizing fMRI studies using standardized passive sensorimotor stimulation tasks in infants at high risk of developing motor sequelae because of preterm birth.

### **7T MRI research in neurology: initial results and future research applications**

*A.G. Webb, M.J. Verluis, M.A. van Buchem, H.E. Kan, W.M. Teeuwisse, and M.J.P. van Osch*

Leiden University Medical Center established the C.J. Gorter Center for High Field Magnetic Resonance Imaging (MRI) within the Department of Radiology in late 2007. The center's aim is to develop new methods and protocols for high field clinical MRI in a variety of patient populations. This is done in parallel with performing studies of correlative disease models in animals. The center recently installed a Philips Achieva 7T whole-body MRI research system, one of only two in the Netherlands. This article summarizes progress in neurological applications during the first year of operation of the 7T scanner at Leiden.

### Dynamic whole-spine MRI of contortionists

W.W. Orrison, Jr and T. G. Perkins

A study of five female contortionists from a Mongolian circus school was conducted to assess pathological changes that might be associated with the dramatic twisting of the body into extreme positions.

All five participants were examined using a Philips Achieva 3T cylindrical MR imaging system, and additional whole-spine dynamic images were obtained in two of the participants using the Philips Panorama HFO 1T open MR system to define the range of motion achieved during extreme contortion.

Pathological changes observed included intervertebral disc bulges, osteophyte formation, and a total of four anterosuperior limbus fractures in three of the five participants.

### Molecular imaging in dementia: journey to the end of the night

V. L. Villemagne and G.J. O'Keefe

With the advent of new therapeutic strategies aimed at preventing or delaying functional and irreversible cognitive loss in dementia, there is increased interest in developing agents that allow the *in vivo* assessment of the pathophysiological mechanisms at play. Molecular imaging with target-specific ligands can support the early diagnosis of dementia and the evaluation of anti-dementia therapy by examining brain metabolism and neurotransmitter systems, as well as disease specific traits, such as  $\beta$ -amyloid in Alzheimer's disease. Recent developments in the field are reviewed to illustrate the utility of molecular imaging in the clinical management of dementia.

### Three-dimensional real-time *in vivo* magnetic particle imaging

J. Borgert, B. Gleich, J. Rahmer, H. Dahnke and J. Weizenecker

Magnetic particle imaging (MPI) is a new tomographic imaging method capable of imaging the local concentration of commercially available contrast agent with high spatial and temporal resolution. Until now, only static and dynamic 2D phantom experiments with high tracer concentrations have been demonstrated. This article presents the first *in vivo* 3D real-time MPI scans revealing details of a beating mouse heart using clinically approved concentrations of a commercially available MRI contrast agent. With these abilities, MPI has taken a huge step towards proving its feasibility for medical applications.

### 3D-multimodality roadmapping in interventional neuroradiology

T. Andersson, M. Söderman, D. Ruijters, D. Babic, R. Homan and P. Mielekamp.

During minimally invasive neurovascular interventions, live information on endovascular devices contained within two-dimensional (2D) fluoroscopic images, and three-dimensional soft-tissue images from sources such as MRI and CT, are usually shown on separate displays. The interventionist has to mentally project the position of the endovascular device on to the soft-tissue data. This article describes a method of fusing the information into one combined image. This reduces the interventionist's workload and allows better understanding of the anatomy with, consequently, more precise navigation. For maximum benefit, image fusion has to take place in real time with minimum latency and an adequate frame rate.

### Perméabilité de la barrière hémato-encéphalique: quantification par tomодensitométrie et application pour les AVC ischémiques aigus

*M. Wintermark, J. Hom, J. W. Dankbaar, J. Bredno et M. E. Olszewski*

Au vu des coûts élevés, à la fois humains et financiers, que représentent un accident vasculaire cérébral et ses conséquences, il semble essentiel d'en améliorer le traitement. L'efficacité de l'activateur tissulaire du plasminogène recombinant (rt-PA) a été démontrée pour le traitement des accidents vasculaires cérébraux ischémiques aigus; toutefois, l'utilisation du rt-PA n'est actuellement approuvée que pour un traitement sur une durée déterminée. Elle est également associée à un risque non négligeable de transformation hémorragique. Cet article porte sur l'imagerie TDM quantitative de la perméabilité de la barrière hémato-encéphalique, qui pourrait permettre une administration plus étendue du rt-PA lors d'AVC aigus. En effet, cette technique assure une prise de décision thérapeutique individualisée et prenant en compte les risques spécifiques, basée sur la physiologie du patient et non sur la durée du traitement.

### Tractographie clinique par IRM: passé, présent et avenir

*K. Yamada, K. Akazawa, S. Yuen et T. Nishimura*

La tractographie par imagerie de tenseur de diffusion (DTI) a été présentée pour la première fois à la communauté médicale il y a dix ans. Depuis, cette technique a été largement utilisée pour des examens cliniques de routine dans de nombreux domaines, notamment pour la planification préopératoire en cas de tumeurs cérébrales et de malformations vasculaires. Cette technique permet de déceler le parcours des faisceaux de fibres de zones éloquentes, notamment le faisceau pyramidal, les voies optiques et le faisceau arqué. Elle a d'abord été introduite comme méthode déterministe, puis s'est développée pour utiliser des approches probabilistes plus élaborées. Les dernières techniques nécessitent souvent des capacités d'imagerie et de post-traitement étendues. Ce court article synthétise le passé, le présent et l'avenir de la tractographie clinique.

### Applications cliniques de l'imagerie de tenseur de diffusion pour les examens pédiatriques

*N.K. Rollins et J.M. Chia*

Technique relativement récente en IRM, l'imagerie de tenseur de diffusion (DTI) utilise les mouvements préférentiels des protons aqueux dans le cerveau, le long des axones. Repérant les mouvements anisotropes des protons, l'imagerie de tenseur de diffusion permet de visualiser individuellement les faisceaux de la substance blanche sous forme de structures anatomiques distinctes. Les informations des données de tenseur de diffusion permettent de créer des rendus mathématiques 3D de la substance blanche. L'imagerie de tenseur de diffusion permet d'examiner la micro-architecture de la substance blanche sous forme de données chiffrées renseignant sur l'intégrité axonale et la myélinisation. Les applications de l'imagerie de tenseur de diffusion pour les examens cérébraux chez l'enfant sont très nombreuses, et ce dès la naissance, qu'il présente un état normal ou un état pathologique.

### IRM fonctionnelle du système sensori-moteur chez les nouveau-nés

*H. Boecker, L. Scheef et A. Heep*

L'imagerie néonatale par IRM fonctionnelle permet de cartographier *in vivo* et de façon non invasive certains circuits cérébraux lors des premières phases de développement. Cet article résume l'expérience en cours à l'hôpital universitaire de Bonn, visant à établir et optimiser ce type d'examens à l'aide de tâches standardisées de stimulation sensori-motrice passive chez les nourrissons prématurés présentant des risques élevés de développer des troubles moteurs.

### IRM 7T en neurologie: premiers résultats et applications futures

*A.G. Webb, M.J. Versluis, M.A. van Buchem, H.E. Kan, W.M. Teeuwisse, et M.J.P. van Osch*

Fin 2007, le centre médical universitaire de Leiden a créé le centre C.J. Gorter d'imagerie à résonance magnétique (IRM) à haut champ, au sein du service de radiologie. Ce centre a pour but de développer de nouveaux protocoles et méthodes d'IRM clinique à haut champ s'appliquant à de nombreuses catégories de patients. Parallèlement à ce développement, des études de maladies corrélatives sont réalisées sur des animaux. Le centre a récemment installé un système IRM Philips Achieva à 7T permettant l'imagerie du corps entier, l'un des deux seuls dispositifs de ce type aux Pays-Bas. Cet article résume les progrès en matière d'applications neurologiques effectués au cours de la première année de fonctionnement du scanner 7T à Leiden.

### IRM dynamique totale de la colonne vertébrale chez les contorsionnistes

W.W. Orrison, Jr et T.G. Perkins

Une étude portant sur cinq femmes contorsionnistes d'une école du cirque Mongole a été réalisée pour évaluer les modifications pathologiques pouvant être liées aux torsions importantes du corps dans des positions extrêmes.

Les cinq participantes ont été examinées à l'aide d'un système IRM cylindrique Philips Achieva 3T. En outre, des images dynamiques supplémentaires de la colonne vertébrale de deux participantes ont été acquises à l'aide du système IRM ouvert Philips Panorama HFO 1T afin de définir la plage de mouvement atteinte lors de contorsions extrêmes.

Les modifications pathologiques observées comprennent une saillie des disques intervertébraux, la formation d'ostéophyte et un total de quatre fractures des vertèbres lombaires antéro-supérieures chez trois des cinq participantes.

### Imagerie moléculaire chez les patients atteints de démence: voyage au bout de la nuit

V.L. Villemagne et G.J. O'Keefe

Avec l'apparition de nouvelles stratégies thérapeutiques visant à prévenir ou à retarder les pertes fonctionnelles et cognitives irréversibles chez les patients atteints de démence, de nombreux scientifiques s'intéressent au développement d'agents permettant l'évaluation *in vivo* des mécanismes pathophysiologiques intervenant chez ces patients. L'imagerie moléculaire de certains ligands permet d'effectuer un diagnostic précoce en cas de démence et d'évaluer un traitement anti-démence via l'examen du métabolisme cérébral, des systèmes de neurotransmetteurs, ainsi que des caractéristiques spécifiques de la maladie, telles que la présence de  $\beta$  amyloïde dans le cas de la maladie d'Alzheimer. L'article présente les développements récents dans ce domaine et illustre l'utilité de l'imagerie moléculaire pour la prise en charge clinique des patients atteints de démence.

### Imagerie de particule magnétique tridimensionnelle *in vivo* en temps réel

J. Borgert, B. Gleich, J. Rahmer, H. Dahnke et J. Weizenecker

L'imagerie de particule magnétique est une nouvelle méthode d'imagerie tomographique permettant d'acquérir, avec une résolution spatiale et temporelle de très grande qualité, des images de la concentration locale des traceurs magnétiques. Jusqu'à présent, seuls des essais fantômes en 2D statiques et dynamiques avec une concentration élevée de traceurs avaient été réalisés. Cet article présente les premières acquisitions par imagerie de particule magnétique 3D *in vivo* en temps réel, révélant tous les détails des battements du cœur d'une souris à l'aide de concentrations cliniquement approuvées d'un agent de contraste IRM disponible dans le commerce. Avec ces capacités, l'efficacité de l'imagerie à particule magnétique pour les applications médicales ne tardera pas à être démontrée.

### Cartographie 3D multimodalité en neuroradiologie interventionnelle

T. Andersson, M. Söderman, D. Ruijters, D. Babic, R. Homan et P. Mielekamp

Lors d'un traitement neurovasculaire à invasion minimale, les informations obtenues en temps réel concernant les appareils endovasculaires interventionnels et contenues dans les acquisitions bidimensionnelles (2D) fluoroscopiques et tridimensionnelles provenant de sources telles que l'IRM et la TDM, sont visualisées sur deux écrans distincts. Le médecin doit projeter mentalement l'emplacement de l'appareil endovasculaire sur les données de tissus mous. Cet article décrit une méthode de fusion des informations en une seule image combinée, permettant une réduction de la charge de travail du médecin et une meilleure compréhension anatomique avec une navigation plus précise. Pour bénéficier de performances optimales, la fusion des images doit être réalisée en temps réel avec une latence réduite au minimum et une cadence d'images suffisante.

### **Permeabilität der Blut-Hirn-Schranke: Quantifizierung über Computer-Tomographie und Anwendung bei akuten ischämischen Schlaganfällen**

*M. Wintermark, J. Hom, J. W. Dankbaar, J. Bredno und M. E. Olszewski*

Aufgrund der hohen – menschlichen und finanziellen – Kosten, die durch Schlaganfälle und ihre Folgen verursacht werden, sind Verbesserungen bei der Schlaganfalltherapie von größter Bedeutung. Der Recombinant Tissue Plasminogen Activator (rt-TPA) hat sich bei der Behandlung akuter ischämischer Schlaganfälle als effektiv erwiesen, ist jedoch bislang nur zur Anwendung innerhalb eines festen Zeitfensters zugelassen und wird mit einem nicht zu vernachlässigenden Risiko hämorrhagischer Transformation in Zusammenhang gebracht. In diesem Artikel wird die quantitative CT-Bildgebung der Permeabilität der Blut-Hirn-Schranke erläutert, die möglicherweise eine breitere Anwendung von rt-TPA bei akuten Schlaganfällen ermöglicht: Behandlungsentscheidungen unterliegen dann weniger dem Faktor Zeit, sondern können individuell unter Abwägung der Risiken und unter Berücksichtigung der Physiologie des Patienten getroffen werden.

### **Klinische MR-Traktografie: Vergangenheit, Gegenwart und Zukunft**

*K. Yamada, K. Akazawa, S. Yuen und T. Nishimura*

Die auf der Diffusions-Tensor-Bildgebung (DTI) basierende Traktografie wurde in der Medizin vor etwa einem Jahrzehnt eingeführt. Seitdem wird diese Technik bei zahlreichen klinischen Routinebehandlungen in diversen Bereichen eingesetzt, unter anderem zur präoperativen Planung bei Hirntumoren und Gefäßmissbildungen. Diese Technik macht den Verlauf der eloquenten Faserbündel deutlich, wie beispielsweise der Pyramidenbahn, des visuellen Pfads und des Fasciculus arcuatus. Diese Technik wurde zunächst gemeinsam mit der deterministischen Stromlinien-Methode eingesetzt und anschließend weiterentwickelt, um ausgefeiltere probabilistische Ansätze verwenden zu können. Bei den neuesten Techniken sind die Bildgebungs- und Nachverarbeitungszeiten meistens länger. In diesem kurzen Überblick werden Vergangenheit, Gegenwart und Zukunft der klinischen Traktografie beleuchtet.

### **Klinische Anwendung von Diffusions-Tensor-Bildgebung bei Kindern**

*N.K. Rollins und J.M. Chia*

Die Diffusions-Tensor-Bildgebung (DTI), eine relativ junge Erweiterung der Magnetresonanztomographie, erforscht die bevorzugte Bewegung von Wasserprotonen im Hirn entlang der Axonenachse. Dank der Empfindlichkeit gegenüber der anisotropen Bewegung von Protonen wird durch DTI eine klare Visualisierung der weißen Gehirnsstofffasern als deutliche anatomische Strukturen erreicht. Mit den Informationen aus den Diffusions-Tensor-Daten werden dann mathematische 3D-Renderings der weißen Gehirnsstoffsubstanz erstellt. DTI stellt Informationen zur Mikroarchitektur der weißen Gehirnsstoffsubstanz in Form von Metriken zur Verfügung, aus denen sich Daten zur axonalen Integrität und Myelinisierung ablesen lassen. Es gibt eine Vielzahl von Anwendungsmöglichkeiten für DTI am Gehirn von Kindern im gesunden und erkrankten Zustand ab der Geburt.

### **Funktionales MRT des sensomotorischen Systems bei Neugeborenen**

*H. Boecker, L. Scheef und A. Heep*

Ein neonatales funktionales MRT (fMRT) ermöglicht eine nicht invasive *in-vivo*-Zuordnung dedizierter Schaltkreise im Gehirn in frühen Entwicklungsphasen. In diesem Artikel werden die aktuellen Fortschritte am Universitätskrankenhaus Bonn bei der Gestaltung und Optimierung von fMRT-Studien zusammengefasst, während derer standardisierte passive sensomotorische Stimulationen an Säuglingen getestet werden, die aufgrund einer Frühgeburt Gefahr laufen, motorische Spätfolgen zu entwickeln.

### **7-T-MRT in der Neurologie: Erste Ergebnisse und zukünftige Anwendungen**

*A.G. Webb, M.J. Versluis, M.A. van Buchem, H.E. Kan, W.M. Teeuwisse, und M.J.P. van Osch*

Das medizinische Zentrum der Universität von Leiden (Leids Universitair Medisch Centrum) gründete Ende 2007 innerhalb seiner Radiologieabteilung das C.J. Gortercentrum für Hochfeld-Magnetresonanztomographie (MRT). Das Ziel dieses Zentrums ist die Entwicklung neuer Methoden und Protokolle für klinische Hochfeld-MRTs für unterschiedliche Patientengruppen. Diese Entwicklung läuft parallel zur Durchführung von Studien korrelativer Krankheitsmodelle bei Tieren. Das Zentrum hat kürzlich ein Philips Achieva 7-T-Ganzkörper-MRT-System installiert, eines von insgesamt zweien in den Niederlanden. In diesem Artikel wird der Fortschritt im ersten Betriebsjahr des 7-T-Scanners in Leiden im Rahmen neurologischer Anwendungen untersucht.

### Dynamisches Wirbelsäulen-MRT von Kontorsionisten

W.W. Orrison, Jr und T.G. Perkins

In einer Studie an fünf Kontorsionistinnen („Schlangenfrauen“) aus einer mongolischen Zirkusschule wurden pathologische Änderungen untersucht, die durch die übermäßige Verdrehung des Körpers in extreme Positionen verursacht werden.

Alle fünf Teilnehmerinnen wurden mit einem zylindrischen Philips Achieva 3T-MRT-System untersucht, und zusätzlich wurden von zwei Teilnehmerinnen mit Hilfe des offenen Philips Panorama HFO 1T-MRT-Systems dynamische Bilder der gesamten Wirbelsäule aufgezeichnet, um den Bewegungsbereich zu definieren, der während extremer Verdrehungen erreicht wird.

Entdeckt wurden Bandscheibenschwellungen, Osteophytenformationen und bei drei von fünf Teilnehmerinnen insgesamt vier Frakturen im anterosuperioren Limbus.

### Molekulare Bildgebung bei Demenz: „Voyage au bout de la nuit“

V.L. Villemagne und G.J. O'Keefe

Seit der Einführung neuer therapeutischer Strategien zur Vermeidung oder Verzögerung eines irreversiblen Gedächtnisverlustes bei Demenz besteht zunehmend Interesse an der Entwicklung von Agenzien, die eine *in-vivo*-Analyse der beteiligten pathophysiologischen Mechanismen ermöglichen. Die molekulare Bildgebung mit zielspezifischen Liganden kann die frühe Diagnose einer Demenz und die Evaluierung einer entsprechenden Therapie unterstützen, indem der Energiestoffwechsel im Gehirn, die Neurotransmittersysteme und krankheitsspezifische Eigenschaften wie das  $\beta$ -Amyloid bei Alzheimer untersucht werden. In diesem Artikel werden die aktuellen Entwicklungen in diesem Bereich erläutert und der Nutzen der molekularen Bildgebung bei der klinischen Behandlung von Demenz aufgezeigt.

### Dreidimensionales *in-vivo*-MPI in Echtzeit

J. Borgert, B. Gleich, J. Rahmer, H. Dahnke und J. Weizenecker

Magnetic Particle Imaging (MPI) ist eine neue Methode zur tomografischen Bildgebung, bei der eine lokale Konzentration magnetischen Tracer-Materials mit hoher räumlicher und zeitlicher Auflösung dargestellt wird. Bislang wurden lediglich statische und dynamische 2D-Phantomuntersuchungen mit hohen Tracer-Konzentrationen durchgeführt. In diesem Artikel werden die ersten 3D-*in-vivo*-Echtzeit-MPI-Scans vorgestellt, die Details eines schlagenden Mauserzens enthüllen, die durch klinisch genehmigte Konzentrationen eines kommerziell erhältlichen MRT-Kontrastmittels erreicht wurden. Dieses Ergebnis zeigt deutlich, dass MPI für medizinische Anwendungen durchaus geeignet ist.

### Modalitätsübergreifendes 3D-Roadmapping in der interventionellen Neuroradiologie

T. Andersson, M. Söderman, D. Ruijters, D. Babic, R. Homan und P. Mielekamp

Im Rahmen minimalinvasiver neurovaskulärer Behandlungen werden Live-Informationen von interventionellen endovaskulären Geräten in der 2D-Fluoroskopie und 3D-Bilder aus MRT- und CT-Systemen auf separaten Bildschirmen angezeigt. Der Untersuchende muss hierbei im Kopf die Position des endovaskulären Geräts auf die Weichteildaten projizieren. In diesem Artikel wird eine Methode zur Zusammenführung der Informationen in einem kombinierten Bild erläutert. Auf diese Weise sollen die Belastung des Untersuchenden verringert und ein besseres Verständnis der Anatomie sowie eine präzisere Navigation erreicht werden. Um die Vorteile der Bildzusammenführung vollständig nutzen zu können, muss diese in Echtzeit mit minimaler Latenz und einer ausreichenden Bildfrequenz geschehen.

### **Permeabilidad de la barrera hematoencefálica: cuantificación mediante tomografía computerizada y aplicación en ictus isquémico agudo**

*M. Wintermark, J. Hom, J. W. Dankbaar, J. Bredno y M. E. Olszewski*

Dados los elevados costes, tanto humanos como económicos, asociados al ictus y sus secuelas, las mejoras en su tratamiento adquieren una importancia crucial. Se ha demostrado que el activador del plasminógeno tisular recombinante (rt-PA) resulta eficaz en el tratamiento del ictus isquémico agudo. No obstante, en la actualidad el uso del rt-PA se ha aprobado únicamente para un período de tiempo limitado y se asocia a un riesgo significativo de transformación hemorrágica. En este artículo se describe cómo la adquisición cuantitativa de imágenes tomográficas de la permeabilidad de la barrera hematoencefálica puede permitir una extensión de la administración del rt-PA en casos de ictus agudo, facilitando así la toma de decisiones individualizadas y con riesgos sopesados para el tratamiento, basadas en aspectos fisiológicos en lugar de aspectos temporales.

### **Tractografía clínica por RM: pasado, presente y futuro**

*K. Yamada, K. Akazawa, S. Yuen y T. Nishimura*

Hace ya una década, la tractografía por imágenes con tensor de difusión (DTI) se presentaba por primera vez en la comunidad médica. Desde entonces, esta técnica se ha utilizado ampliamente en diversos campos de la práctica clínica rutinaria, incluida la planificación preoperatoria en casos de tumores cerebrales y anomalías vasculares. Esta técnica muestra con claridad los recorridos de tractos de fibras significativos, tales como el tracto piramidal, el tracto óptico y el fascículo arqueado. En un primer momento, esta técnica se introdujo con un enfoque más de determinación pero ha evolucionado hacia una perspectiva de probabilidad más sofisticada. Por lo general, el tiempo requerido por las técnicas más recientes para la adquisición de imágenes y el posprocesamiento es mayor. En esta breve reseña se describe la situación pasada, presente y futura de la tractografía clínica.

### **Aplicaciones clínicas para imagen con tensor de difusión en pacientes pediátricos**

*N.K. Rollins y J.M. Chia*

La imagen con tensor de difusión (DTI), una incorporación relativamente nueva a la adquisición de imágenes por RM, aprovecha el movimiento aleatorio de los protones de agua en el cerebro a lo largo del eje de los axones. A consecuencia de la sensibilidad al movimiento anisotrópico de los protones, la DTI permite la visualización individual de tractos de sustancia blanca como estructuras anatómicas diferenciadas. La información contenida en los datos del tensor de difusión puede generar representaciones matemáticas tridimensionales de la sustancia blanca. La DTI puede proporcionar información acerca de la microarquitectura de la sustancia blanca en forma de valores métricos que ofrecen datos sobre mielinización e integridad axonal. La DTI tiene diversas aplicaciones cerebrales en pacientes pediátricos, del nacimiento en adelante, en estados de salud normales y de enfermedad.

### **RM funcional del sistema sensitivomotor en recién nacidos**

*H. Boecker, L. Scheef y A. Heep*

La RM funcional (RMf) en neonatos permite la representación *in vivo* no invasiva de circuitos cerebrales específicos en las etapas iniciales de desarrollo. En este artículo se resume la experiencia actual del Hospital Universitario de Bonn en la realización y optimización de estudios de RMf que utilizan métodos de estimulación sensitivomotora pasiva estandarizada en lactantes con alto riesgo de presentar secuelas en el sistema motor tras un parto prematuro.

### **Imagen neurológica por RM de 7T: resultados iniciales y aplicaciones futuras**

*A. G. Webb, M. J. Versluis, M.A. van Buchem, H. E. Kan, W.M. Teeuwisse y M. J. P. van Osch*

El Centro Médico de la Universidad de Leiden estableció el Centro C.J. Gorter para la adquisición de imágenes mediante resonancia magnética (RM) de alto campo en el Departamento de Radiología a finales de 2007. El objetivo del Centro es desarrollar métodos y protocolos nuevos para la RM clínica de alto campo en diversas poblaciones de pacientes. Esta labor se efectúa en paralelo con la realización de estudios sobre tipos de enfermedad correlativos en animales. Recientemente, el Centro instaló un sistema de RM Philips Achieva para cuerpo entero de 7T, uno de los dos que existen en los Países Bajos. Este artículo resume los avances en las aplicaciones neurológicas durante el primer año de uso del escáner de 7T en Leiden.

### RM dinámica de columna vertebral completa de contorsionistas

W. W. Orrison, Jr y T. G. Perkins

Se ha realizado un estudio con cinco mujeres contorsionistas de una escuela circense de Mongolia para evaluar los cambios patológicos que se pueden asociar a torsiones extremas del cuerpo en posiciones límite.

Las cinco participantes se examinaron con un equipo de resonancia magnética cilíndrico Philips Achieva 3T y se obtuvieron imágenes dinámicas adicionales de la columna vertebral completa de dos participantes con un equipo de resonancia magnética abierto Philips Panorama HFO 1T para determinar el rango de movimiento alcanzado durante la contorsión extrema.

Entre los cambios patológicos detectados se incluyen hernias de disco intervertebral, formación de osteofitos y un total de cuatro fracturas de miembros anterosuperiores en tres de las cinco participantes.

### Adquisición de imágenes moleculares en casos de demencia: viaje al fin de la noche

V.L.Villemagne y G.J. O'Keefe

Con la aparición de nuevas estrategias terapéuticas destinadas a la prevención o al retraso de las pérdidas cognitivas funcionales e irreversibles propias de la demencia, ha aumentado el interés por el desarrollo de agentes que permitan la evaluación *in vivo* de los mecanismos fisiopatológicos que intervienen.

La adquisición de imágenes moleculares con ligandos específicos del objetivo permite diagnosticar la demencia de forma temprana y valorar el tratamiento de la demencia mediante un examen del metabolismo cerebral, los sistemas de neurotransmisores, así como los rasgos específicos de la enfermedad, tales como el  $\beta$ -amiloides propio de la enfermedad de Alzheimer. Se están analizando los desarrollos recientes en este campo para demostrar la utilidad de la adquisición de imágenes moleculares en el control clínico de la demencia.

### Adquisición de imágenes de partículas magnéticas *in vivo* tridimensionales en tiempo real

J. Borgert, B. Gleich, J. Rahmer, H. Dahnke y J. Weizenecker

La adquisición de imágenes de partículas magnéticas es un nuevo método tomográfico que permite obtener imágenes de la concentración local de los materiales empleados como marcadores magnéticos con una gran resolución espacial y temporal. Hasta el momento, sólo se habían realizado experimentos con maniqués estáticos y dinámicos en 2D con altas concentraciones de marcadores magnéticos. En este artículo, se presentan las primeras exploraciones 3D *in vivo* de partículas magnéticas en tiempo real que revelan los detalles del latido del corazón de un ratón mediante concentraciones clínicamente aprobadas de un medio de contraste de RM disponible en el mercado. Con todas estas funciones, se ha logrado un gran avance en lo que respecta a resonancia de partículas magnéticas, demostrando su idoneidad para aplicaciones médicas.

### Cartografía 3D multimodalidad en neurorradiología intervencionista

T. Andersson, M. Söderman, D. Ruijters, D. Babic, R. Homan y P. Mielekamp

Durante un tratamiento neurovascular mínimamente invasivo, la información en tiempo real relacionada con los dispositivos endovasculares intervencionistas de la fluoroscopia bidimensional (2D) y las imágenes en tres dimensiones de fuentes como imágenes de resonancia magnética y de tomografía computerizada se visualizan en pantallas diferentes. El radiólogo debe proyectar mentalmente la posición del dispositivo endovascular en los datos del tejido blando. Este artículo describe un método de fusión de la información en una imagen combinada. De esta forma, se reducirá la carga de trabajo del radiólogo y se mejorará el conocimiento anatómico con una navegación más precisa. Para conseguir el máximo provecho, la fusión de imágenes debe producirse en tiempo real con una latencia mínima y una velocidad suficiente de imágenes.

## New products

### Innovative neuroradiology interpretation made possible by Advanced Vessel Analysis on the Brilliance Workspace

Philips has developed the Brilliance Everywhere solution to help CT clinical experts pioneer breakthrough imaging techniques. Philips' Advanced Vessel Analysis (AVA) is one of the ways they achieve this. This application features neuro bone removal. When performing neuro CT angiography studies, bone removal becomes a challenge due to the proximity of the bones and vessels in the carotid siphon region. The Philips AVA package automatically removes bones to provide clear visualization of the vessels and enables automatic extraction of centerlines and contours for vessel analysis. A recent study compared the effectiveness of conventional tools with that of bone removal in the interpretation and detection of cerebral aneurysms. The study showed that the AVA method offered significant workflow improvements in post-processing time and increased aneurysm detection sensitivity.



▲ CT and geographic image using automatic bone removal method

The Brilliance Workspace is ranked #1 in Advanced Visualization by KLAS as reported in its 2008 Top 20 Best in KLAS Awards ■

### The Wireless Portable Detector for DigitalDiagnost

The innovative wireless portable detector with its array of well thought-out accessories maximizes flexibility and efficiency in the DR room. In combination with a digital bucky system, such as the Philips DigitalDiagnost with moveable multi-purpose detector (Figure 1), it offers a versatile and cost-efficient solution meeting a range of imaging requirements. Horizontal, vertical and lateral exams can be performed with just one fixed detector (Figure 2), while the wireless portable detector can be used for more complex projections and free exposures.

The wireless portable detector's cable-free design helps healthcare providers meet high standards of hygiene, and allows for convenient handling.

As part of Philips' Eleva concept, the wireless portable detector benefits from exceptional UNIQUE image quality and provides DR images instantly. The wireless portable detector can be alternated with CR cassettes ■



▲ Figure 1. The wireless portable detector allows even the most difficult projections at table, patient bed, wheelchair or trolley.



▲ Figure 2. With the moveable multi-purpose stand, all horizontal, vertical and lateral examinations are fast and convenient.

## New FlexVision XL display helps clinicians to perform complex interventional procedures



FlexVision XL is a new viewing concept giving clinicians full control over their viewing environment from the tableside. This allows clinicians to display multiple images simultaneously in their own preferred size and layout. The 56-inch (125 cm) screen, covering an area greater than the equivalent screen area of six standard monitors, offers a resolution of 8 million pixels. FlexVision XL is now available commercially.

In today's interventional setting, clinicians must perform procedures that are ever more complex, with smaller devices, on complex anatomies – a difficult combination. They often have to sort through diagnostic information from multiple sources to help guide their intervention.

Philips has introduced FlexVision XL to help them meet these challenges. FlexVision XL provides outstanding viewing flexibility from the tableside and supports clinicians in carrying out complex interventional procedures.

A SuperZoom function with advanced image-sharpening algorithms lets clinicians magnify images and make out fine details without having to move closer to the display. They can also select an on-screen layout of images that suits the way they work, change it at any time during the procedure, and customize the layouts by switching sources. In addition, they are able to manage multiple video sources on one screen from the tableside ■

## Instructions to authors

Medicamundi is a journal for medical professionals, published by Philips Healthcare. It provides information on the medical applications of Philips Healthcare products, and the results obtained. Articles on related topics, such as economic and technical aspects, will also be considered for publication.

The Editor-in-Chief reserves the right to require the revision of a manuscript as a condition of its acceptance and to make any changes required to make the article conform to the editorial standards of Medicamundi and/or regulatory requirements (this could result in publication only in the international edition, which is distributed outside the USA).

The Editor-in-Chief and the editorial staff accept no responsibility for opinions expressed by the contributors, and the description of a particular medical procedure does not imply approval of the procedure in all countries. Examples of earlier issues of Medicamundi can be found on the Philips website: [www.philips.com/medicamundi](http://www.philips.com/medicamundi)

### ► Permission to publish

Submission of an article implies transfer of copyright (in the case of government employees to the extent transferable) to the Editor-in-Chief of Medicamundi.

### ► Title page

The title page should carry the title (underlined), the authors' names and the name(s) of the department(s) and institution(s) to which the work should be attributed. The title should be brief (max. 140 characters including spaces).

The principal author's name should be given first, followed by the names of the other authors in alphabetical order. For reasons of space and ease of cross-referencing, it is preferred to have no more than six authors.

The exact postal address (complete with post code) and the e-mail address of the principal author should be given on the title page. N.B. This is for internal information and will not be published.

### ► Abstract

Each article must be accompanied by an abstract of not more than 100 words.

### ► References

All claims in the text must be supported by appropriate references. The references should be restricted to publications referred to in the text, and the list should be kept reasonably short. References in the text should be identified only by Arabic numerals [in square brackets], and be numbered consecutively as they appear in the text. References should be presented in accordance with "Citing Medicine" – the National Library of Medicine Style Guide. See [www.nlm.gov/citingmedicine](http://www.nlm.gov/citingmedicine)

### ► Language

Manuscripts may be submitted in English, French, German, Spanish, Japanese, Chinese or Dutch. Accepted articles will be translated where necessary and published in English.

### ► Abbreviations

Except for units of measurement, abbreviations are strongly discouraged. Except for units of measurement, the first time an abbreviation appears, it should be preceded by the words for which it stands.

### ► Informed consent

Articles reporting the results of experimental studies on human subjects must include a statement to the effect that

informed consent was obtained, after the nature of the procedure(s) had been fully explained. Reports of animal studies must be accompanied by a statement that the animals have been maintained in accordance with the appropriate guidelines and regulations.

### ► Rights and permissions

The principal author is responsible for obtaining permission to use any previously published figures or tables. The source of the material should be clearly indicated in the manuscript. The principal author is also responsible for obtaining permission to reproduce any photograph showing recognizable persons.

### ► Electronic submission

Articles can be accepted as e-mail attachments or on CD-rom. Text and illustrations should be submitted as separate files.

#### *Text file*

Texts should be submitted as a single text file, preferably in Word™. Use the default settings, and keep the text free from formatting codes, as these can cause problems when the text is converted for typesetting. Only use the hard return at the end of sections or paragraphs.

### Do not use automated tools for inserting references etc. as this information may be lost.

#### *Image file*

Original clinical images should be provided in PC tif format with an image width of at least 66 mm (2.6 in.) at a resolution of 350 dpi. If the imaging modality does not meet these specifications, provide original clinical images with the highest resolution available.

Please rank the importance of the visuals so that the key ones supporting the article can be made as large as possible. (Ranking: most important = A, less important = B, least important = C)

### • Do not import illustrations and clinical images into the text.

### • Never use desktop systems to interpolate image data: this produces artifacts that cannot be removed.

### • Images must never be superimposed or overlap, and there should be no texts or symbols in the image area.

### • PowerPoint presentations do not meet the requirements for printing and cannot be used.

If there are technical questions regarding images, please contact [wolf.zimmermann@philips.com](mailto:wolf.zimmermann@philips.com)

### ► Proofs

In place of a proof, a pdf of the laid-out article will be provided. Unless otherwise specified, this will be e-mailed to the first named author.

### N.B. Corrections should be restricted to errors, as editorial alterations at this stage can lead to delays in production.

### ► Complimentary copies and honorarium

The principal author of a published Medicamundi article is entitled to 50 complimentary copies. Please provide the address to which these should be sent when submitting the article.

### ► How to submit an article to Medicamundi

Medicamundi welcomes articles on interesting applications of Philips Healthcare products.

Because Medicamundi is a scientific journal, the articles should be written in a neutral, factual style, usually in the third person.

Although not all criteria will be appropriate for every article, the article should cover all or most of the following points:

- the type of healthcare institution
- the clinical problems to be solved
- the type of equipment used
- the examination parameters
- the results obtained, with good-quality illustrations.

### Printed images demand a higher resolution than electronic displays. Please read the adjacent section on Electronic submission.

The article should proceed smoothly from start to conclusion, without digressions. As it is an article, rather than a scientific report, the sections should have titles, but not be numbered.

The article should not exceed 2500 words, and should be accompanied by an abstract of not more than 100 words.

Please note that it is not always possible to include all articles submitted – sometimes a selection has to be made! The decision to publish is the responsibility of the Editorial Board of Medicamundi, who will review all submitted articles.

### ► Submission of articles and images

Articles for publication in Medicamundi should be submitted to:

The Editor-in-Chief  
Medicamundi  
Philips Healthcare  
Building QX-2.135.1  
P.O. Box 10 000  
5680 DA Best, the Netherlands  
E-mail: [healthcare@philips.com](mailto:healthcare@philips.com)

Images should be sent directly and only to our digital publishing specialist:  
[wolf.zimmermann@philips.com](mailto:wolf.zimmermann@philips.com)

## Inside information...

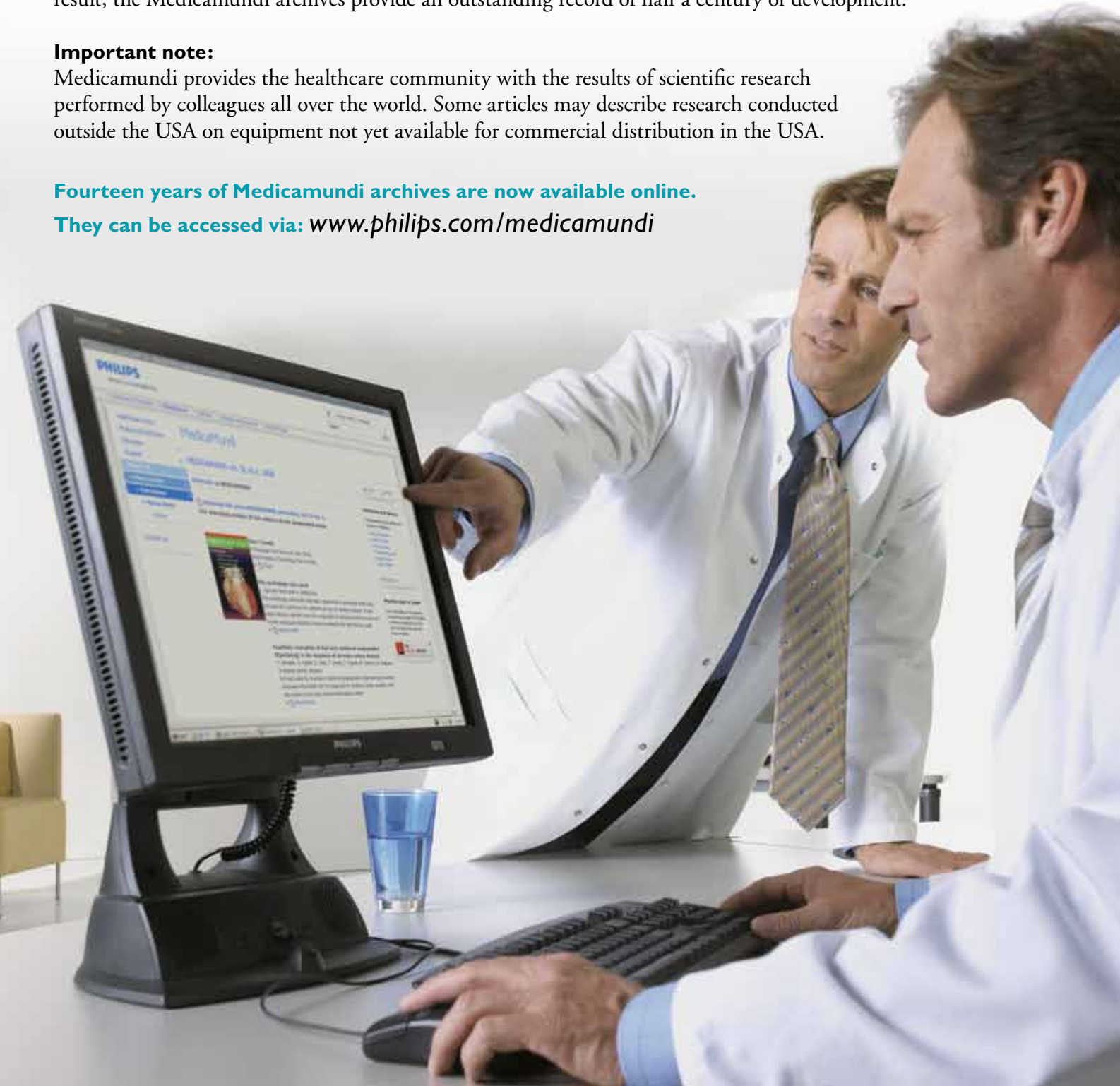
Medicamundi allows healthcare professionals and the industry to share inside information on the latest technological developments and their medical applications. Over the last fifty years, Medicamundi has been among the first to present many of the extraordinary developments in healthcare technology in general, and medical imaging in particular. As a result, the Medicamundi archives provide an outstanding record of half a century of development.

### **Important note:**

Medicamundi provides the healthcare community with the results of scientific research performed by colleagues all over the world. Some articles may describe research conducted outside the USA on equipment not yet available for commercial distribution in the USA.

**Fourteen years of Medicamundi archives are now available online.**

**They can be accessed via: [www.philips.com/medicamundi](http://www.philips.com/medicamundi)**



# PHILIPS